T2R2 東京科学大学 リサーチリポジトリ
Science Tokyo Research Repository

論文 / 著書情報
Article / Book Information

題目(和文)	金及び金合金めっきの機械的強度の強化
Title(English)	Enhancement of Mechanical Strength in Electrodeposited Gold and Gold Alloys
著者(和文)	唐 浩峻
Author(English)	Hao-Chun Tang
出典(和文)	学位:博士(工学), 学位授与機関:東京工業大学, 報告番号:甲第10981号, 授与年月日:2018年9月20日, 学位の種別:課程博士, 審査員:曽根 正人,木村 好里,寺田 芳弘,細田 秀樹,三宮 工
Citation(English)	Degree:Doctor (Engineering), Conferring organization: Tokyo Institute of Technology, Report number:甲第10981号, Conferred date:2018/9/20, Degree Type:Course doctor, Examiner:,,,,
学位種別(和文)	博士論文
Type(English)	Doctoral Thesis

Powered by T2R2 (Science Tokyo Research Repository)

Enhancement of Mechanical Strength in Electrodeposited Gold and Gold Alloys

Doctor of Engineering

Department of Material Science and Engineering

Tokyo Institute of Technology

Hao-Chun Tang

2018

Table of content

CHAPTER 1 1
General Introduction

1.1. Background of the Present Study 1
1.1.1. Application of Au Materials in MEMS Devices 1
1.1.2. Strengthening Mechanisms in Electrodeposits 3
1.1.3. Electrodeposition of Metallic Materials 5
1.1.4. Mechanical Properties of Small-Scale Materials 8
1.2. Objective of the Present Study 9
1.3. Outline of This Study 9
1.4. References 11
1.5. Figures 18

CHAPTER 2 26
Fabrication of Ultrafine-Grained Au by Electrodeposition Techniques

2.1. Introduction 26
2.2. Experimental 28
2.2.1. Electroplating of Au Films 28
2.2.2. Characterization and Micro-Compression Tests 29
2.3. Results and Discussion 30
2.3.1. Crystalline Structure and Composition of Electrodeposited Au Films 30
2.3.2. Deformation Behaviors of Au Micro-Pillars 31
2.3.3. Micro-Mechanical Properties of Au Micro-Pillars 32
2.3.4. Mechanical Properties of the Au Pillars with Different Dimensions 33
2.4. Conclusions 35
2.5. References 36
2.6. Figures 40

CHAPTER 3 48
Galvanic Deposition of Au–Cu Alloys from Non-Cyanide Electrolyte

3.1. Introduction 48

3.2. Experimental 49
3.2.1. Fabrication of Au–Cu Alloys by Galvanostatic Plating 49
3.2.2. Characterization 50
3.2.3. Micro-Compression Tests 50
3.3. Results and Discussion 51
3.3.1. Surface Morphology of Au–Cu Films 51
3.3.2. Crystalline Structure and Composition 51
3.3.3. Deformation Behavior of Au–Cu Micro-Pillars and Micro-Mechanical Properties 52
3.3.4. Strengthening Mechanisms in the Electroplated Au–Cu Alloys 53
3.4. Conclusions 55
3.5 References 56
3.6. Figures 59

CHAPTER 4 .... **65**
Pulse Current Electrodeposition of Ultrahigh Strength Nanocrystalline Au–Cu Alloys

4.1. Introduction 65
4.2. Experimental 67
4.2.1. Fabrication of Au–Cu Alloys by Pulse Electroplating 67
4.2.2. Characterization and Micro-Compression Tests 67
4.3. Results and Discussion 68
4.3.1. Effects of Pulse Current Density 68
4.3.2. Effects of Current Off-Time 69
4.3.3. Morphology of Au–Cu Alloys 72
4.3.4. Micro-Mechanical Properties of Pulse Electroplated Au–Cu Alloys 73
4.4. Conclusions 75
4.5. References 77
4.6. Tables 81
4.7. Figures 83

CHAPTER 5 .... **92**
Microstructure of Electrodeposited Au–Cu Alloys Observed by High-Resolution Transmission Electron Microscopy

5.1. Introduction 92

5.2. Experimental 94
5.3. Results and Discussion 95
5.4. Conclusion 99
5.5. References 101
5.6. Figures 106

CHAPTER 6 .... **111**
Summary and General Conclusions

Acknowledgements 115
Publication Lists 117
Presentation Lists 120

CHAPTER 1

General Introduction

1.1. Background of the Present Study

1.1.1. Application of Au Materials in MEMS Devices

In recent years, microelectromechanical systems (MEMS) capacitive accelerometers have been developed and used in a variety of consumer electronics for the acceleration detection of 1–5 G (1 G = 9.8 m/s^2) [1–3]. Along with the development of MEMS accelerometers, many technologies have been reported to improve the device performance and small-size implementation of multi-axis acceleration sensing. Especially for the application in the medical and health care fields, accurate sensing with sub-1 G detection is necessary for monitoring the human activities [4,5]. To detect such low acceleration in a compact sensor module, various types of MEMS accelerometers based on silicon (Si) bulk micromachining [6,7] have been reported to utilize a large proof mass to suppress the thermal-mechanical noise (i.e., Brownian noise (B_N) [8]). For further miniaturization and high functionality of MEMS accelerometers, complementary metal-oxide semiconductor (CMOS)–MEMS technology has also been applied to accelerometer developments by taking advantage of the foundry services for mass production, smaller chip size, high functionalities with CMOS circuitry, and minimal parasitic capacitances [9–11]. While, limited choices of materials and thickness for CMOS-MEMS accelerometer have been the major issue to reduce B_N, which would become critical for

low-acceleration sensing with high precision when the parasitic capacitance is minimized.

Thermal-mechanical noise of the proof mass in an accelerometer can be gauged by B_N that arises from the random thermal motion of molecules in the surrounding gas, as described in the following equation [8]:

$$B_{\mathrm{N}} = \frac{\sqrt{4k_{\mathrm{B}}Tb}}{m} \quad (1\text{-}1)$$

where k_B is the Boltzmann constant, T is the absolute temperature, b is the viscous damping coefficient, and m is the mass of the movable parts of an accelerometer. Equation (1.1) indicates that the B_N can be subjected largely to the size and density of proof mass. The analytical modeling of B_N on the proof masses made of different materials is shown in Fig. 1.1(c). The results show that using a high density material (i.e., Au = 19.3 g/cm^3) can effectively reduce the B_N when the size of proof mass decreases. Yamane et al. [12–14] proposed a miniaturized MEMS accelerometer (Fig. 1.1(a,b)) by using a post-CMOS process with electrodeposited Au micro-components, which enabled further size reduction of the proof mass and the device footprint without compromising the sensitivity. With the application of electrodeposited Au in the MEMS accelerometers [12–14], a wide range of acceleration from 1 mG to 20 G can be achieved and are expected to be used for monitoring the human-activities with required high sensitivity.

However, the mechanical strength of Au is much lower than the conventional Si used in MEMS accelerometers. The yield strength of Au is 50–200 MPa in it bulk state [15]. The fracture strength of Si is 1–3 GPa [16], which is one order larger than Au. The lower mechanical strength of Au would cause the structural stability when employed as the micro-movable components. The long-term vibration tests using the electrodeposited Au cantilevers show that the height of cantilever-tip slightly changed after the vibration cycle exceed over ~10^7 [17]. Therefore, strengthening is necessary for ensuring the long-

term stability of Au-based MEMS accelerometers.

1.1.2. Strengthening Mechanisms in Electrodeposits

Typically, there are four strengthening mechanisms in the metallic materials, including work (strain) hardening, grain boundary strengthening, precipitation strengthening, and solid solution strengthening. Expect for the work hardening, the other strengthening methods are achievable in electrodeposits by adjusting the electrodeposition conditions. For example, Rashidi et al. [18,19] reported that a fine-grained structure can be obtained in the electrodeposited Ni by controlling the electroplating parameters such as current density, bath temperature, and additive amount in aqueous electrolyte. Classically, one would expect an increase in yield strength or hardness for smaller grain sizes according to the Hall–Petch equation [20] given by:

$$\sigma = \sigma_0 + k \cdot d_g^{-0.5} \quad (1\text{-}2)$$

where σ_0 is the friction stress in the absence of grain boundaries, k is a constant and d_g is the grain size. In other words, the yield strength increases with decreasing grain size because pile-ups in fine-grained materials contain fewer dislocations, the stress at the tip of the pile-up decreases and, thus, a larger applied stress is required to generate dislocations in the adjacent grain. In very small grains, this mechanism will break down because grains are unable to support dislocation pile-ups. Typically, this is expected to occur at grain sizes below 10 nm for most metals. The relationship between yield strength and grain size is illustration in Fig. 1.2.

Alloying is also one of commonly using method for increasing the mechanical strength in electrodeposits. Solid solution strengthening results from an interaction between dislocation and solute atoms, as shown in Fig. 1.3(a). The solution atoms

influence the elastic energy of a dislocation due to both local size and modulus changes and act as obstacles to dislocation motion. The alloys could be electrodeposited from a mixed electrolyte containing different metal salts. Schuh et al. [21] reported that the hardness of Ni increased from 1 GPa to 8 GPa by forming the Ni–W alloys. Similar strengthening was also reported in the Ni–Co [22,23], Ni–P [24], and Ni–Mn [25]. In addition, alloying with the elements having large difference of atomic masses would exhibit pronounced strengthening as demonstrated in Cu-based alloys (Fig. 1.3(b)) [26].

On the other hand, nanotwinned structure can also increase the mechanical strength [27]. Lu et al. [27] reported that ultrafine epitaxial-rained Cu with high density nano-scale twins synthesized by pulse electrodeposition exhibits similar dependence like Hall–Petch relationship which the tensile yield strength increases with reducing the twin thickness [28]. It indicates that nanoscale twin boundaries, by blocking dislocation motion, provide as much strengthening as conventional high-angle grain boundaries (Fig. 1.4). Besides, the elecrodeposited alloys such as Ni–Mn [25] and Ni–Co [29] often exhibit the twinned structure in randomly oriented crystalline grains due to the reduction of stacking fault energy, promoting the formation of growth twins in as-deposited electrodeposits.

The deposited Au are widely used as interconnection in electronic devices because of its outstanding properties of high chemical stability, corrosion resistance, and electrical conductivity. However, the mechanical properties were seldom discussed. With the application of micro-components in the MEMS devices, strengthening in the Au materials has become an urgent issue for maintaining the structural stability of the MEMS devices. It is expected that the strengthening mechanisms used for metals can be adopted in the electrodeposited Au materials.

1.1.3. Electrodeposition of Metallic Materials

Electrodeposition is one of the film growth processes for the formation of metallic coating onto a base materials occurring through the electrochemical reaction of metal ions from an electrolyte. The electroplating process consists essentially in the immersion of the object (cathode) to be coated in a vessel containing the electrolyte and a counter electrode (anode), followed by the connection of the two electrodes to an external power supply to make current flow possible. The object to be coated is connected to the negative terminal of the power supply, in such a way that the metal ions are reduced to metal atoms, which eventually form the deposit on the surface. Several electroplating parameters (i.e., composition of electrolyte, current density, bath temperature, pH value, etc.) can be controlled to obtain the desired properties of the electrodeposits. To date, electrodeposition has been frequently utilized for practical purposes in a wide variety of technical fields ranging from metallurgy and heavy engineering industries to microelectronics and nanotechnology.

Electrodeposition is usually carried in two controlling modes: potentiostatic method and galvanostatic method (Fig. 1.5(a,b)). For potentiostatic method, in addition to anode (working electrode) and cathode (counter electrode), reference electrode is necessary for controlling the reduction potential of metal ions. Using this method can precisely control the potential difference between cathode and reference electrode; while, the current density may vary in the electroplating process due to the morphology change or composition change in electrolyte, leading to the difficulty on the estimation of electrodeposit thickness and current density efficiency. For galvanostatic method, the fixed current density is used in the electroplating process and could be generated by a simple power supply. This method only requires anode and cathode; therefore, it widely

used in the industry especially for electroplating with large objects.

In metal electrodeposition, current density is often used to control the characteristics in electrodeposits, in particular, the grain size. The theory of metal deposition is based generally on the Butler–Volmer (BV) equation [30] giving the current density on a meal substrate as a function of overpotential η:

$$j = j_0 \left\{ \exp\left(\frac{\alpha_a zF}{RT}\eta\right) - \exp\left(\frac{\alpha_c zF}{RT}\eta\right) \right\} \quad (1\text{-}3)$$

$$\eta = E - E_{\text{eq}} \quad (1\text{-}4)$$

where j is the electrode current density, j_0 is the exchange current density, z is the number of electrons involved in the electrode reaction, F is the Faraday constant, R is the universal gas constant, T is the absolute temperature, α_a and α_a are the anodic and cathodic transfer coefficient, η is the overpotential, E is the electrode potential, E_{eq} is the equilibrium potential. The first and second terms in right side of the equation (1-3) are associated with the reactions occurred at anode surface and cathode surface, respectively. Because the electrochemical reduction of metal ions is occurred at cathode, the BV equation could be simplified and considered to be half-cell reaction with cathodic term. On the other hand, the nucleation rate (υ) during the electrodeposition could be expressed by the following equation [31]:

$$\upsilon = a \cdot \exp\left(-\frac{b\varepsilon^2}{qk_{\text{B}}T|\eta|}\right) \quad (1\text{-}5)$$

where a is a proportionality constant, b is the geometrical factor, ε is the surface energy, q is the required charges for formation of a monolayer. Combining the equations of (1-3) and (1-5), the nucleation rate can be promoted by an increase of current density, leading to a finer-grained structure in electrodeposits.

Pulse electroplating is a versatile method that was proven to produce

nanocrystalline materials [32,33]. Pulse plating parameters (current on-time, current off-time, and pulse current density) play a major role on controlling the electrocrystallization process, and hence the microstructure and properties of the electrodeposits. Because of the higher instantaneous current density in comparison to direct current plating, pulse electrodeposition has been found to be an effective means of perturbing the adsorption–desorption processes occurring at the electrodeposit/electrolyte interface and hence offers an opportunity to control the microstructure of the electrodeposits [34,35]. The difference between constant current electroplating and pulse electroplating on the current waveform is shown in Fig. 1.5(c,d).

On the other hand, application of supercritical carbon dioxide ($scCO_2$) in the electroplating process has been developed to solve the problems encountered in miniaturization of the devices [36], such as reducing usage of organic solvents in the cleaning process, drying of the nano-structures after the electroplating process, and minimize problems caused by evolution of H_2. In particular, H_2 gas bubbles adsorbed on the surface of cathode is one of the major causes for defects found in the electrodeposits reduced from the acid electrolyte (Fig. 1.6(a)) [37]. Previous studies showed that electroplating with the $scCO_2$-contained electrolyte (EP-SCE) has the effects on the grain refinement due to the periodic-plating-characteristic mechanism [38,39] which is similar to the pulse electroplating, shown in Fig. 1.7. In addition, Chung and Tsai [39] proposed the grain refinement and enhancement of mechanical strength in the electrodeposited Ni using the EP-SCE method. The higher impurity C content in Ni electrodeposits suggest that the impurity C decomposed from the CO_2 in the electrolyte would precipitate in the grain boundary, causing the precipitation strengthening. Another advantage of using EP-SCE is surface smoothening. The solubility of H_2 is high in CO_2 because of the non-polar

property [40]; therefore, desorption of H_2 gas bubbles from the surface of cathode could significantly enhanced in sc-CO_2 (Fig. 1.6(b)). To date, the EP-SCE has been employed on the fabrication of several metal films including Ni [38,39], Cu [41], Sn [42], and Co [43]. However, Au have not been reported yet. It is expected that EP-SCE can be employed in the fabrication of Au as well as other materials.

1.1.4. Mechanical Properties of Small-Scale Materials

Micro-components used in MEMS such as micro-spring, bending beams, and structural support of MEMS suffer from mechanical straining and need suitable mechanical properties. For mechanical evaluation on such materials, conventional indentation or wear test is insufficient for obtaining real information on the micro-components. Moreover, when the sample size comes to micro-scales, the classical physics are not always useful because of size effect. In the past decade, micro-mechanical tests have been developed to investigate the mechanical properties of specimens in the micron- or nano-scale [44–51]. Since Uchic et al. [44] first introduced the uniaxial compression testing of micro-pillars, a new wave of studies of small-scale plasticity has been explored in numerous materials. The majority of research investigating the size effect of metals by means of the micro-testing technique has focused on single crystalline metals [44–46] and metallic grasses [52,53]. It was observed that the yield strength scales inversely with some power to the pillar diameter. Many subsequent investigations followed on single crystall face-centred-cubic (fcc) and body-centred-cubic (bcc) metals, with power law scaling exponents being agreed to be 0.6 for fcc [45,46], and 0.2–0.6 for bcc metals [48], respectively. For the poly- or nanocrysalline materials, both the phenomena of "Smaller is stronger" [54,55] and "Smaller is weaker" [56,57] were observed; while, those

experimental findings for sample size effect are still inconclusive.

Components used in MEMS devices are usually in micron- or nano-scale, and mechanical properties of materials in micro-scale are often different from those of the bulk materials. Therefore, the mechanical properties of the electroplated micro-components have great interests in industries owing to miniaturization of MEMS devices reaching to its component scales at sub-micron or nano regime. In previous studies, our group has reported several methods to evaluate the micro-mechanical properties of electrodeposited materials, such as micro-compression [50,58], micro-tensile [59], and micro-bending [60]. Those micro-specimens are made by focus ion beam (FIB), as shown in Fig. 1.8.

1.2. Objective of the Present Study

The primary target of this study is to fabricate high strength Au and Au alloys using electroplating techniques for the application in the MEMS devices. In order to achieve it, first I utilized three electroplating methods to fabricate the pure Au films and investigated their micro-mechanical properties using the micro-compression tests. After that, alloying in the Au by forming the Au–Cu alloys was investigated in order to achieve higher mechanical strength with the effect of the solid solution strengthening. Finally, the TEM will be used to observe the microstructure of the electrodeposited Au–Cu alloys, and the deformation behaviors will also be discussed.

1.3. Outline of This Study

In Chapter 2, three electroplating methods, including conventional electroplating (CONV-EP), pulse electroplating (PEP), and electroplating with $scCO_2$-contained

electrolyte (EP-SCE), were utilized to fabricate the pure Au films. The micro-mechanical properties of were evaluated by the micro-compression tests using the micro-pillars fabricated from the Au electrodeposits. Moreover, the sample size effects of the electrodeposited Au are also investigated.

In Chapter 3, Au–Cu alloys were fabricated by CONV-EP from a mixed electrolyte mainly containing Au sulfite and Cu sulfate. Current density, which is one of the most electroplating parameters, were varied in order to control the electrodeposit properties. Morphology, crystalline structure, and chemical composition were characterized using SEM, XRD, and EDS, respectively. The micro-mechanical properties of the electrodeposited Au–Cu alloys were also investigated.

In Chapter 4, PEP was utilized to fabricated the Au–Cu alloys. The pulse parameters such as pulse on and off-time were introduced to further control the film properties. In particular, the change of characteristics in the pulse-off time because of replacement reaction was described in details. The micro-mechanical properties were also investigated and compared with those of Au–Cu alloys fabricated by CONV-EP.

In Chapter 5, microstructure of the electrodeposited Au–Cu alloys was observed by transmission electron microscope. In particular, the deformation behaviors related to the mechanical properties was discussed in detail.

In Chapter 6, the present study is summarized.

1.4. References

[1] H. Seidel, H. Riedel, R. Kolbeck, G. Mück, W. Kupke, and M. Königer, Capacitive Silicon Accelerometer with Highly Symmetrical Design, Sens. Actuators A 21 (1990) 312–315.

[2] B. Ha, Y. Oh, and C. Song, A Capacitive Silicon Microaccelerometer with Force-Balancing Electrodes, Jpn. J. Appl. Phys. 37 (1998) 7052–7057.

[3] H. Okada, T. Kobayashi, T. Masuda, and T. Itoh, Ultra-Low Power Event-Driven Wireless Sensor Node Using Piezoelectric Accelerometer for Health Monitoring, Jpn. J. Appl. Phys. 48 (2009) 070222.

[4] R.E. Mayagoitia, A.V. Nene, P.H. Veltink, Accelerometer and Rate Gyroscope Measurement of Kinematics: An Inexpensive Alternative to Optical Motion Analysis Systems, J. Biomech. 35 (2002) 537–542.

[5] Y.-J. Hong, I.-J. Kim, S. C. Ahn, and H.-G. Kim, Mobile Health Monitoring System Based on Activity Recognition Using Accelerometer, Simul. Model. Pract. Theory 35 (2010) 446–455.

[6] J. Chae, H. Kulah, and K. Najafi, A Monolithic Three-Axis Micro-g Micromachined Silicon Capacitive Accelerometer, IEEE J. Microelectromech. Syst. 14 (2005) 235–242.

[7] R. Abdolvand, B.V. Amini, and F. Ayazi, Sub-Micro-Gravity In-Plane Accelerometers with Reduced Capacitive Gaps and Extra Seismic Mass, IEEE J. Microelectromech. Syst. 16 (2007) 1036–1043.

[8] M. Lemkin and B.E. Boser, A Three-Axis Micromachined Accelerometer with a CMOS Position-Sense Interface and Digital Offset-Trim, IEEE J. Solid-State Circuits 34 (1999) 456–468.

[9] H. Qu, D. Fang, and H. Xie, A Monolithic CMOS-MEMS 3-Axis Accelerometer with a Low-Noise, Low-Power Dual-Chopper Amplifier, IEEE Sens. J. 8 (2008) 1511–1518.

[10] Y.-C. Liu, M.-H. Tsai, T.-L. Tang, and W. Fang, Post-CMOS Selective Electroplating Technique for the Improvement of CMOS-MEMS Accelerometers, J. Micromech. Microeng. 21 (2011) 105005.

[11] Y. Chiu, H.-C. Hong, and P.-C. Wu, Development and Characterization of a CMOS-MEMS Accelerometer with Differential LC-Tank Oscillators, IEEE J. Microelectromech. Syst. 22 (2013) 1285–1295.

[12] D. Yamane, T. Konishi, T. Matsushima, K. Machida, H. Toshiyoshi, and K. Masu, Design of Sub-1g Microelectromechanical Systems Accelerometers, Appl. Phys. Lett. 104 (2014) 074102.

[13] K. Machida, T. Konishi, D. Yamane, H. Toshiyoshi, and K. Masu, Integrated CMOS-MEMS Technology and Its Applications, ECS Trans. 61 (2014) 21–39.

[14] D. Yamane, T. Matsushima, T. Konishi, H. Toshiyoshi, K. Masu, K. Machida, A Dual-Axis MEMS Capacitive Inertial Sensor with High-Density Proof Mass, Microsys. Technol. 22 (2015) 459–464.

[15] R.D. Emery and G.L. Povirk, Tensile Behavior of Free-Standing Gold Films. Part I. Coarse-Grained Films, Acta Mater. 51 (2003) 2067–2078.

[16] T. Tsuchiya, O. Tabata, J. Sakata, and Y. Taga, Specimen Size Effect on Tensile Strength of Surface-Micromachined Polycrystalline Silicon Thin Films, J. Microelectromech. Syst. 7 (1998) 106–113.

[17] D. Yamane, T. Konishi, T. Safu, K. Tachibana, M. Teranishi, C.-Y Chen, T.-F.M. Chang, M. Sone, K. Machida, and K. Masu, Long-Term Vibration Characteristics of

MEMS Inertial Sensors by Multi-Layer Metal Technology, in Proc. 19th International Conference on Solid-State Sensors, Kaohsiung, Taiwan, June 18-June 22, 2017.

[18] A.M. Rashidi and A. Amadeh, The Effect of Current Density on the Grain Size of Electrodeposited Nanocrystalline Nickel Coatings, Surf. Coat. Technol. 202 (2008) 3772–3776.

[19] A.M. Rashidi and A. Amadeh, The Effect of Saccharin Addition and Bath Temperature on the Grain Size of Nanocrystalline Nickel Coatings, Surf. Coat. Technol. 204 (2009) 353–358.

[20] N.J. Petch, The Cleavage Strength of Polycrystals, J. Iron Steel Inst. 174 (1953) 25–28.

[21] C.A. Schuh, T.G. Nieh, and H. Iwasaki, The Effect of Solid Solution W Additions on the Mechanical Properties of Nanocrystalline Ni, Acta Mater. 51 (2003) 431–443.

[22] Y. Li, H. Jiang, W. Huang, and H. Tian, Effects of Peak Current Density on the Mechanical Properties of Nanocrystalline Ni–Co Alloys Produced by Pulse Electrodeposition, Appl. Surf. Sci. 254 (2008) 6865–6869.

[23] C.K. Chung and W.T. Chang, Effect of Pulse Frequency and Current Density on Anomalous Composition and Nanomechanical Property of Electrodeposited Ni–Co Film, Thin Solid Films 517 (2009) 4800–4804.

[24] L. Chang, P.W. Kao, and C.-H. Chen, Strengthening Mechanisms in Electrodeposited Ni–P Alloys with Nanocrystalline Grains, Scripta Mater. 56 (2007) 713–716.

[25] N.Y.C. Yang, T.J. Headley, J.J. Kelly, and J.M. Hruby, Metallurgy of High Strength Ni–Mn Microsystems Fabricated by Electrodeposition, Scripta Mater. 51 (2004) 761–766.

[26] K. Maki, Y. Ito, H. Matsunaga, and H. Mori, Solid-Solution Copper Alloys with High Strength and High Electrical Conductivity, Scripta Mater. 68 (2013) 777–780.

[27] L. Lu, Y. Shen, X. Chen, L. Qian, and K. Lu, Ultrahigh Strength and High Electrical Conductivity in Copper, Science 304 (2004) 422–426.

[28] Y.F. Shen, L. Lu, Q.H. Lu, Z.H. Jin, and K. Lu, Tensile Properties of Copper with Nano-Scale Twins, Scripta Mater. 52 (2005) 989–994.

[29] B.Y.C. Wu, P.J. Ferreira, and C.A. Schuh, Nanostructured Ni-Co Alloys with Tailorable Grain Size and Twin Density, Metall. Mater. Trans. A 36A (2005) 1927–1936.

[30] T. Erdey-Gruz and M. Volmer, Zur Theorie der Wasserstoffüberspannung, Z. Phys. Chem. A 150 (1930) 203.

[31] H. Natter, T. Krajewski, and R. Hempelmann, Nanocrystalline Palladium by Pulsed Electrodeposition, Ber. Bunsenges. Phys. Chem. 100 (1996) 55–64.

[32] M.S. Youssef, C.C. Koch, and P.S. Fedkiw, Influence of Additives and Pulse Electrodeposition Parameters on Production of Nanocrystalline Zinc from Zinc Chloride Electrolytes, J. Electrochem. Soc. 151 (2004) C103-C111.

[33] M.S. Youssef, C.C. Koch, and P.S. Fedkiw, Influence of Pulse Plating Parameters on the Synthesis and Preferred Orientation of Nanocrystalline Zinc from Zinc Sulfate Electrolytes, Electrochim. Acta 54 (2008) 677–683.

[34] B. Tury, M. Lakatos-Varsanyi, and S. Roy, Effect of Pulse Parameters on the Passive Layer Formation on Pulse Plated Ni–Co Alloys, Appl. Surf. Sci. 253 (2007) 3103.

[35] L.M. Chang, M.Z. An, H.F. Guo, and S.Y. Shi, Microstructure and Properties of Ni–Co/Nano-Al_2O_3 Composite Coatings by Pulse Reversal Current Electrodeposition, Appl. Surf. Sci. 253 (2006) 2132.

[36] J. Ke, W. Su, S.M. Howdle, M.W. George, D. Cook, M. Perdjon-Abel, P.N. Bartlett, W. Zhang, F. Cheng, W. Levason, G. Reid, J. Hyde, J. Wilson, D.C. Smith, K. Mallik, and P. Sazio, Electrodeposition of Metals from Supercritical Fluids, PNAS 106 (2009) 14768–14772.

[37] W.L. Tsai, P.C. Hsu, Y. Hwu, C.H. Chen, L.W. Chang, J.H. Je, H.M. Lin, A. Groso, and G. Margaritondo, Building on Bubbles in Metal Electrodeposition, Nature 417 (2002) 139.

[38] H. Yoshida, M. Sone, H. Wakabayashi, H. Yan, K. Abe, X.T. Tao, A. Mizushima, S. Ichihara, and S. Miyata, New Electroplating Method of Nickel in Emulsion of Supercritical Carbon Dioxide and Electroplating Solution to Enhance Uniformity and Hardness of Plated Film, Thin Solid Films 446 (2004) 194–199.

[39] T.-F.M. Chang, M. Sone, A. Shibata, C. Ishiyama, and Y Higo, Bright Nickel Film Deposited by Supercritical Carbon Dioxide Emulsion Using Additive-Free Watts Bath, Electrochim. Acta 55 (2010) 6469–6475.

[40] S.M. Howdle, V.N. Bagratashvil, The Effects of Fluid Density on the Rotational Raman Spectrum of Hydrogen Dissolved in Supercritical Carbon Dioxide, Chem. Phys. Lett. 214 (1993) 215–219.

[41] T. Shimizu, N. Shinoda, T.-F.M. Chang, A. Shibata, and M. Sone, Crystal Growth on Novel Cu Electroplating Using Suspension of Supercritical CO_2 in Electrolyte with Cu Particles, Surf. Coat. Technol. 231 (2013) 77–80.

[42] M. Tanabe, T.-F.M. Chang, H. Hosoda, T. Sato, and M. Sone, Electrodeposition of Tin Using Supercritical Carbon Dioxide Emulsions, ECS Electrochem. Lett. 3 (2014) D44–D45.

[43] X. Luo, C.-Y. Chen, T.-F.M. Chang, H. Hosoda, and M. Sone, Crystal Growth of

Cobalt Film Fabricated by Electrodeposition with Dense Carbon Dioxide, J. Electrochem. Soc. 162 (2015) D423–D426.

[44] M.D. Uchic, D.M. Dimiduk, J.N. Florando, and W.D. Nix, Sample Dimensions Influence Strength and Crystal Plasticity, Science 305 (2004) 986–989.

[45] J.R. Greer, W.C. Oliver, and W.D. Nix, Size Dependence of Mechanical Properties of Gold at the Micron Scale in the Absence of Strain Gradients, Acta Mater. 53 (2005) 1821–1830.

[46] J.R. Greer, C.R. Weinberger, and W Cai, Comparing the Strength of F.c.c. and B.c.c. Sub-Micrometer Pillars: Compression Experiments and Dislocation Dynamics Simulations, Mater. Sci. Eng. A 493 (2008) 21–25

[47] M.D. Uchic, P.A. Shade, and D.M. Dimiduk, Plasticity of Micrometer-Scale Single Crystals in Compression, Annu. Rev. Mater. Res. 39 (2009) 361–386.

[48] J.R. Greer and J.Th.M. De Hosson, Plasticity in Small-Sized Metallic Systems: Intrinsic Versus Extrinsic Size Effect, Prog. Mater. Sci. 56 (2011) 654–724.

[49] M. Dietiker, S. Buzzi, G. Pigozzi, J.F. Löffler, and R. Spolenak, Deformation Behavior of Gold Nano-Pillars Prepared by Nanoimprinting and Focused Ion-Beam Milling, Acta Materialia 59 (2011) 2180–2192.

[50] T. Nagoshi, T.-F.M. Chang, S. Tatsuo, and M. Sone, Mechanical Properties of Nickel Fabricated by Electroplating with Supercritical CO_2 Emulsion Evaluated by Micro-Compression Test Using Non-Tapered Micro-Sized Pillar, Microelectron. Eng. 110 (2013) 270–273.

[51] A.B. Hagen and C. Thaulow, Low Temperature In-Situ Micro-Compression Testing of Iron pPillars, Mater. Sci. Eng. A 678 (2016) 355–364.

[52] S. Cheng, X.L. Wang, H. Choo, and P.K. Liaw, Global Melting of $Zr_{57}Ti_5Ni_8Cu_{20}Al_{10}$

Bulk Metallic Glass Under Microcompression, Appl. Phys. Lett. 91 (2007) 201917.

[53] B.E. Schuster, Q. Wei, T.C. Hufnagel, and K.T. Ramesh, Microcompression of Nanocrystalline Nickel, Scripta Mater. 56 (2008) 5091–5100.

[54] A. Rinaldi, P. Peralta, C. Friesen, and K. Sieradzki, Sample-Size Effects in the Yield Behavior of Nanocrystalline Nickel, Acta Mater. 56 (2008) 511–517.

[55] R. Fritz, V. Maier-Kiener, D. Lutz, and D. Kiener, Interplay Between Sample Size and Grain Size: Single Crystalline vs. Ultrafine-Grained Chromium Micropillars, Mater. Sci. Eng. A 674 (2016) 626–633.

[56] D. Jang and J.R. Greer, Size-Induced Weakening and Grain Boundary-Assisted Deformation in 60 nm Grained Ni Nanopillars, Scripta Mater. 64 (2011) 77–80.

[57] C. Howard, D. Frazer, A. Lupinacci, S. Parker, R.Z. Valiev, C. Shin, B.W. Choi, and P. Hosemann, Investigation of Specimen Size Effects by In-Situ Microcompression of Equal Channel Angular Pressed Copper, Mater. Sci. Eng. A 649 (2016) 104–113.

[58] H. Kinashi, T. Nagoshi, T.-F.M. Chang, T. Sato, and M. Sone, Mechanical Properties of Cu Electroplated in Supercritical CO_2 Emulsion Evaluated by micro-compression test, Microelectron. Eng. 121 (2014) 83–86.

[59] A. Shibata, T. Nagoshi, M. Sone, and Y. Higo, Micromechanical Characterization of Deformation Behavior in Ferrous Lath Martensite, J. Alloy. Comp. 577S (2013) S555–S558.

[60] Y. Kihara, T. Nagoshi, T.-F.M. Chang, H. Hosoda, S. Tatsuo, and M. Sone, Tensile Behavior of Micro-Sized Specimen Made of Single Crystalline Nickel, Mater. Lett. 153 (2015) 36–39.

[61] J.R. Greer, Nanotwinned Metals: It's All About Imperfections, Nat. Mater. 12 (2013) 689–690.

1.5. Figures

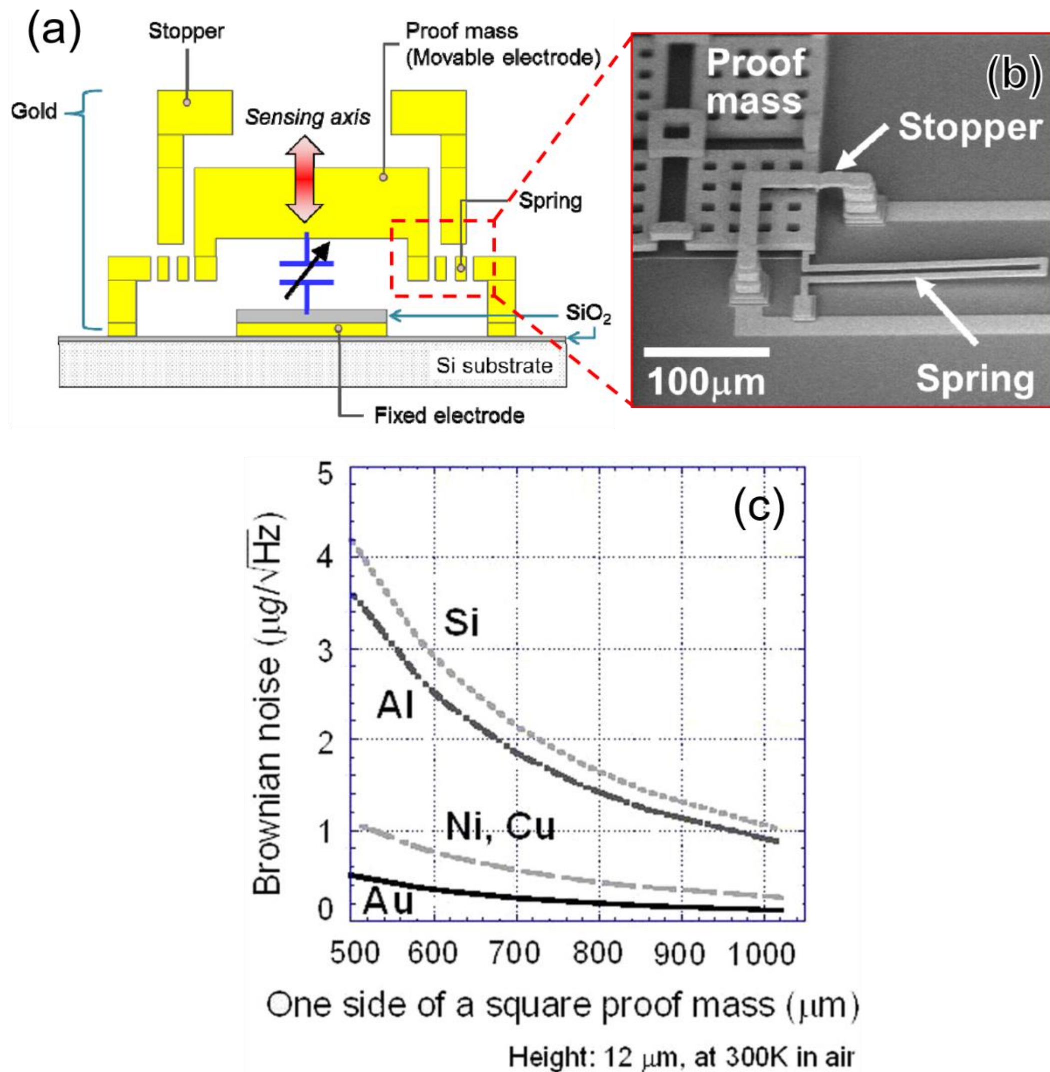

FIG. 1.1. (a) Schematic design of a MEMS capacitive accelerometer for sub-1g sensing. (b) SEM image of the MEMS accelerometers in the boxed region of (a). (c) Analytical modeling of Brownian noise on several proof mass materials [12,13].

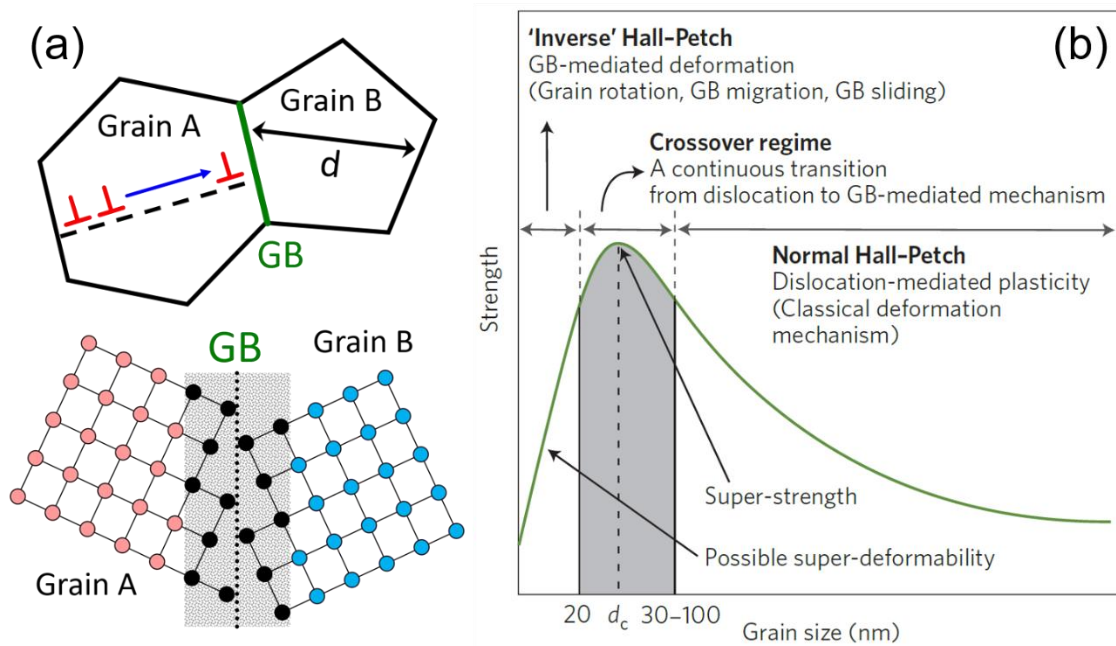

FIG. 1.2. (a) Illustration of grain boundary strengthening. (B) Two-dimensional representations of a typical grain boundary. (c) Schematic of a Hall–Petch plot, which shows material strength as a function of grain size [61].

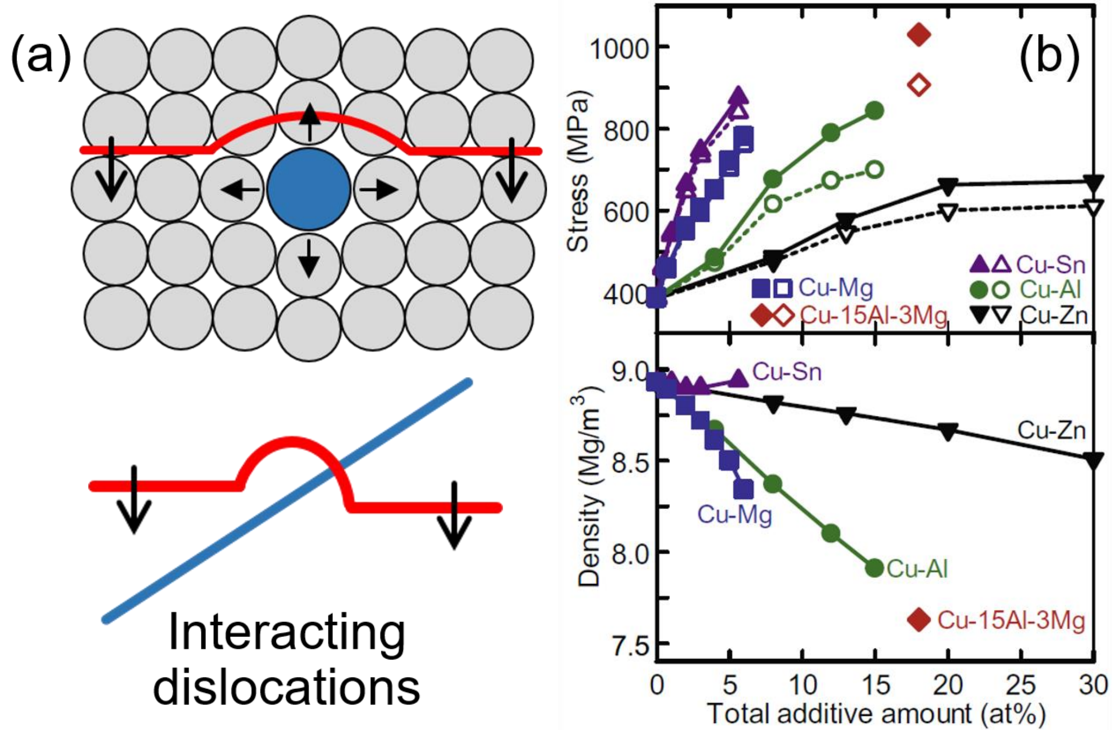

FIG. 1.3. (a) Illustration of solute atoms interacting with the dislocations. (b) The yield strength and density as a function of solution concentration in Cu alloys [26].

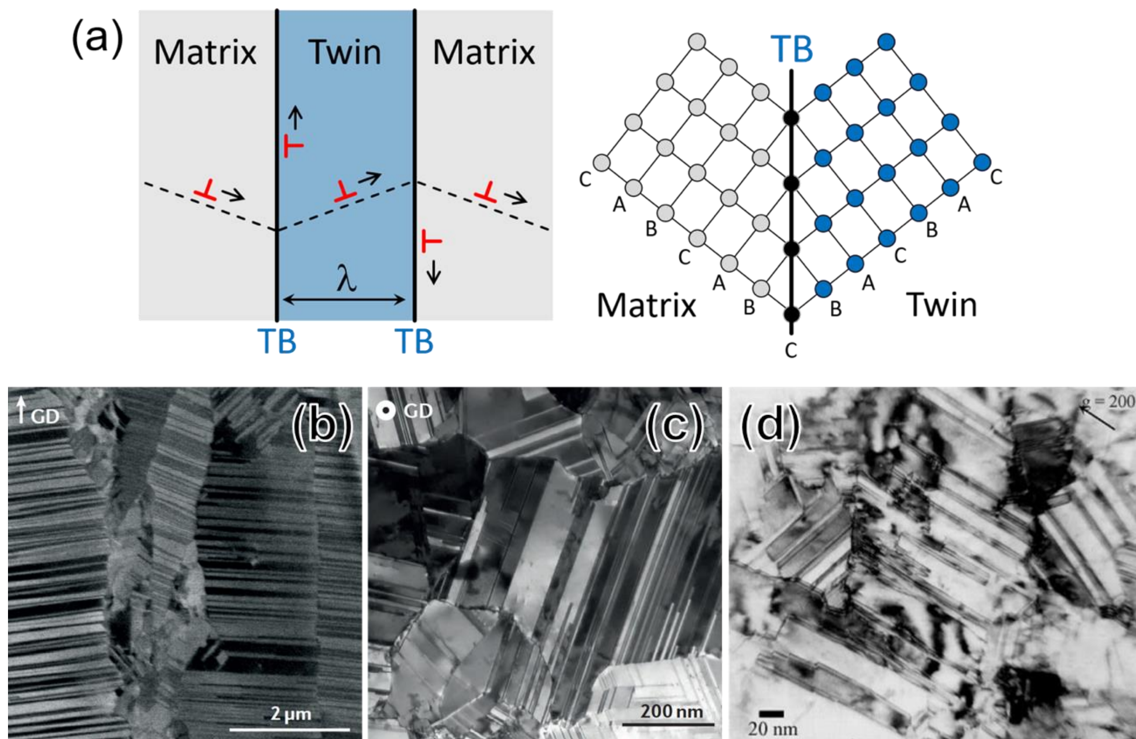

FIG. 1.4. (a) Schematic of twin boundary strengthening. The coherent twin boundary works same as the conventional high-angel grain boundary to obstruct the dislocation motion. (a,b) Pulse electrodeposited Cu showing high density nanotwins [27]. (c) Nanotwinned structure in Ni–Mn alloys [29].

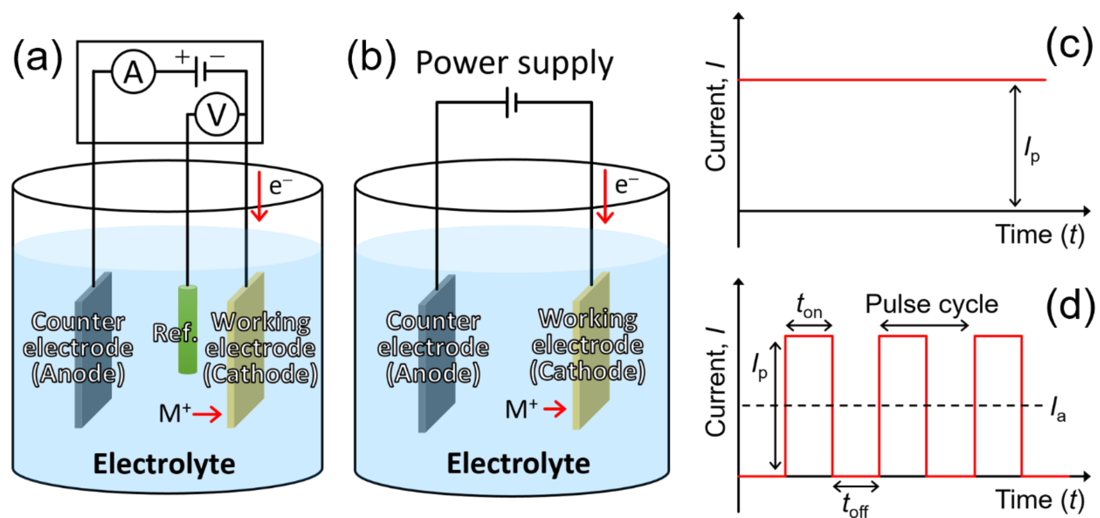

FIG. 1.5. (a,b) Electrodeposition with potentiostatic mode and galvanostatic mode, respectively. (c,d) Schematics of direct constant current and pulse current, respectively.

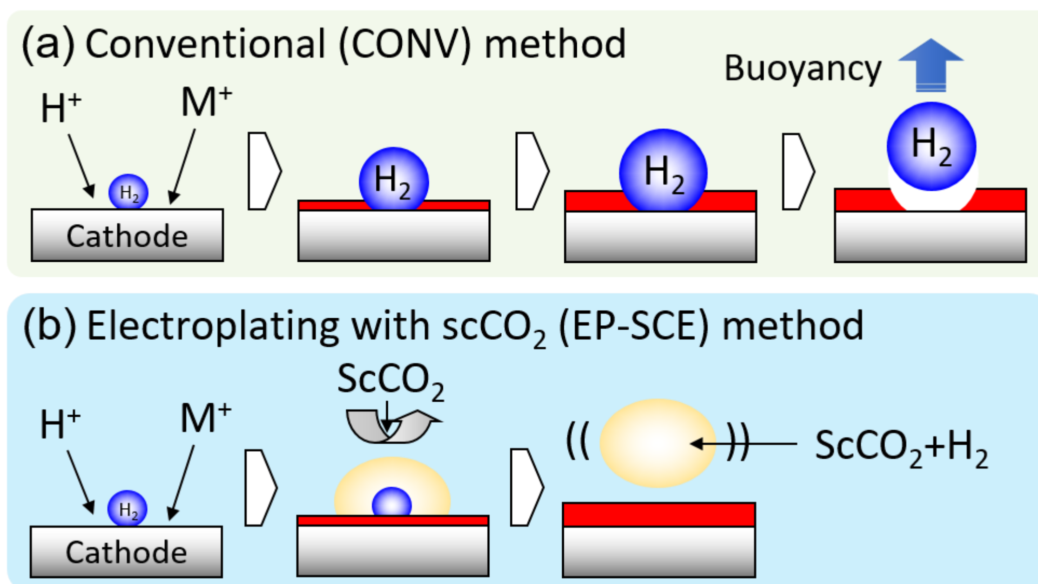

FIG. 1.6. Illustration of how the hydrogen evolution affects the morphology of electrodeposits. (a) Defects caused by the hydrogen evolution in conventional electroplating in acid electrolyte. (b) Desorption of hydrogen by $scCO_2$ introduced in the electroplating process.

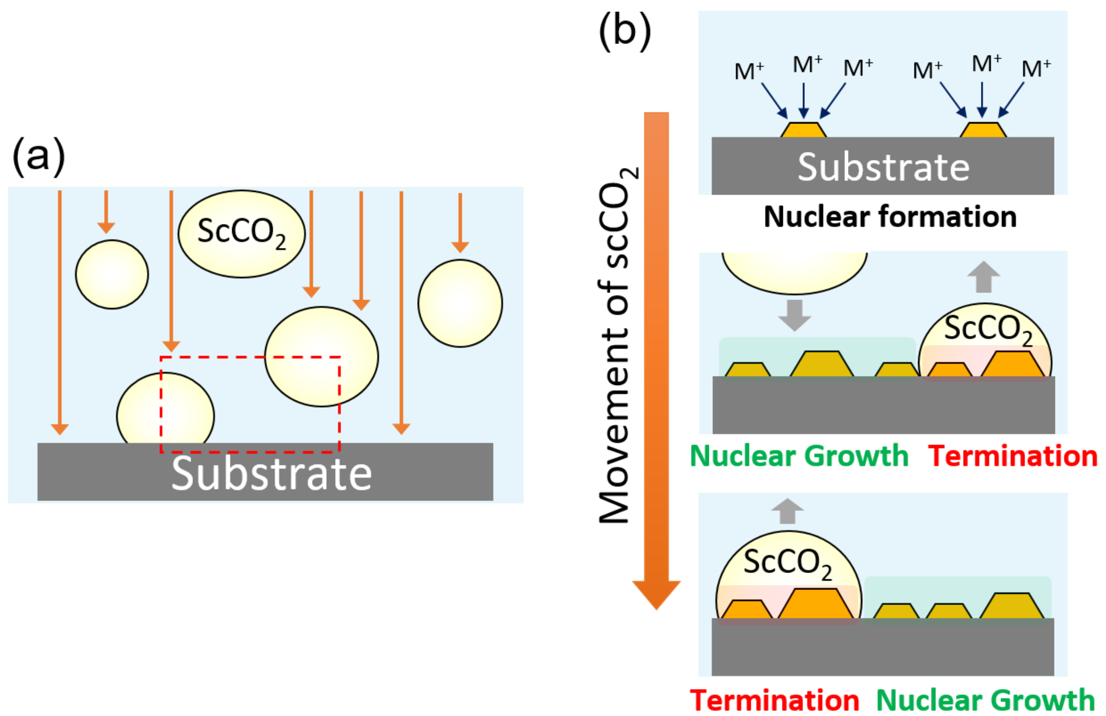

FIG. 1.7. (a) Schematic of periodic-plating-characteristic mechanism. (b) Dynamic illustration of $scCO_2$ in the boxed region of (a) [39].

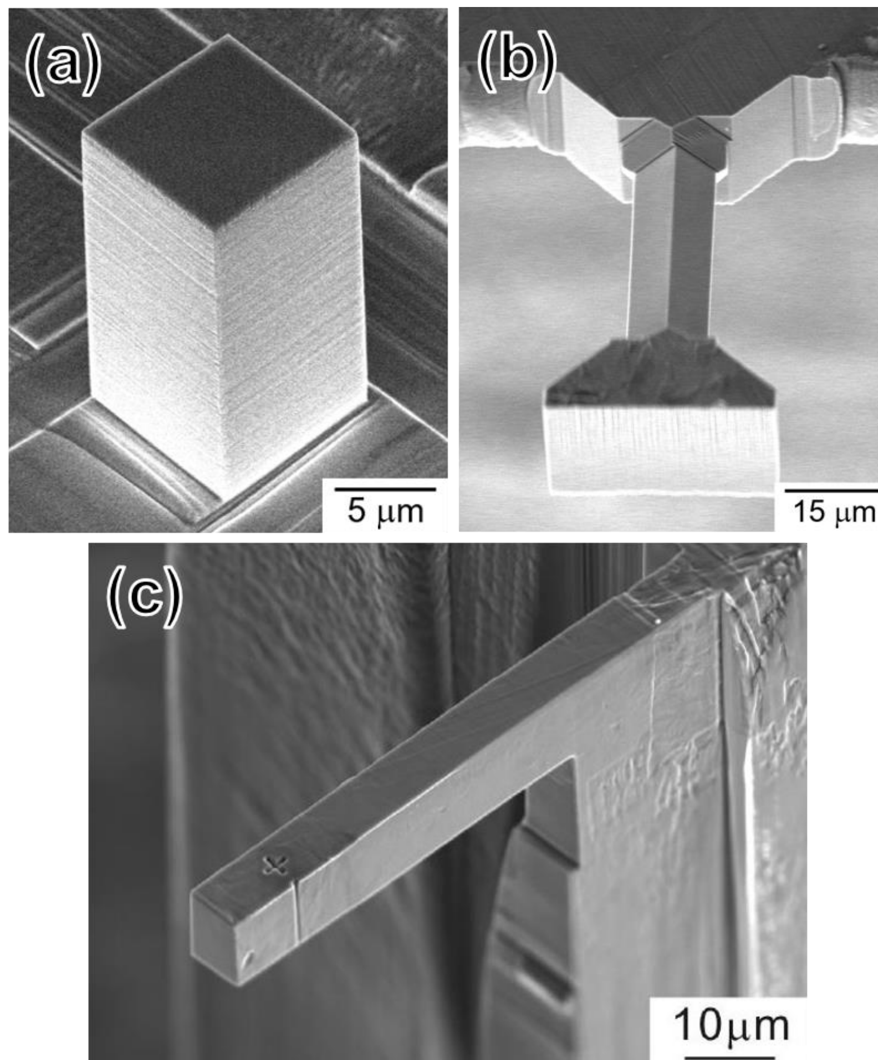

Fig. 1.8. FIB-fabricated micro-specimens for the micro-mechanical tests. (a) Micro-pillar [50], (b) micro-tensile specimen [59], and (c) micro-cantilever [60].

CHAPTER 2

Fabrication of Ultrafine-Grained Au by Electroplating Techniques

2.1. Introduction

In past few decades, gold (Au) materials have attracted much attentions and are widely used in micro-electronic industries because of their outstanding properties such as high chemical stability, corrosion resistance, electrical conductivity, and density [1,2]. Among the fabrication methods, electroplating (EP) is extensively applied in fabrication of the Au materials used in micro-electrical-mechanical system (MEMS) devices, i.e., capacitive accelerometers [3]. However, the mechanical strength of Au is relatively low (i.e., yield strength of bulk Au: 50–200 MPa [4]) when compared with other metallic materials, which has been a concern in practical applications in MEMS especially when used as the movable components. Strengthening by grain refinement is a typical method to enhance the mechanical strength of metallic materials based on the Hall–Petch relationship [5]. As the grain size reaches submicron- or nano-scale, high strength can be obtained when compared to coarse-grained metals with the same chemical composition and phase constitution [6,7].

Grain size control is a fascinating feature in the EP by appropriately adjusting the deposition parameters such as the current density, pH value, plating bath temperature, etc. [8]. For example, an increase in the current density can lead to a decrease in the grain

size, and therefore, enhances the mechanical strength. However, the film composition could be varied because of side-reactions, defects could be formed in the film, and the current efficiency would be low when the current density is too high. An alternative EP method employing a constant current density and a supercritical carbon dioxide ($scCO_2$) contained electrolyte was reported to be effective to give the grain refinement effect as demonstrated in electroplating of Ni and Cu [9,10]. Moreover, the specific properties of $scCO_2$ can promote transfer of materials into confined spaces and removal of H_2 gas bubbles away from the cathode, which allow application of high current density while keeping a defect- and pinhole-free plating at the same time [11–13]. In addition, co-deposition of carbon was reported in electroplating with an electrolyte containing $scCO_2$ (EP-SCE) at high pressure [14,15]. The co-deposited carbon would precipitate at the grain boundary to suppress the occurrence of the inverse Hall–Petch Relationship [14,16] and reduce the grain boundary mobility [17], which is very effective in stabilizing the nanocrystalline structures to maintain the high mechanical strength. With these advantages, mechanical strength of the electroplated Au films in is expected to be enhanced by introducing $scCO_2$ into the EP process. On the other hand, pulse electroplating (PEP) has been reported to be effective in fabricating electrodeposits with finer grains, higher uniformity, and lower porosity [18–20]. An increase in the nuclei density because of the higher instantaneous current density in pulse on-time could be achieved to obtain electroplated films with finer grains. Also, it is possible to control the composition and the film thickness by regulating the pulse amplitude and width.

Mechanical properties of materials having dimensions in micro-scale are different from those of bulk materials. The phenomenon is known as the sample size effect. Since the first report of the sample size effect in single crystal specimens [21], many

subsequent investigations have demonstrated the effect in the mechanical strength of specimens composed of fcc and bcc metals when dimensions of the specimen are decreased to micro- or nano-scale [22,23]. For polycrystalline specimens, there are limited reports on the sample size effect [24–26], especially for specimens composed of Au and having dimensions in micro-scale. Components in MEMS devices often have dimensions in micrometer or tens of micrometer order. For practical applications in fabrication of components used in MEMS devices, it is necessary to evaluate the mechanical property using specimens having dimensions in micro-scale.

In this chapter, three EP methods including galvanostatic conventional EP (CONV-EP), EP-SCE and PEP were utilized to fabricate the Au films. Micro-mechanical properties of the electrodeposited Au films were evaluated by micro-compression tests using the non-tapered micro-sized pillars with a square cross-section. The Au micro-pillars were fabricated from the Au electrodeposits by focus ion beam (FIB). Furthermore, the sample size effects were investigated from the Au films with various dimensions. Micro-compression tests with a displacement controlled mode would be applied to evaluate the mechanical property.

2.2. Experimental

2.2.1. Electroplating of Au Films

The Au electrolyte used in this work was a commercially available sulfite-based electrolyte provided by METEX Corporation, Japan, which contained 50 g/L of Na_2SO_3, 50 of g/L $(NH_4)_2SO_3$, 10 g/L of Au, and 5 % sodium gluconate with pH of 8.0. Cu plates and Pt plates were used as the cathode and anode, respectively. Three electroplating methods were utilized to fabricate the Au films: CONV-EP, PEP, and EPSCE. For CONV-

EP, the current density is fixed at 5 mA/cm^2. For the PEP, the pulsed current density was 10 mA/cm2, and the off-time current density was 0 mA/cm^2. The current on-time (t_{on}) and the current off-time (t_{off}) of the PEP were fixed at 10 ms as the optimized parameter. The average current density is 5 mA/cm^2, which is the same as CONV-EP. For the EP-SCE, 20 vol.% of CO_2 with respect to the overall volume of the reaction chamber was used. The pressure was controlled at 10 MPa during the entire EP-SCE process. The EP-SCE process is illustrated in Fig. 2.1 [9]. The current density utilized in the EP-SCE is same with the CONV-EP. The plating temperature was maintained at 40 ± 1 °C for all electroplating processes.

2.2.2. Characterization and Micro-Compression Tests

Crystalline structures of the electrodeposited Au films were characterized using grazing incidence X-ray diffraction (GIXRD, Rigaku Ultima) at a glancing angle of 3°. The scan ranged from 2θ = 30° to 80° with a step size of 0.02°, and the scan rate was 2 °/min. Micro-size compression pillars were fabricated from the electrodeposited Au films prepared by three electroplating methods (CONV-EP, PEP, and EP-SCE) with a film thickness of ~50 μm. FIB (FB2100, Hitachi) was utilized to fabricate the non-tapered Au micro-pillars. Dimensions of the micro-pillars were 10×10×20 μm^3 for all Au electrodeposits. To investigate the sample size effects, the micro-pillars with the dimensions of 15×15×30 and 20×20×40 μm^3 were further fabricated from the CONV-EP and EP-SCE films. Micro-compression tests were conducted with a testing machine specially designed for micro-size specimens, which a diamond flat-punch indenter equipped to a load cell was used as the compression platen [14]. The micro-compression was controlled at a constant displacement rate of 0.1 μm/s using a piezo-electric actuator.

The illustrations of micro-pillar fabrication process and micro-compression test are shown in Fig. 2.2. Deformation behaviors of the Au micro-pillars after the micro-compression tests were observed by a scanning electron microscope (SU4300SE, Hitachi) and a scanning ion microscope (SIM) equipped in the FIB. The engineering strain-stress (*SS*) curves were subsequently converted by the following equations:

$$\sigma = P/A_0 \tag{2-1}$$

$$\varepsilon = L/L_0 \tag{2-2}$$

where σ is the engineering stress, P is the load, A_0 is area of top surface of the micro-pillar before compression, ε is the engineering strain, L is the displacement, L_0 is the length of micro-pillar. Grain boundary characteristics of the pillar surface normal to the compression axis were examined by electron backscatter diffraction (EBSD, INCA Crystal software, Oxford Instruments) installed in a SEM, and carbon content in the Au films was examined by energy-dispersive X-ray spectroscopy (EDS) equipped in the same SEM.

2.3. Results and Discussion

2.3.1. Crystalline Structure and Composition of Electrodeposited Au Films

Fig. 2.3 shows the GIXRD patterns of three Au films fabricated by CONV-EP, PEP, and EP-SCE methods. All films exhibit the characteristic peaks corresponding to the (111), (200), (220), and (311) planes of metallic face-centered cubic (fcc) Au. The major diffraction peak is (111) for both Au films, which is because the surface energy of the (111) crystal growth orientation is the lowest when compared with other crystal orientations [21]. On the other hand, the diffraction peaks of the PEP and the EP-SCE films are broader than those of the CONV-EP film. The d_g estimated from the GIXRD

patterns and Scherrer equation are ~22 nm for CONV-EP film, and ~13 nm for PEP and EP-SCE films. The finer d_g in the PEP can be attributed the higher pulse current density which results in an increase of nucleation rate during the on-time. On the other hand, the grain refinement effect in the EP-SCE Au film is suggested to be contributed by the same phenomena observed in electrodeposition of Ni, which are the periodic-plating-characteristics (PPC) [11] and the co-deposited carbon contents [14]. The EDS result showed that the carbon content in the EP-SCE film was 39.92 ± 2.02 at.%, which was higher than that in the CONV-EP film (29.63 ± 3.11 at.%). The co-deposited carbon would directly contribute to the grain refinement effect and immobilize movement of the grain boundaries [19], which is especially important in maintaining the ultra-fine grain structure since the mechanical strength is closely related to the grain size. The hydrobaric effect, which is the effect of pressure on crystal structure of the materials electrodeposited in an aqueous electrolyte, is also expected to have influences on the Au crystal structure [27].

2.3.2. Deformation Behaviors of Au Micro-Pillars

Fig. 2.4 shows SIM images of the micro-pillars fabricated from the electrodeposited Au thick films before and after the micro-compression tests. The CONV-EP pillar showed camouflage-like patterns on the side-surface, where clear boundaries along the patterns with different level of brightness would be the grain boundaries. On the other hand, inconspicuous grain boundaries were observed on the surface of both PEP and EP-SCE Au pillars, which implied the d_g was finer than ca. 1 μm [28]. After the micro-compression test, barrel-shape deformation was observed in the middle part of all micro-pillars. The deformation following the slips of grain boundaries or formation of barrel-shape is well recognized to be the typical characteristics of the deformation of poly-

and nano-crystalline structures [29]. These results confirmed the polycrystalline structure in the three micro-pillars. In addition to the rough observation of grain size from SIM, EBSD measurement was conducted to confirm the grain size distribution in the Au films. Fig. 2.5(a) shows the orientation map of the CONV-EP pillar determined from the EBSD analysis. The grains randomly distribute with a wide range of various orientations, and no obviously preferred-growth orientation was observed. The corresponding grain size distribution is summarized in Fig. 2.5(b), which the d_g ranged from few hundred nanometers to 1–2 μm with an average of ~0.8 μm. It should be noticed that grains size of the EP-SCE Au was too small to be determined by EBSD measurement; therefore, the average d_g of the EP-SCE Au was estimated from the GIXRD pattern (Fig. 2.3) using the Scherrer equation. The estimated average d_g of the PEP and the EP-SCE Au was extremely small of ~13 nm, which was far smaller than that of the CONV-EP Au.

2.3.3. Micro-Mechanical Properties of Au Micro-Pillars

Mechanical strengths of the Au films were determined from engineering *SS* curves generated from the micro-compression tests. Fig. 2.6 shows the *SS* curves of the CONV-EP and the EP-SCE micro-pillars. The σ_y of CONV-EP pillar was estimated to be 380 MPa, which was determined by the cross-point of the *SS* curve and 0.2 % offset line of the elastic deformation region. The σ_y obtained from the PEP and the EP-SCE pillar was evaluated to be 540 MPa and 520 MPa, respectively. Moreover, the compressive flow stress also reached ~800 MPa for the PEP and the EP-SCE pillars, further suggesting that mechanical properties of electroplated Au can be enhanced by employing these two methods. The significant enhancement of the mechanical properties in the PEP and the EP-SCE Au pillars could be explained by the Hall-Petch relationship [5], that is, strength

of polycrystalline metallic materials is enhanced following a decrease in the grain size. As confirmed by the GIXRD patterns (Fig. 2.3) and the SIM images (Fig. 2.4), both the PEP and the EP-SCE Au films had a finer d_g when compared with the CONV-EP film. It is worth noting that the high mechanical strength is attributed to the ultra-fine grains. For the EP-SCE, the PPC, the hydrobaric effect, and the high carbon content could all contribute to the grain refinement effect. Besides, the high carbon content suggests that the EP-SCE films are promising electronic materials for the fabrication process involving heat treatment since the grain growth would be suppressed.

2.3.4. Mechanical Properties of the Au Pillars with Different Dimensions

Considering dimensions of the components in MEMS devices, mechanical properties of pillars having dimensions in 15×15×30 μm^3 and 10×10×20 μm^3 fabricated from the CONV-EP and the EP-SCE Au films were also evaluated. Fig. 2.7 shows three Au pillars fabricated from the CONV-EP and the EP-SCE films with different pillar size before and after the compression tests. All the three pillars exhibited the same barrel-shape deformation behavior as well as the Au pillars observed in Fig. 2.4.

Fig. 2.8(a) and (b) shows *SS* curves of the CONV and the EP-DCE pillars with dimensions ranged from 10×10×20 to 20×20×40 μm^3, respectively. An increase in the σ_f in the plastic deformation region with a decrease in the sample size was observed. In a study on micro-pillars composed of nanocrystalline Ni having the d_g at 8 nm, an increase in the σ_f is reported when the pillar cross-sectional area is decreased from 900 to 25 μm^2 [24]. The dependency of mechanical properties on the diameter or cross-sectional area of the samples evaluated is known as the sample size effect. In this study, the micro-pillars evaluated were also composed of metallic crystals having the d_g in nano-scale, and an

enhancement in the strength was observed when the cross-section area decreased from 400 to 100 μm^2, which indicated the sample size effect in the EP-SCE pillars. The stress as a function in log scale of the pillar size (l, length of a side of the square cross-section) for the EP-SCE gold was plotted to further clarify the sample size effect, as shown in Fig. 2.8(c). Rinaldi et al. [30] reported that compressive stresses of Ni pillars composed of nanocrystals exhibit an inverse power-law relationship with the diameter (D), $\sigma \propto D^{-\beta}$, where the value of β ranges from 0.38 to 0.66. Similar trends between the stresses with square root of the cross-sectional area, which is diameter of a pillar having circular cross-section or length of one side of a pillar having square cross-section as in this study, are reported in other literature [24,31]. As shown in Fig. 2.8(c), the σ_f increased from 740 to 810 MPa when the l scales down from 20 to 10 μm, and the exponent is about –0.13, which gives $\sigma_f \propto l^{-0.13}$.

Mechanical properties determined from SS curves can be affected by the strain rate as reported in the literature, especially for nanocrystalline face-centered cubic metals, which the strength is reported to have an inverse power-law relationship with the strain rate, $\sigma \propto (\text{strain rate})^{-m}$, and the m value is the strain rate sensitivity reported in the range from 0.01 to 0.03 in nanocrystalline fcc metals [32–35]. In this study, the compression tests conducted were displacement rate controlled at 0.1 μm/s. Heights of the pillars evaluated were ranged from 40 to 20 μm, and the strain rate would be varied from 2.5×10^{-3} to 5.0×10^{-3} s^{-1}. Using the m value at 0.03, a ~2.1% increase in the strength is expected when the strain rate is increased from 2.5×10^{-3} to 5.0×10^{-3} s^{-1}. In this study, the σ_f of EP-SCE pillars increased from 740 to 810 MPa when the strain rate was increased from 2.5×10^{-3} to 5.0×10^{-3} s^{-1}, which is a ~9.5% increase in the strength. Therefore, the increase in the σ_f is suggested to be mainly contributed by the sample size effect.

On the other hand, there was almost no variation in the σ_y as the l changed, which remained at 520 MPa. For the sample size effect on the σ_y, ratio of the l to the d_g is important. The sample size effect on the σ_y is suggested to be observable when the l/d_g ratio is between 5~10 [25,35,36]. In this study, d_g of the EP-SCE gold film was finer than 100 nm and would lead to a ratio of $l/d_g \geq 100$ when the l was larger than 10 μm. This should be the main reason why the sample size effect showed insignificant influence on the σ_y.

2.4. Conclusions

An enhancement in the mechanical properties of the Au films fabricated by the PEP and the EP-SCE was confirmed by micro-compression tests in this study. Also, grain refinement effect was observed in the Au films prepared by the PEP and the EP-SCE. Also, a high carbon content was observed in the EP-SCE film, which was one of the causes of the grain refinement effect. The yield strength and compressive flow stress of the EP-SCE micro-pillar with dimensions of 10×10×20 μm^3 reached 520 MPa and ~800 MPa, respectively. The fine grains were suggested to be the main cause of the enhancement in the mechanical properties based on the grain-boundary hardening mechanism known as the Hall-Petch relationship. For the EP-SCE pillars with different pillar dimensions, the σ_f increased from 740 to 810 MPa with a decrease in the pillar dimensions from 20×20×40 μm^3 to 10×10×20 μm^3. The strengthening observation confirmed the sample size effect on mechanical properties of micro-pillars composed of Au crystals having an average grain size in the nano-scale. The present study demonstrated the alternative EP methods in the fabrication of Au materials with improved mechanical properties for applications in electronic devices such as MEMS devices.

2.5. References

[1] Y. Okinaka and M. Hoshino, Some Recent Topics in Gold Plating for Electronics Applications, Gold Bull. 31 (1998) 3–13.

[2] T.A. Green, Gold Electrodeposition for Microelectronic, Optoelectronic and Microsystem Applications, Gold Bull. 40 (2007) 105–114.

[3] D. Yamane, T. Konishi, T. Matsushima, K. Machida, H. Toshiyoshi, and K. Masu, Design of Sub-1g Microelectromechanical Systems Accelerometers, Appl. Phys. Lett. 104 (2014) 074102.

[4] R.D. Emery and G.L. Povirk, Tensile Behavior of Free-Standing Gold Films. Part I. Coarse-Grained Films, Acta Mater. 51 (2003) 2067–2078.

[5] N.J. Petch, The Cleavage Strength of Polycrystals, J. Iron Steel Inst., 174 (1953) 25-28.

[6] Y. Wang, M. Chen, F. Zhou, and E. Ma, High Tensile Ductility in a Nanostructured Metal, Nature 419 (2002) 912–915.

[7] S. Cheng, E. Ma, Y. Wang, L. Kecskes, K. Youssef, C. Koch, U. Trociewitz, and K. Han, Tensile Properties of In Situ Consolidated Nanocrystalline Cu, Acta Mater. 53 (2005) 1521–1533.

[8] M. Stern and A.L. Geary, Electrochemical Polarization: I. A Theoretical Analysis of the Shape of Polarization Curves, J. Electrochem. Soc. 104 (1957) 56–63.

[9] T.-F.M. Chang, M. Sone, A. Shibata, C. Ishiyama, and Y Higo, Bright Nickel Film Deposited by Supercritical Carbon Dioxide Emulsion Using Additive-Free Watts Bath, Electrochim. Acta 55 (2010) 6469–6475.

[10] T.-F.M. Chang, T. Shimizu, C. Ishiyama, and M. Sone, Effects of Pressure on Electroplating of Copper Using Supercritical Carbon Dioxide Emulsified Electrolyte,

Thin Solid Films 529 (2013) 25–28.

[11] T.-F.M. Chang, T. Tasaki, C. Ishiyama, and M. Sone, Defect-Free Nickel Micropillars Fabricated at a High Current Density by Application of a Supercritical Carbon Dioxide Emulsion, Ind. Eng. Chem. Res. 50 (2011) 8080–8085.

[12] J. Ke, W. Su, S.M. Howdle, M.W. George, D. Cook, M. Perdjon-Abel, P.N. Bartlett, W. Zhang, F. Cheng, W. Levason, G. Reid, J. Hyde, J. Wilson, D.C. Smith, K. Mallik, and P. Sazio, Electrodeposition of Metals from Supercritical Fluids, PNAS 106 (2009) 14768–14772.

[13] J.M. Blackburn, D.P. Long, A. Cabanas, and J.J. Watkins, Deposition of Conformal Copper and Nickel Films from Supercritical Carbon Dioxide, Science 294 (2001) 141–145.

[14] T. Nagoshi, T.-F.M. Chang, S. Tatsuo, and M. Sone, Mechanical Properties of Nickel Fabricated by Electroplating with Supercritical CO_2 Emulsion Evaluated by Micro-Compression Test Using Non-Tapered Micro-Sized Pillar, Microelectron. Eng. 110 (2013) 270–273.

[15] S.-T. Chung and W.-T. Tsai, Nanocrystalline Ni–C Electrodeposits Prepared in Electrolytes Containing Supercritical Carbon Dioxide, J. Electrochem. Soc. 156 (2009) D457–D461.

[16] T.G. Nieh and J. Wadsworth, Hall-Petch Relation in Nanocrystalline Solids, Scripta Metall. Mater. 25 (1991) 955–958.

[17] T. Nagoshi, T.-F. M. Chang, T. Sato, and M. Sone, Effect of Annealing on Mechanical Properties of Nickel Electrodeposited Using Supercritical CO_2 Emulsion Evaluated by Micro-Compression Test, Microelectron. Eng. 153 (2016) 101–104.

[18] J. Horkens and L.T. Romankiw, Pulsed Potentiostatic Deposition of Gold from

Solutions of the Au(I) Sulfite Complex, J. Electrochem. Soc. 124 (1977) 1499–1505.

[19] A. Ruffoni and D. Landolt, Pulse-Plating of Au–Cu–Cd alloys—II. Theoretical Modelling of Alloy Composition, Electrochim. Acta 33 (1988) 1281–1289.

[20] M.S. Chandrasekar and M. Pushpavanam, Pulse and Pulse Reverse Plating—Conceptual, Advantages and Applications, Electrochim. Acta 53 (2008) 3313–3322.

[21] M.D. Uchic, D.M. Dimiduk, J.N. Florando, and W.D. Nix, Sample Dimensions Influence Strength and Crystal Plasticity, Science 305 (2004) 986–989.

[22] J.R. Greer, W.C. Oliver, and W.D. Nix, Size Dependence of Mechanical Properties of Gold at the Micron Scale in the Absence of Strain Gradients, Acta Mater. 53 (2005) 1821–1830.

[23] M.D. Uchic, P.A. Shade, and D.M. Dimiduk, Plasticity of Micrometer-Scale Single Crystals in Compression, Annu. Rev. Mater. Res. 39 (2009) 361–386.

[24] T. Nagoshi, M. Mutoh, T.-F.M. Chang, T. Sato, M. Sone, Sample Size Effect of Electrodeposited Nickel with Sub-10nm Grain Size, Mater. Lett. 117 (2014) 256–259.

[25] M. Dietiker, S. Buzzi, G. Pigozzi, J.F. Löffler, and R. Spolenak, Deformation Behavior of Gold Nano-Pillars Prepared by Nanoimprinting and Focused Ion-Beam Milling, Acta Materialia 59 (2011) 2180–2192.

[26] R. Gu, A.H.W. Ngan, Size Effect on the Deformation Behavior of Duralumin Micropillars, Scripta Mater. 68 (2013) 861–864.

[27] L. Oniciu and L. Mureşan, Some Fundamental Aspects of Levelling and Brightening in Metal Electrodeposition, J. Appl. Electrochem. 21 (1991) 565–574.

[28] D. Udler and D.N. Seidman, Grain Boundary and Surface Energies of Fcc Metals, Phys. Rev. B 54 (1996) R11133–R11136.

[29] W.-H. Lin, C.-Y. Chen, T.-F.M. Chang, Y.-J. Hsu, and M. Sone, Effects of Pressure in Cathodic Deposition of TiO_2 and SnO_2 with Supercritical CO_2 Emulsified Electrolyte, Electrochim. Acta 208 (2016) 244–250.

[30] A. Rinaldi, P. Peralta, C. Friesen, and K. Sieradzki, Sample-Size Effects in the Yield Behavior of Nanocrystalline Nickel, Acta Mater. 56 (2008) 511–517.

[31] R. Fritz, V. Maier-Kiener, D. Lutz, and D. Kiener, Interplay Between Sample Size and Grain Size: Single Crystalline vs. Ultrafine-Grained Chromium Micropillars, Mater. Sci. Eng. A 674 (2016) 626–633.

[32] N. Warthi, P. Ghosh, A.H. Chokshi, Approaching Theoretical Strengths by Synergistic Internal and External Size Refinement, Scripta Mater. 68 (2013) 225–228.

[33] R. Schwaiger, B. Moser, M. Dao, N. Chollacoop, S. Suresh, Some Critical Experiments on the Strain-Rate Sensitivity of Nanocrystalline Nickel, Acta Mater. 51 (2003) 5159–5172.

[34] Q. Wei, Strain Rate Effects in the Ultrafine Grain and Nanocrystalline Regimes—Influence on Some Constitutive Responses, J. Mater. Sci. 42 (2007) 1709–1727.

[35] J.Y. Zhang, G. Liu, J. Sun, Strain Rate Effects on the Mechanical Response in Multi- and Single-Crystalline Cu Micropillars: Grain Boundary Effects, Int. J. Plast. 50 (2013) 1–17.

[36] C. Howard, D. Frazer, A. Lupinacci, S. Parker, R.Z. Valiev, C. Shin, B.W. Choi, and P. Hosemann, Investigation of Specimen Size Effects by In-Situ Microcompression of Equal Channel Angular Pressed Copper, Mater. Sci. Eng. A 649 (2016) 104–113.

2.6. Figures

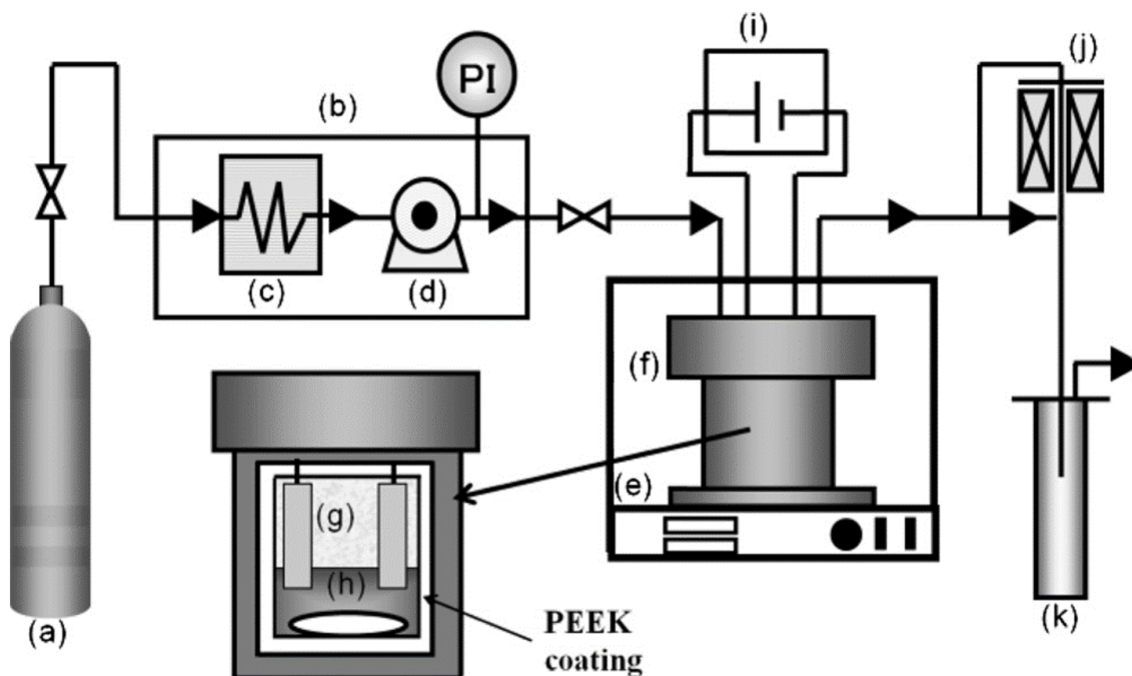

FIG. 2.1. A schematic of high pressure apparatus for EP-SCE: (a) CO_2 gas tank, (b) CO_2 pressurization unit, (c) liquidization unit, (d) high-pressure pump, (e) box oven, (f) reaction cell, with PEEK coating on the inner wall, (g) substrates, (h) stirrer, (i) programmable power supply, (j) back-pressure regulator, and (k) trap [9].

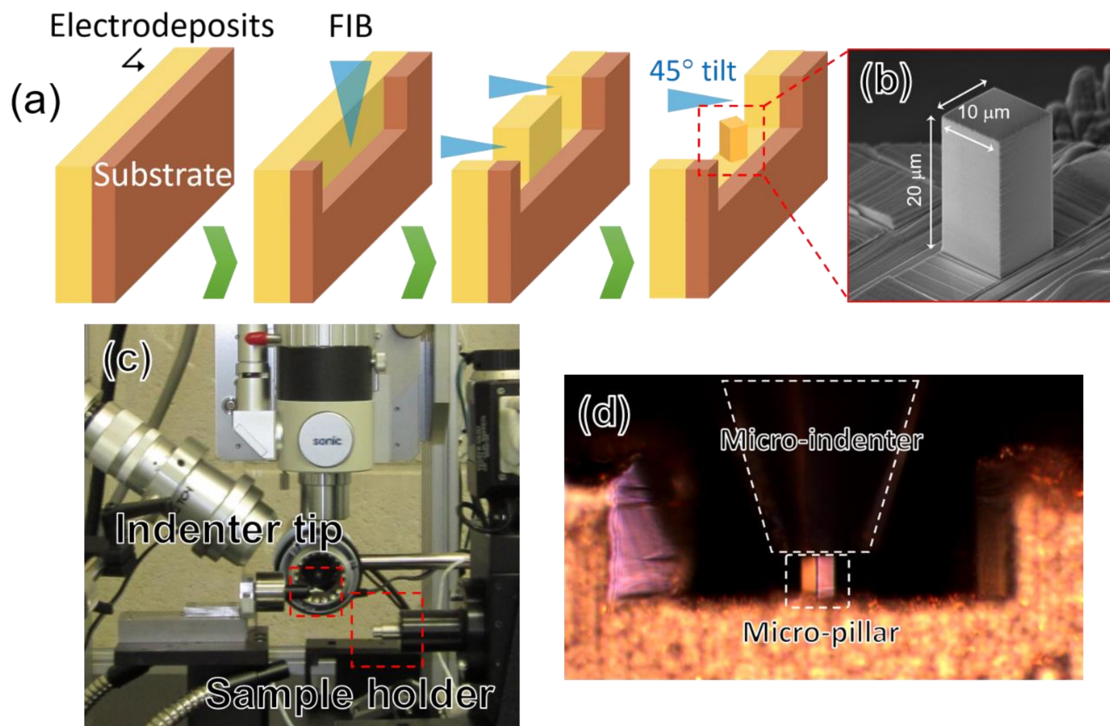

FIG. 2.2. (a) A schematic showing the fabrication process of micro-pillars using FIB. (b) SEM image of a micro-pillar with the dimension of 10×10×20 μm^3. (c) Micro-mechanical testing machine used for compression test. (d) Optical microscopic image showing the micro-indenter and micro-pillar.

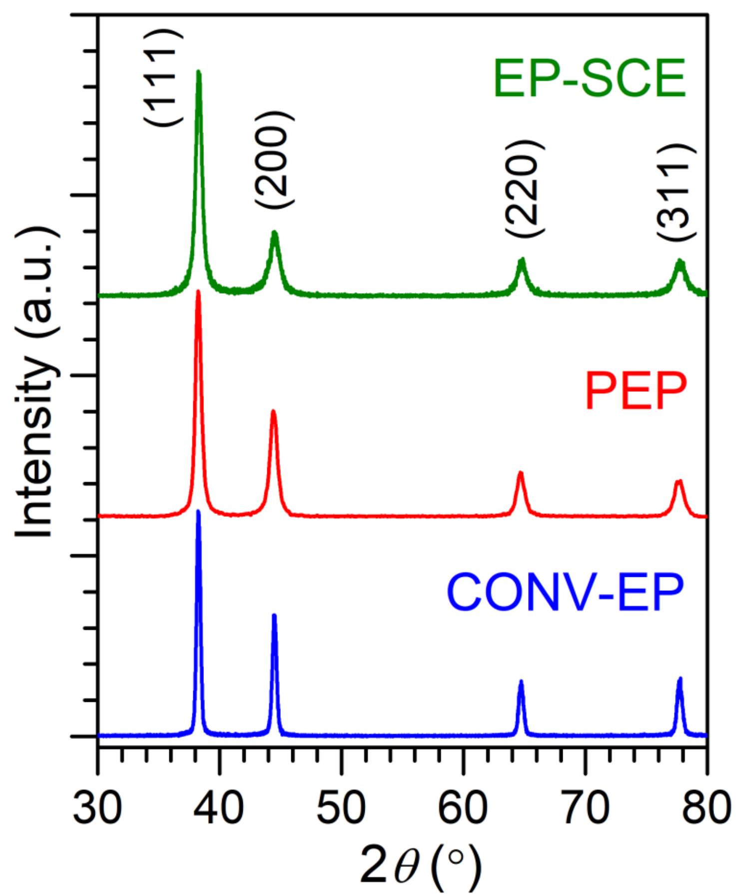

FIG. 2.3. GIXRD patterns of CONV-EP, PEP, and EP-SCE Au films.

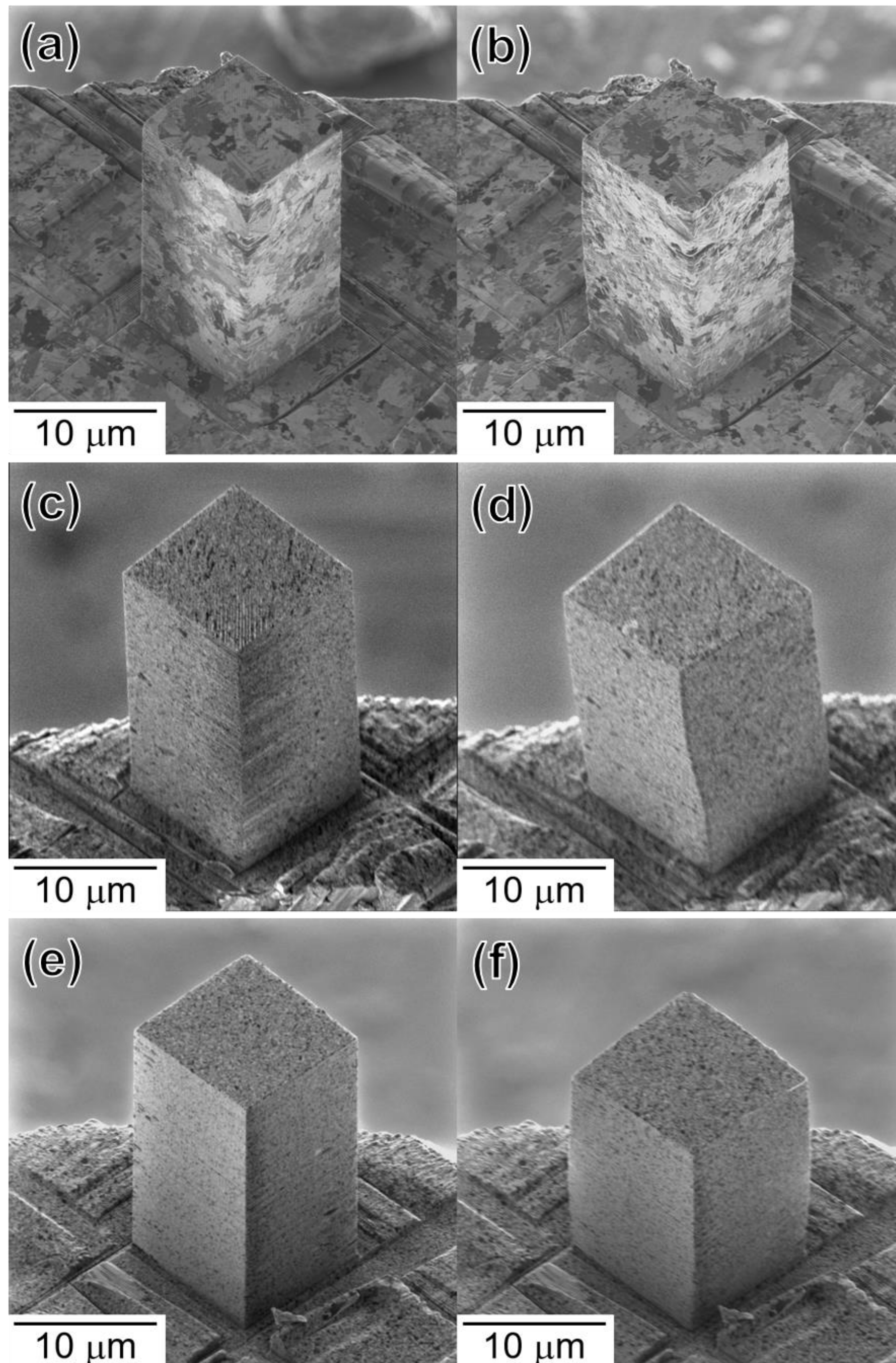

FIG. 2.4. SIM images showing the (a,b) CONV-EP (c,d) PEP, and (e,f) EP-SCE Au pillars (a,c,e) before and (b,d,f) after the compression tests. The micro-pillars were tilted at 45°.

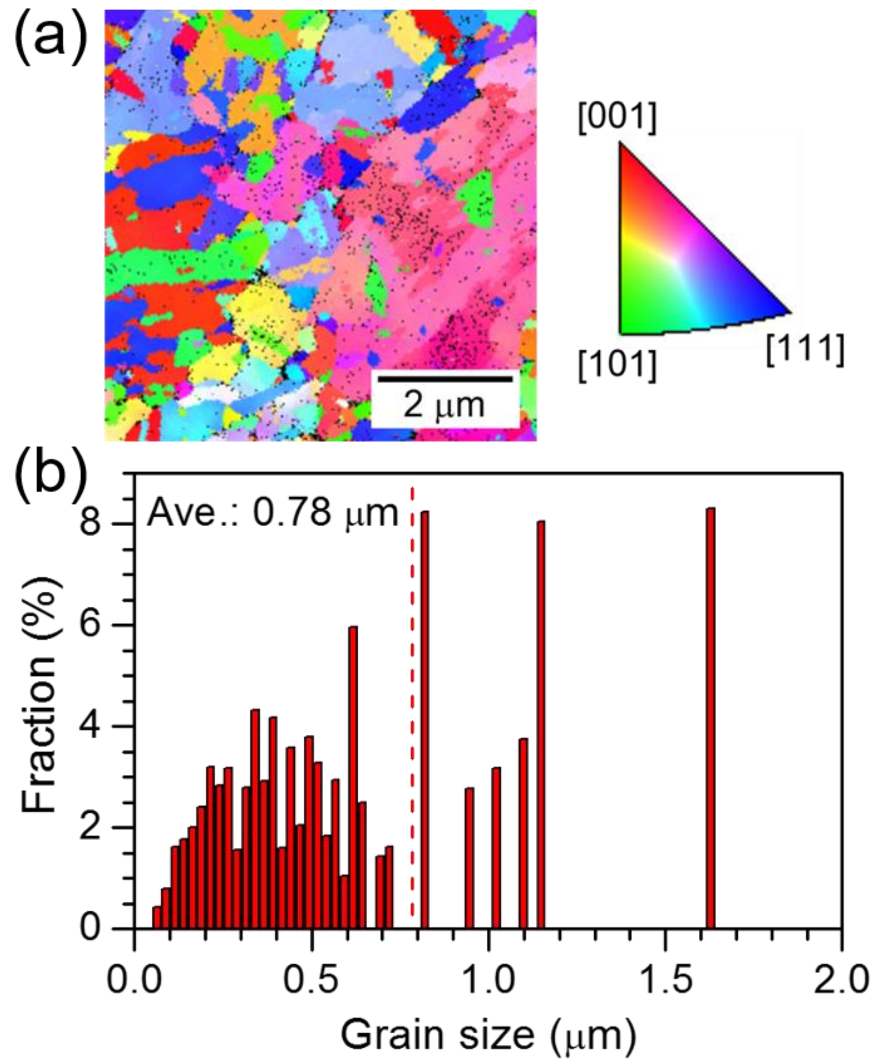

FIG. 2.5. (a) EBSD orientation map of the CONV-EP Au pillar in Fig. 2.4 (a,b) with the view of compression direction. (b) Grain size distribution obtained from (a).

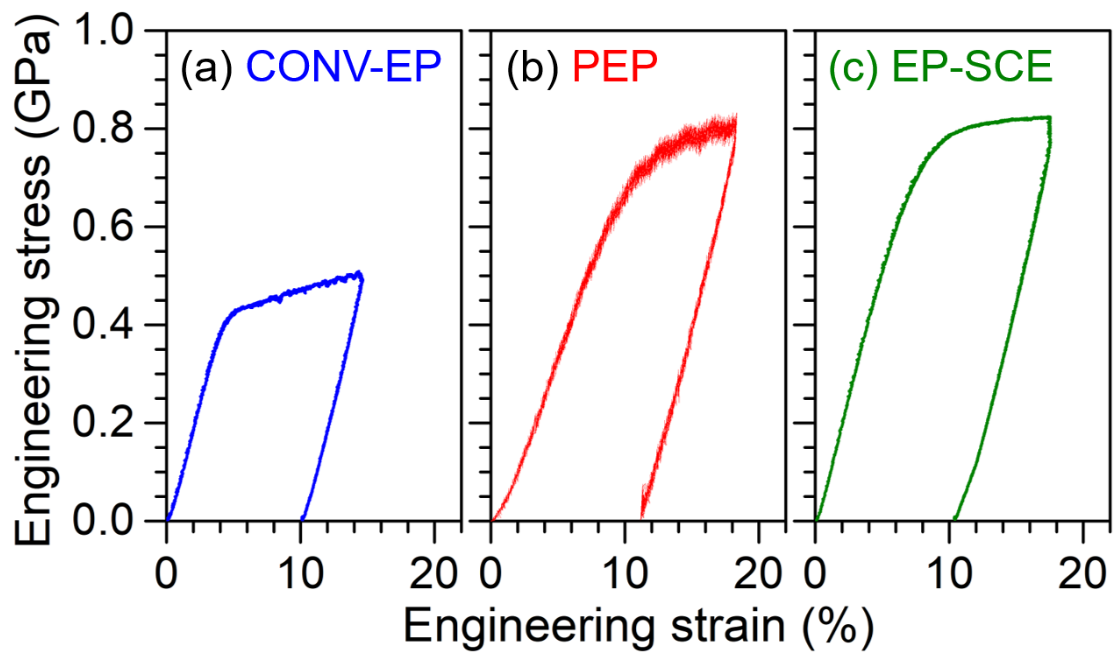

FIG. 2.6. Engineering *SS* curves obtained from the micro-compression tests using Au micro-pillars. Pillar dimensions: 10×10×20 μm^3. (a) CONV-EP, (b) PEP, and (c) EP-SCE Au thick films.

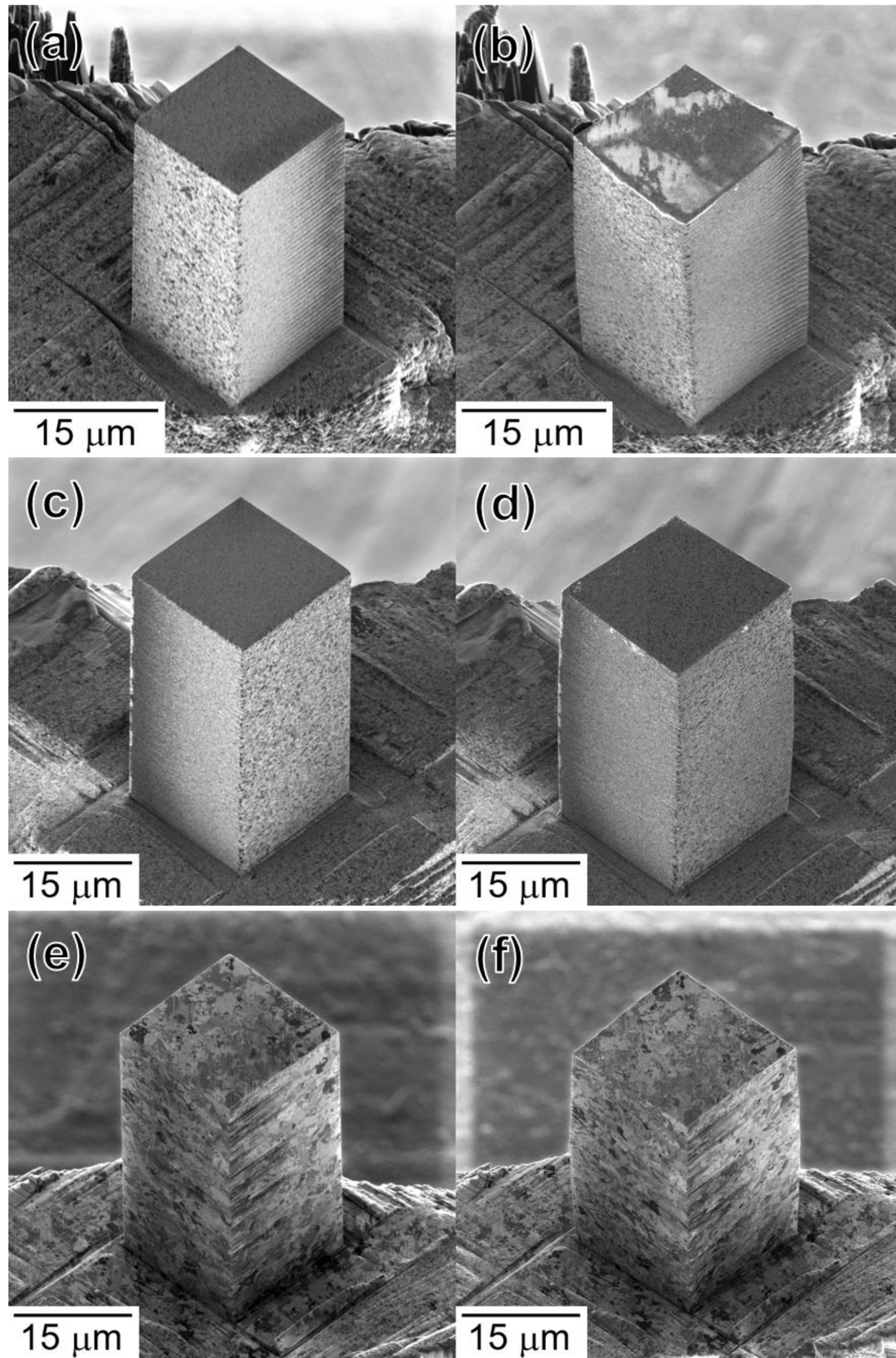

FIG. 2.7. SIM images of the EP-SCE Au pillars with the dimensions of (a,b) 15×15×30 μm^3 and (c,d) 20×20×40 μm^3. (e,f) The CONV-EP Au pillar with the dimensions of 20×20×40 μm^3. (a,c,e,) Before and (b,d,f) after micro-compression tests. The micro-pillars were tilted at 45°.

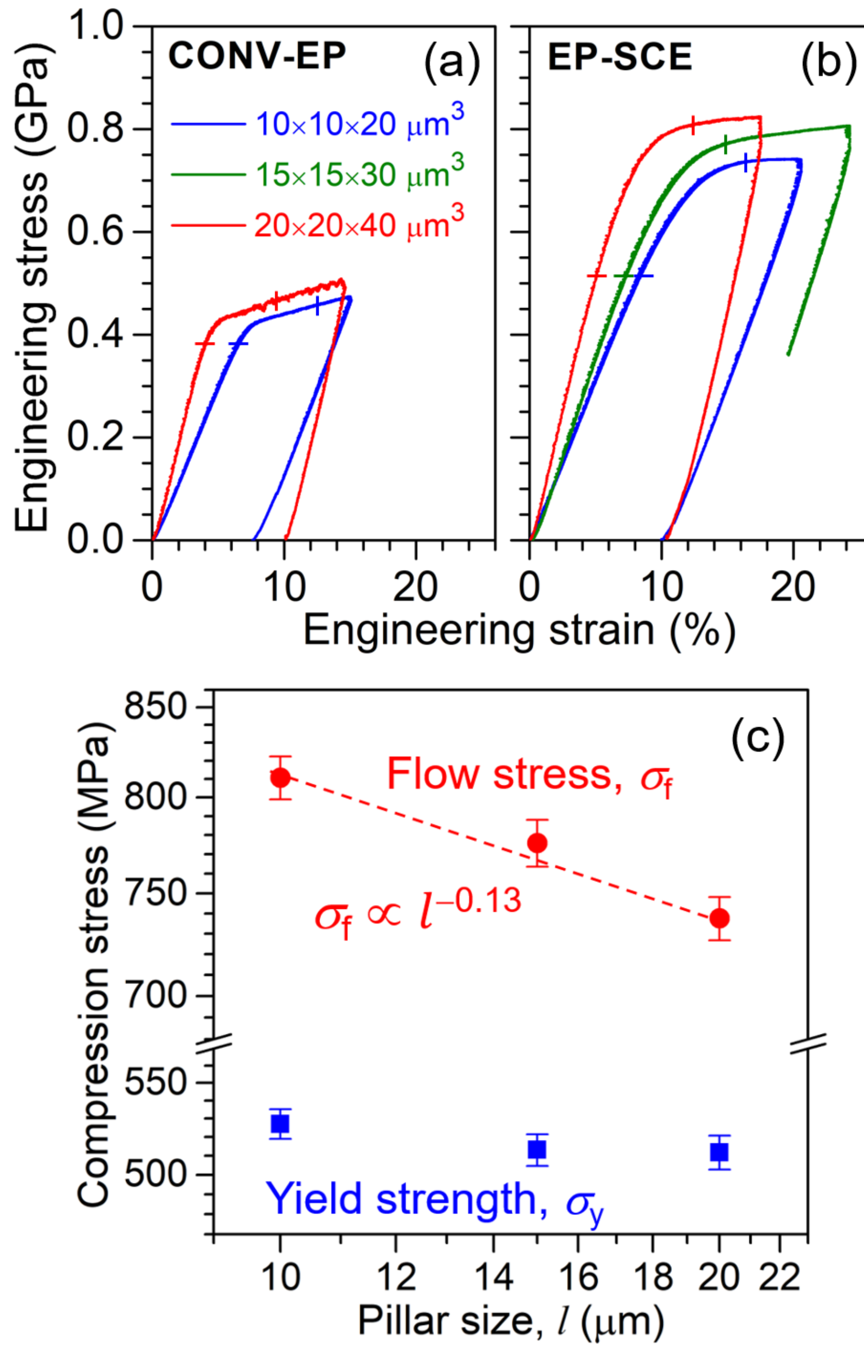

FIG. 2.8. Engineering stress-strain curves of (a) the CONV and (b) the EP-SCE Au micro-pillars with different dimensions. The yield strength (σ_y) and flow stress at 5% (σ_f) are marked by the vertical bar and horizontal bar, respectively. (c) Plot of the stress, σ_f and σ_y, versus the pillar size for the EP-SCE Au pillars.

CHAPTER 3

Galvanic Deposition of Au–Cu Alloys from Non-Cyanide Electrolyte

3.1. Introduction

In recent years, electroplating of metal-based electronic components applied in micro-electrical-mechanical system (MEMS) devices has been developed to replace conventional Si-based components to further improve the performance and miniaturization of the devices [1–4]. Among the metallic materials, Au is promising to attain better sensitivity in MEMS accelerometers by significantly lowering the Brownian noise because of the high density (19.30 g/cm^3 at 298 K) [5]. However, Au is known to be a soft metallic material. Reliability or structure stability of the components used in MEMS devices is highly dependent on mechanical properties (yield strength, fracture strength, etc.) of the materials used to construct the components. Especially for the yield stress, prior to the yield stress, the material will deform elastically and return to its original shape when the applied stress is removed. Yield stress of bulk Au is reported to be 55~200 MPa [6]. Although a yield stress of 500 MPa could be achieved by refining the average grain size to nanoscale through the pulse electroplating [7] and supercritical carbon dioxide-assisted electroplating methods [8], but it is still much lower than fracture strength of Si materials, which is 1–3 GPa [4]. Since Si material does not yield until fracture occurs hence the fracture strength is used here to be a comparison with the yield

stress of gold materials. Besides, abnormal grain growth of the pulse-electroplated fine-grained Au at room temperature may raise additional concerns in the applications [9]. To overcome these predicaments, alloying the electroplated Au is suggested to be the solution and allows further strengthening by the solid solution strengthening mechanism [10–12].

On the other hand, Vickers micro-hardness measurement is widely used to characterize mechanical properties of the electroplated metallic materials [13,14]. However, the obtained results are often affected by the substrate, which may not represent the real strength of the electroplated materials. Moreover, mechanical properties of materials in micro-scale are much different from those of bulk materials due to the size effect [15]. Therefore, micro-mechanical tests using specimens in micro-scale are required to provide reliable information on the mechanical properties for design of the MEMS micro-components [15,16].

In this chapter, effects of the current density on micro-mechanical properties of the Au–Cu alloy films fabricated by galvanostatic electroplating were evaluated by micro-compression tests. The Au–Cu alloy micro-specimen showed an ultra-high yield strength of 1.15 GPa when optimum electroplating conditions were employed. This report demonstrates electroplated Au–Cu alloys with high strength and excellent ductility are promising materials for next generation of MEMS.

3.2. Experimental

3.2.1. Fabrication of Au–Cu Alloys by Galvanostatic Plating

The Au–Cu electrolyte used in this work was a commercially available electrolyte provided by MATEX Co. Japan, which contained 17.3 g/L of $X_3Au(SO_3)_2$

(X=Na, K), 1.26 g/L of $CuSO_4$, and EDTA as the additive with pH of 7.5. A potentiostat (Solartron SI1287) was served for the electroplating. The electroplating was carried out at 50 °C, and the current density was varied from 2 to 9 mA/cm^2. A piece of Pt plate and Cu plate with the same dimensions of 1×2 cm^2 were used as the anode and the cathode, respectively. Two thicknesses of the films were prepared for the characterization. Thin films with a thickness of ~3 μm were used for surface characterization, and thick films with a thickness of ~50 μm were used only for fabrication of the micro-compression specimens.

3.2.2. Characterization

Surface morphology of the Au–Cu alloy thin films was observed by a scanning electron microscope (SEM, Hitachi SU4300SE). The composition was evaluated by energy dispersive spectroscopy (EDS) equipped in the SEM. Crystal structures of the films were characterized by X-ray diffraction (XRD, Rigaku Ultima IV) at a glancing angle of 3°. Microstructures and deformation behaviors of the micro-specimens were observed using a scanning ion microscope (SIM) equipped in a focus ion beam system (FIB, Hitachi FB2100).

3.2.3. Micro-Compression Tests

The micro-compression specimens used in this study were non-tapered micro-pillars fabricated from the Au–Cu alloy thick films using the FIB. The micro-pillars had a square cross-section of 10×10 μm^2 and a height of 20 μm. The micro-compression tests were conducted with a testing machine specially designed for micro-specimens. The compression was conducted at a constant displacement rate of 0.1 μm/s using a piezo-

electric actuator. Details of the micro-pillar fabrication procedures and the micro-compression test were reported in a previous work [16].

3.3. Results and Discussion

3.3.1. Surface Morphology of Au–Cu Films

Fig. 3.1 shows surface morphology of the Au–Cu alloy films electroplated at various current density. The films deposited at lower current densities exhibited nodular-like structures as shown in Fig. 3.1(a) and (b). When the current density was increased (4–7 mA/cm^2), the surface morphology gradually changed to a smooth surface as shown in Fig. 3.1(c) to (f). Large agglomerates of bump-clusters were observed when the current density was higher than 8 mA/cm^2, as shown in Fig. 3.1(g) to (h). Similar morphology was reported for the Au-based alloys electroplated at high current density [17].

3.3.2. Crystalline Structure and Composition

Fig. 3.2(a) and (b) show XRD patterns of the Au–Cu alloys and the peak shift in the vicinity of the major (111) peak and (200) peak, respectively. As shown in Fig. 3.2(b), both the (111) and (200) peaks shifted continuously to a higher diffraction angle as the current density increased. For instance, the (111) peak shifted from $2\theta = 38.79°$ at current density = 3 mA/cm^2 to $2\theta = 40.09°$ at current density = 8 mA/cm^2. The peak shift was suggested to be a result of the increase in the Cu content since 2θ of the (111) peak of Cu is larger than 2θ of the (111) peak of Au. No diffraction peaks from intermetallic nor other ordered phases were observed in the electroplated films. Relationships between the current density with average grain size of the Au–Cu alloy, Cu content in the Au–Cu alloy, and the lattice constant are summarized in Fig. 3.3. The d_g was estimated from the XRD

results and the Scherrer equation. The d_g was reduced from 8.8 nm to a minimum value of 5.3 nm when the current density was increased from 2 to 6 mA/cm^2. d_g of electroplated materials is highly dependent on the cathodic overpotential, which grain refinement is observed as the cathodic overpotential increased [18]. Based on the Butler–Volmer equation, the cathodic overpotential is related to the current density, which the cathodic overpotential increases as the current density increases. Therefore, it is expected to see a reduction in the d_g as the current density increases. On the other hand, an increased in the d_g was observed as the current density increased beyond 6 mA/cm^2. Increasing the current density also promotes the side reaction(s), such as hydrogen evolution. Cathodic overpotential of the main reactions, which are reduction of Au and Cu in this study, would be lowered when the side reaction(s) is promoted [19]. This should be the cause of the grain coarsening observed when the current density is higher than 6 mA/cm^2. Meanwhile, a sustained increase of the Cu concentration in the Au–Cu alloys from 12.2 at% to 46.7 at% was observed when the current density was increased from 2 to 9 mA/cm^2. The results can be interpreted by the difference in the reduction potential between Au and Cu [17], which the reduction potential of Cu is more negative than that of Au. An increase in the cathodic current density would make the applied potential to be more negative, hence reduction of Cu is gradually favored and leads to an increase in the Cu concentration. The lattice constant consequently decreased as the Cu concentration increased due to a smaller atomic radius of Cu atom as shown in Fig. 3.3(c).

3.3.3. Deformation Behavior of Au–Cu Micro-Pillars and Micro-Mechanical Properties

Fig. 3.4 shows SIM images of the Au–Cu alloy micro-pillars fabricated from the thick Au–Cu alloy films before and after the micro-compression tests. Barrel-shape

deformations were observed in the micro-pillars fabricated from the films electroplated at current density = 3, 5, and 6 mA/cm^2, which are typical deformations for polycrystalline metallic materials [20,21]. When the current density was further increased to 8 mA/cm^2, brittle fracture shown by the cracks along boundaries of the agglomerates were observed after the compression test. The Au–Cu alloy film electroplated at 8 mA/cm^2 was composed of nano-grains, which was similar to the film electroplated at lower current density of 4 mA/cm^2; however, formation of the bump-clustered agglomerates at high current density might be the main cause of the brittle deformation. Au–Cu alloys are known to be highly ductile materials. To the best of our knowledge, this is the first report on brittle fracture of Au–Cu alloys, and this information is essential for design of components used in MEMS devices.

Engineering strain-stress (*SS*) curves obtained from the micro-compression tests are shown in Fig. 3.5. Generally, all the pillars exhibited extremely high yield strength (σ_y, determined by the cross-point of the *SS* curve and 0.2% offset line of the elastic deformation region) ranged at 1.00–1.15 GPa, which are far larger than the yield strength obtained from micro-mechanical tests of pure Au and pure Cu reported in the literature [7,8,22,23]. Flow stresses (σ_f) at 10 % strain of all the micro-pillars were higher than 1.3 GPa except for the micro-pillar prepared from the film electroplated at current density of 8 mA/cm^2, which the crack-induced brittle fracture should be the reason of the lowered flow stress.

3.3.4. Strengthening Mechanisms in the Electroplated Au–Cu Alloys

The enhanced yield strength in the Au–Cu alloys is mainly attributed by the following two mechanisms: (i) Grain boundary strengthening [24] and (ii) solid solution

strengthening [10]. As shown in Fig. 3.3, the grain refinement effect goes along with an increase in the Cu content as the current density increases. According to the grain boundary strengthening mechanism, the strength of metallic materials increases as total amount of grain boundary in a specimen increases, that is also understood as a decrease in the average grain size. Moreover, the solid solution strengthening mechanism is considered to restrict the dislocation movement due to interaction of the dislocations with the strained lattice surrounding the solute atoms, which then leads to a stacked strengthening beyond the grain boundary strengthening mechanism. In Fig. 3.6(a), the grain boundary strengthening mechanism can be summarized as the Hall–Petch plots (σ_y vs. $d_g^{-0.5}$) using results obtained in this study and the literature [17,25,26]. Due to lack of the literature on the yield stress of Au–Cu alloys, results obtained from Vicker micro-hardness (HV) tests were adopted and converted to the yield stress by dividing the micro-hardness value to a Tabor coefficient of 4 (σ_y = HV/4 [27]) for the comparison. Overall, the values reported in the literature all follow the Hall–Petch relationship. However, softening caused by the inverse Hall–Petch effect occurs when the d_g scales down to ~6 nm [17,25]. The results obtained in this work also follow the Hall–Petch relationship well. However, the yield stress continues increasing in the inverse Hall–Petch region and reaches 1.15 GPa at the finest d_g = 5.3 nm. Most importantly, the results obtained in this study are much more reliable than those of Vicker micro-hardness tests since the hardness results are often affected by the substrate and cannot reflect real strength of the electroplated films. Furthermore, a plot of log-scale of the Cu content versus the σ_y is shown in Fig. 3.6(b). The σ_y was increased as the Cu content increased, which was a result of the solid solution strengthening mechanism. On the other hand, the σ_y became independent of the Cu content when the Cu content was larger than ~36 at%. These results

suggest the grain size is the dominant factor for the strengthening observed in the Au–Cu alloys [17,25,26].

3.4. Conclusions

In this work, Au–Cu alloys were fabricated by galvanostatic electroplating, and the micro-mechanical properties were evaluated by micro-compression tests. Surface morphology of the Au–Cu alloy films showed a wide variation from smooth surface to bump-clustered agglomerates as the current density varied from 2 to 9 mA/cm^2. A reduction in the grain size and an increase in the Cu content were observed with an increase in the current density. The film with the finest d_g at 5.3 nm was obtained when current density = 6 mA/cm^2 was used. For the micro-compression tests, the specimens used were micro-pillars with dimensions of 10×10×20 μm^3 fabricated from the electroplated Au–Cu alloys. The highest yield stress at 1.15 GPa was achieved for the Au–Cu alloy having d_g = 5.3 nm and the Cu content of 30.3 at%. The ultra-high yield stress was higher than the values reported in the literatures and suggested to be a synergistic effect of the grain boundary strengthening mechanism with the solid solution strengthening mechanism. In conclusion, Au–Cu alloys fabricated by electroplating process high yield stress and tunable Cu concentration, which fulfill the requirement to replace the Si-based materials in next generation MEMS devices.

3.5 References

[1] R. GhodssiReza, P. Lin, MEMS Materials and Processes Handbook, first ed., Springer, New York (2011).

[2] T. Fritz, M. Griepentrog, W. Mokwa, and U. Schnakenberg, Determination of Young's Modulus of Electroplated Nickel, Electrochim. Acta 48 (2003) 3029–3035.

[3] J. Schroers, T. Nguyen, S. O'Keeffe, and A. Desai, Thermoplastic Forming of Bulk Metallic Glass—Applications for MEMS and Microstructure Fabrication, Mater. Sci. Eng. A 449–451 (2007) 898–902.

[4] T. Tsuchiya, O. Tabata, J. Sakata, and Y. Taga, Specimen Size Effect on Tensile Strength of Surface-Micromachined Polycrystalline Silicon Thin Films, J. Microelectromech. Syst. 7 (1998) 106–113.

[5] D. Yamane, T. Konishi, T. Matsushima, K. Machida, H. Toshiyoshi, and K. Masu, Design of Sub-1g Microelectromechanical Systems Accelerometers, Appl. Phys. Lett. 104 (2014) 074102.

[6] H.D. Espinosa, B.C. Prorok, and B. Peng, Plasticity Size Effects in Free-Standing Submicron Polycrystalline FCC Films Subjected to Pure Tension, J. Mech. Phys. Solids 52 (2004) 667–689.

[7] C.-Y. Chen, M. Yoshiba, T. Nagoshi, T.-F.M. Chang, D. Yamane, K. Machida, K. Masu, and M. Sone, Pulse Electroplating of Ultra-Fine Grained Au Films with High Compressive Strength, Electrochem. Commun. 67 (2016) 51–54.

[8] H. Tang, C.-Y. Chen, T. Nagoshi, T.-F.M. Chang, D. Yamane, K. Machida, K. Masu, and M. Sone, Enhancement of Mechanical Strength in Au Films Electroplated with Supercritical Carbon Dioxide, Electrochem. Commun. 72 (2016) 126–130.

[9] N. Schell, T. Jensen, J. H. Petersen, K. P. Andreasen, J. Bøttiger, and J. Chevallier,

The Nanostructure Evolution During and After Magnetron Deposition of Au Films, Thin Solid Films 441 (2003) 96–103.

[10] R.L. Fleischer, Substitutional Solution Hardening, Acta Mater. 11 (1963) 203–209.

[11] T. Yokoshima, A. Takanaka, T. Hachisu, A. Sugiyama, Y. Okinaka, and T. Osaka, Mechanical and Electrical Properties of Au-Ni-C Alloy Films Produced by Pulsed Current Electrodeposition, J. Electrochem. Soc. 160 (2013) D513–D518.

[12] Y.M. Wang, A.F. Jankowski, and A.V. Hamza, Strength and Thermal Stability of Nanocrystalline Gold Alloys, Scripta Mater. 57 (2007) 301–304.

[13] J.R. Cahoon, W.H. Broughton, and A.R. Kutzak, The Determination of Yield Strength from Hardness Measurements, Metall. Trans. 2 (1971) 1979–1983.

[14] C.A. Schuh, T.G. Nieh, and H. Iwasaki, The Effect of Solid Solution W Additions on the Mechanical Properties of Nanocrystalline Ni, Acta Mater. 51 (2003) 431–443.

[15] J.R. Greer and J.Th.M. De Hosson, Plasticity in Small-Sized Metallic Systems: Intrinsic Versus Extrinsic Size Effect, Prog. Mater. Sci. 56 (2011) 654–724.

[16] T. Nagoshi, T.-F.M. Chang, S. Tatsuo, and M. Sone, Mechanical Properties of Nickel Fabricated by Electroplating with Supercritical CO_2 Emulsion Evaluated by Micro-Compression Test Using Non-Tapered Micro-Sized Pillar, Microelectron. Eng. 110 (2013) 270–273.

[17] E. Brun, F. Durut, R. Botrel, M. Theobald, O. Legaie, I. Popa, and V. Vignal, Influence of the Electrochemical Parameters on the Properties of Electroplated Au-Cu Alloys, J. Electrochem. Soc. 158 (2011) D223–D227.

[18] E. Budevski, G. Staikov, and W.J. Lorenz, Electrocrystallization: Nucleation and Growth Phenomena, Electrochim. Acta 45 (2000) 2559–2574.

[19] D.R. Gabe, The Role of Hydrogen in Metal Electrodeposition Processes, J. Appl.

Electrochem. 27 (1997) 908–915.

[20] T. Nagoshi, M. Mutoh, T.-F.M. Chang, T. Sato, M. Sone, Sample Size Effect of Electrodeposited Nickel with Sub-10nm Grain Size, Mater. Lett. 117 (2014) 256–259.

[21] J.Y. Zhang, J.C. Cui, G. Liu, and J. Sun, Deformation Crossover in Nanocrystalline Zr Micropillars: The Strongest External Size, Scripta Mater. 68 (2013) 639–642.

[22] M.A. Meyers, A. Mishra, and D.J. Benson, Mechanical Properties of Nanocrystalline Materials, Prog. Mater. Sci. 51 (2006) 427–556.

[23] M. Mutoh, T. Nagoshi, T.-F.M. Chang, T. Sato, and M. Sone, Micro-Compression Test Using Non-Tapered Micro-Pillar of Electrodeposited Cu, Microelectron. Eng. 111 (2013) 118–121.

[24] N.J. Petch, The Cleavage Strength of Polycrystals, J. Iron Steel Inst., 174 (1953) 25-28.

[25] A.F. Jankowski, C.K. Saw, and J.P. Hayes, Nanocrystalline Growth and Grain-Size Effects in Au–Cu Electrodeposits, Thin Solid Films 515 (2006) 1152–1156.

[26] J. Lohmiller, N.C. Woo, and R. Spolenak, Microstructure–Property Relationship in Highly Ductile Au–Cu Thin Films for Flexible Electronics, Mater. Sci. Eng. A 527 (2010) 7731–7740.

[27] D. Tabor, The Hardness of Metals, Oxford Univ. Press, London (1951).

3.6. Figures

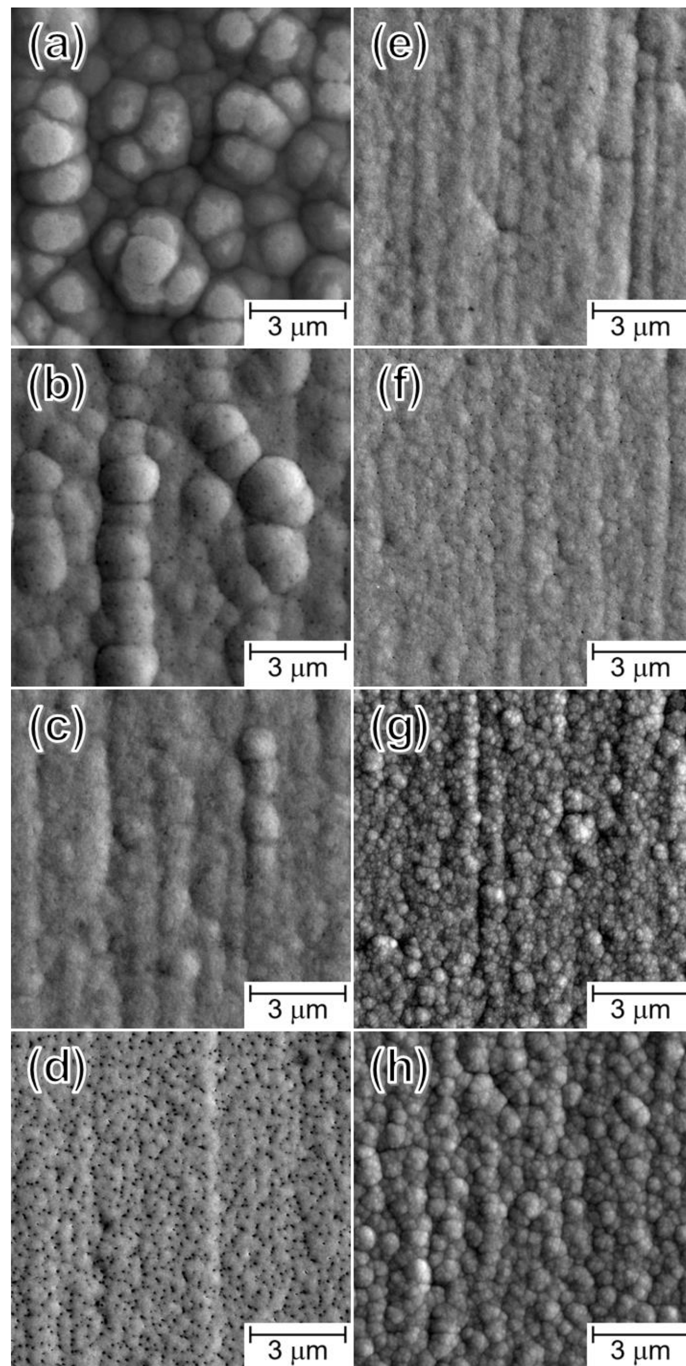

FIG. 3.1. SEM micrographs of the Au–Cu alloy films electroplated at current density = (a) 2, (b) 3, (c) 4, (d) 5, (e) 6, (f) 7, (g) 8, and (h) 9 mA/cm^2.

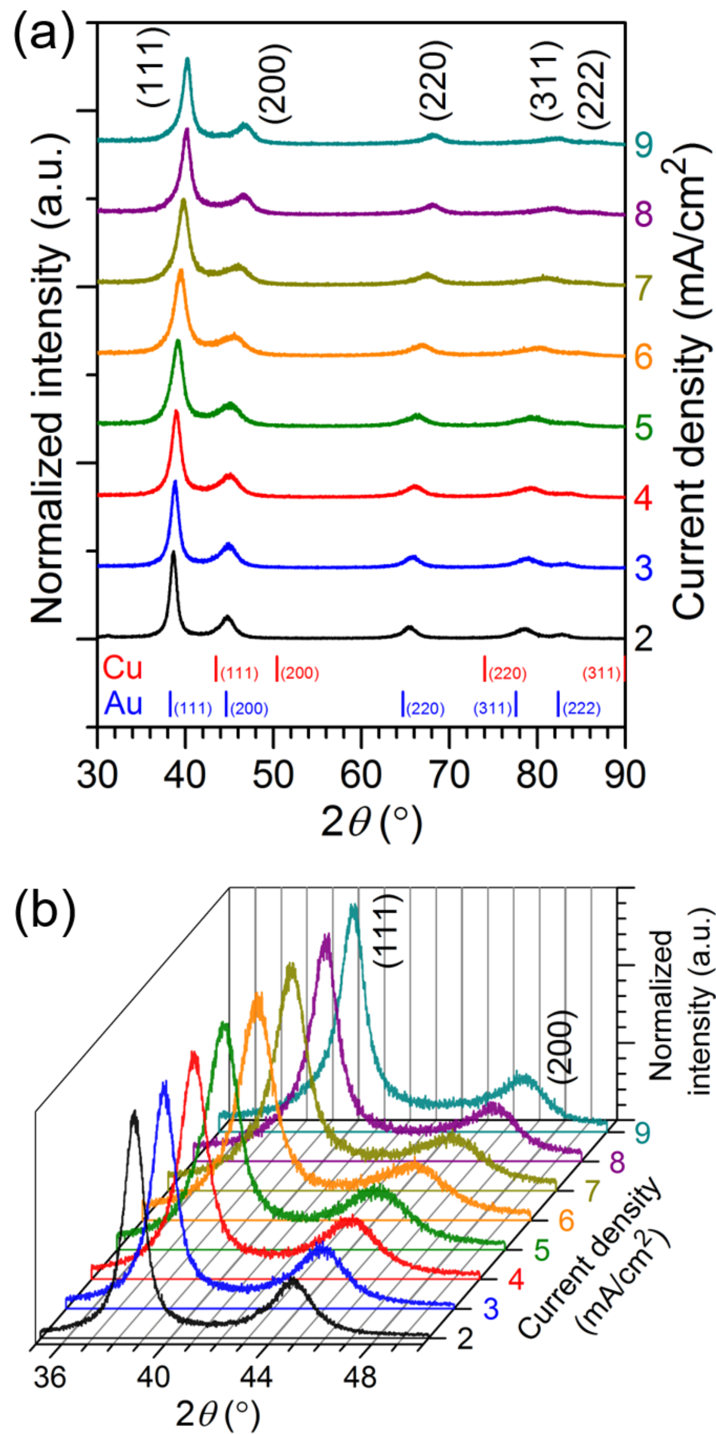

FIG. 3.2. (a) XRD patterns of the electroplated Au–Cu alloy films, where (b) the major diffraction peaks shifts of (111) and (200) were shown.

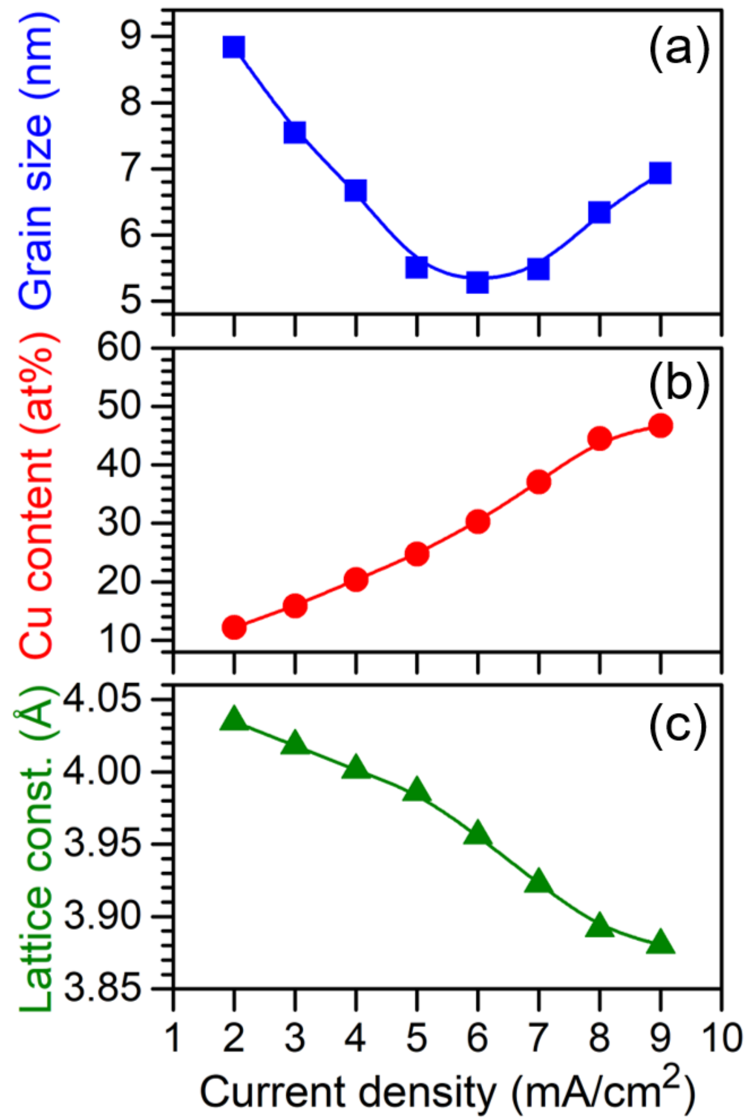

FIG. 3.3. Plot of the current density versus the grain size, the Cu content, and the lattice constant.

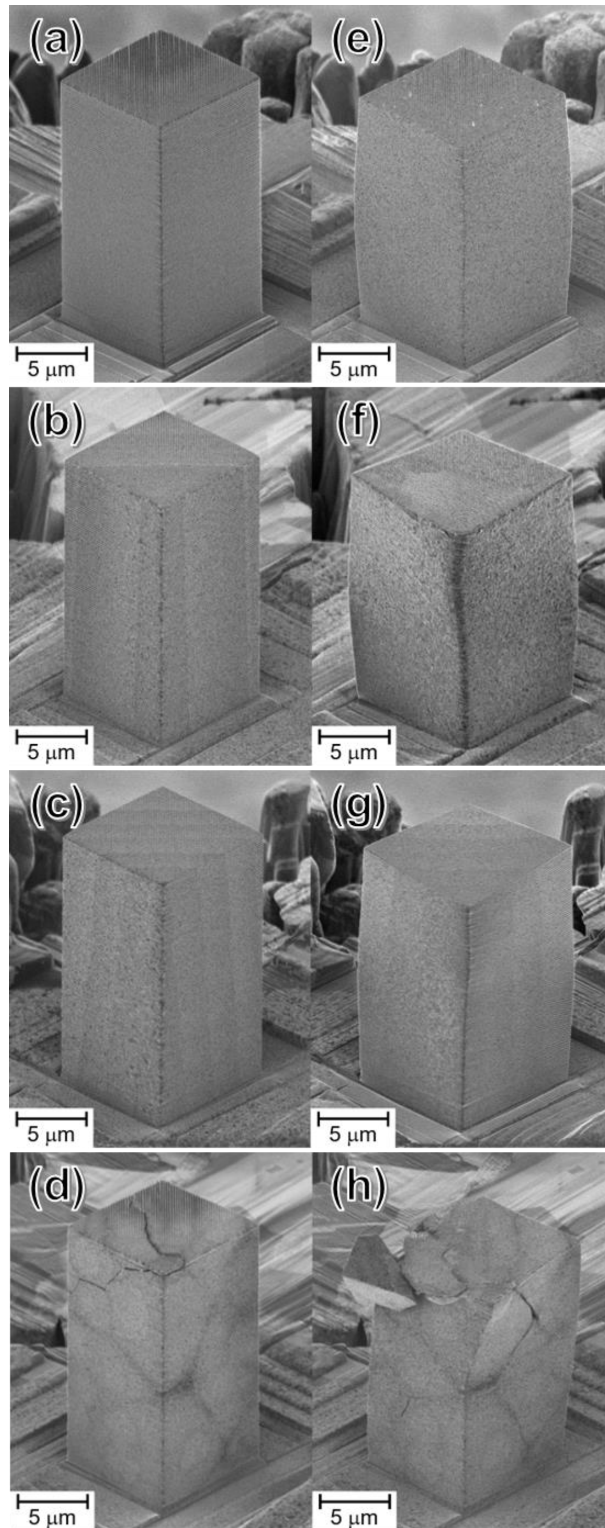

FIG. 3.4. SIM images of the Au-Cu alloy micro-pillars (a–d) before and (e–h) after the micro-compression tests. The micro-pillars were fabricated from the films electroplated at current density = (a, e) 3, (b, f) 5, (c, g) 6, and (d, h) 8 mA/cm^2.

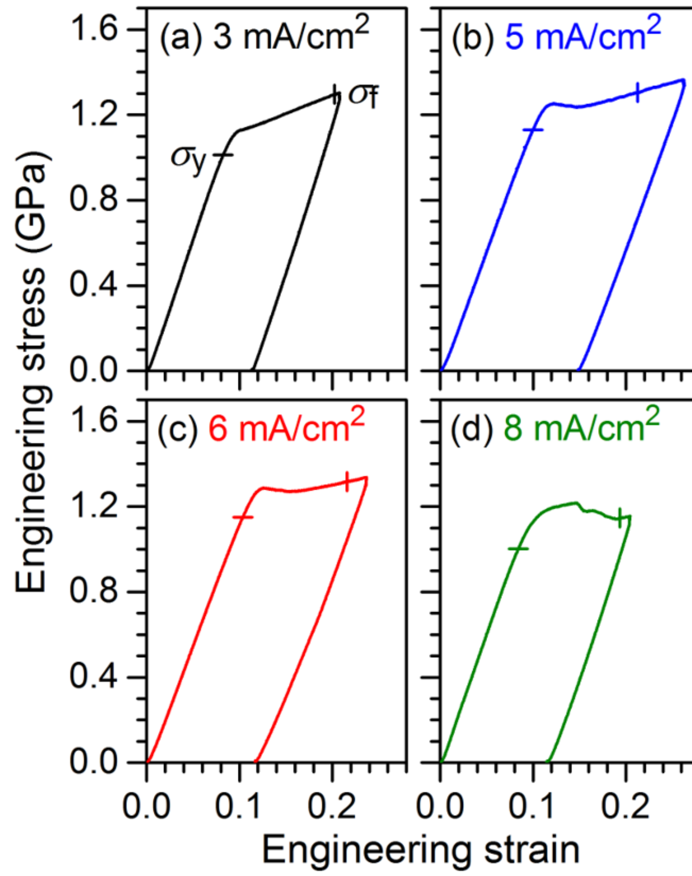

FIG. 3.5. Engineering *SS* curves of the micro-pillars fabricated from the films electroplated at current density = 3, 5, 6, and 8 mA/cm^2. The yield strength (σ_y) and the flow stress (σ_f) in each curves are marked by a horizontal bar (—) and a vertical bar (|), respectively.

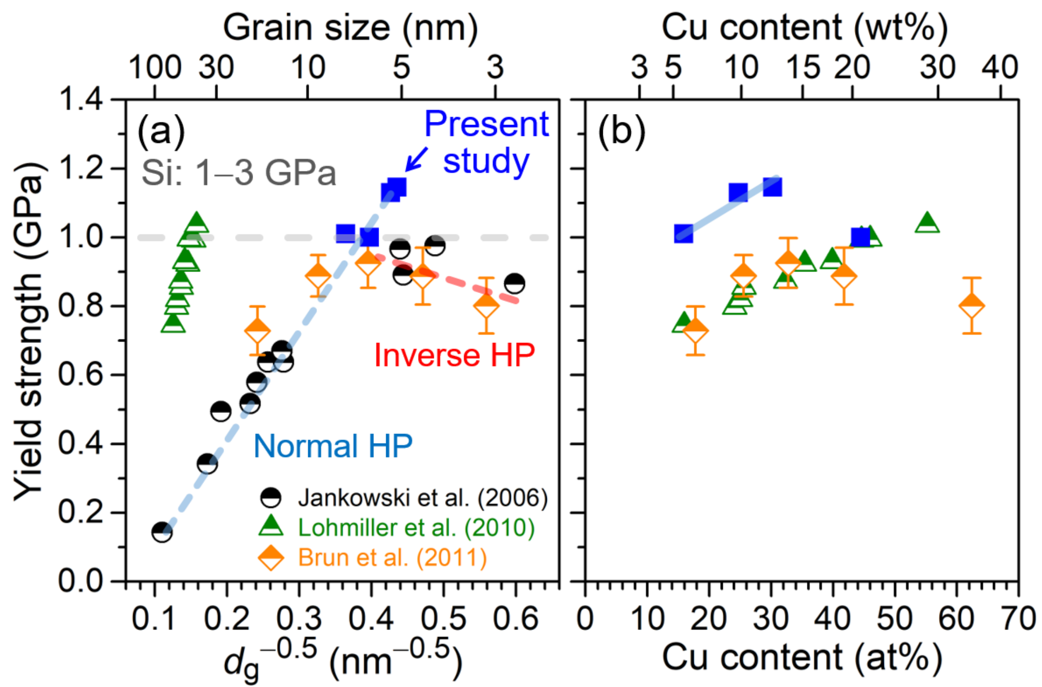

FIG. 3.6. Plots of (a) inverse-square root of the grain size versus the σ_y (Hall–Petch plot) and (b) Cu content versus the σ_y.

CHAPTER 4

Pulse Current Electrodeposition of Ultrahigh Strength Nanocrystalline Au–Cu Alloys

4.1. Introduction

In recent years, high density metallic materials have attracted much attention for applications as movable micro-components in micro-electro-mechanical systems (MEMS) devices to allow further enhancement in the sensitivity and miniaturization [1]. Au material is a promising candidate in MEMS devices due to its high density, chemical stability, electrical conductivity, and ductility [2]. However, mechanical strengths of pure Au are relative low when compared with metals commonly used in electronic devices, which the yield strength (σ_y) is reported to be 50–200 MPa in its bulk state [3]. Because of the poor mechanical property, concerns are raised on structure stability of movable micro-components composed of gold. Therefore, strengthening of the Au material becomes an urgent priority for applications in micro-electronic devices.

Electrodeposition is a commonly applied method to fabricate metallic materials for electronic devices [1,4]. When applied in fabrication of Au materials, Au with controlled properties, such as grain size and morphology can be achieved by adjusting the electrodeposition parameters. Especially for the feasibility in control of the grain size, the grain boundary strengthening mechanism (or so called Hall-Petch effect) can be utilized to enhance the mechanical property by refining the grain size into nanoscale [5,6]. A

significant enhancement in the σ_y over 500 MPa was reported in electrodeposition of pure Au with the grain size at ca. 10 nm [7,8]. In addition, electrodeposition can produce not only pure metals but also alloys with controlled composition. Alloy electrodeposition allows a further enhancement in the mechanical strength based on the solid solution strengthening mechanism [9,10]. In addition, the solid solution strengthening mechanism can be promoted by alloying elements having a large difference between the atomic masses [11,12].

Compared to direct constant current (DC) electrodeposition, pulse current (PC) electrodeposition allows a higher versatility in controlling properties of the electrodeposits [13–15]. In particular, PC electrodeposition can produce electrodeposits with a finer grain size than that of DC electrodeposition [16,17], which is beneficial in strengthening of Au materials. For the candidate of alloying elements, we limit the target to Cu because Cu is also a commonly used material in electronic devices, and its conductivity is comparable with Au. Besides, a conspicuous strengthening is expected based on the difference between the atomic masses [18–20].

For applications of the electrodeposited Au–Cu alloys in movable micro-components of electronic devices, mechanical properties of the Au–Cu alloys in micro-scale were evaluated. Although Vickers micro-hardness tests are often used to characterize micro-mechanical properties of electrodeposits, however, the obtained results could still be affected by the substrate [21,22]. Micro-mechanical tests using specimens in micro-scale are recognized as the most reliable method to evaluate micro-mechanical properties of electrodeposits [23,24]. The aim of this study is to evaluate influences of the PC electrodeposition parameters on chemical composition, grain size, surface morphology, and micro-mechanical properties of the Au–Cu alloys for design of

micro-components in next generation micro-electronic devices.

4.2. Experimental

4.2.1. Fabrication of Au–Cu Alloys by Pulse Electroplating

The Au–Cu alloys were electrodeposited onto cold-rolled Cu substrates ($10 \times 20 \times 0.3$ mm^3) with a commercially available electrolyte provide by MATEX Co. Japan. The electrolyte was consisted of 17.3 g/L of $X_3Au(SO_3)_2$ (X = Na, K), 1.26 g/L of $CuSO_4$, and EDTA as an additive with pH of 7.5. A piece of Pt substrate was used as the counter electrode, and the dimension was the same as the Cu substrate. Temperature of the electrolyte was maintained at 50 ± 1 °C using a water bath. The PC electrodeposition was carried out using a pulse power supply (plating electronic GmbH, type pe86CB-20-5-25-S/GD). For all experiments, the current on-time (t_{on}) was fixed at 10 ms, while the pulsed current density (J_p) and the current off-time (t_{off}) were varied. The parameters were summarized in Table 4.1. Thin Au–Cu alloy films with a thickness of 3–5 μm were used for characterization of the composition, grain size, and morphology. Thick films (thickness > 40 μm) were prepared for fabrication of the micro-compression specimens.

4.2.2. Characterization and Micro-Compression Tests

Crystal structures of the electrodeposited Au–Cu alloys were characterized by X-ray diffraction (XRD, Rigaku Ultima IV) at a glancing angle of 3°. The scan ranged from 2θ = 30° to 90° with a step size of 0.02°, and the scan rate was 2 °/min. The grain sizes were estimated from the XRD results and the Scherrer equation. Surface morphology and composition of the electrodeposits were evaluated by a scanning electron microscope (SEM, Hitachi SU4300SE) and energy dispersive spectroscopy (EDS)

equipped in the SEM. Micro-mechanical properties of the Au–Cu alloys were evaluated using micro-pillars fabricated from the thick Au–Cu films by focus ion beam (FIB, Hitachi FB2100). The Au–Cu micro-pillars had a square cross-section of 10×10 μm^2 and a height of 20 μm. Uniaxial compression tests were conducted at a constant displacement rate of 0.1 μm/s using a testing machine specially designed for micro-specimens. Details of the micro-pillar fabrication and the micro-compression tests are reported in a previous study [24]. Deformation behaviors of the Au–Cu micro-pillars after the micro-compression tests were observed by a scanning ion microscope (SIM) equipped in the FIB.

4.3. Results and Discussion

4.3.1. Effects of Pulse Current Density

Fig. 4.1 shows XRD patterns of the Au–Cu alloys electrodeposited at the J_p of 5–20 mA/cm^2 with the t_{on} and t_{off} both fixed at 10 ms. All electrodeposits showed the same crystal structure, which all of peaks could be indexed to the face-centered cubic (fcc) reflection. With an increase in the J_p, the peaks shifted to larger Bragg angles due to the lattice shrinkage caused by the increase in the Cu concentration. Effects of the J_p on the Cu concentration and grain size are plotted in Fig. 4.2. The Cu concentration linearly increased from 15.3 at% to 45.5 at% as the J_p increased from 5 to 20 mA/cm^2. These results are similar to the Au–Cu alloys prepared by the DC electrodeposition [20], which an increase in the J_p leads to a higher Cu concentration. The standard reduction potential of Cu is more negative than that of Au [25]. An increase in the J_p would make the applied potential to be more negative; therefore, the reduction of Cu is gradually favored and leads to an increase in the Cu concentration. In the meanwhile, the grain size decreased

from 8.0 nm to a minimum value of 5.2 nm as the J_p increased from 5 to 10 mA/cm^2, which is attributed to the increase of the nucleation rate as the current density increases [26]. On the other hand, after reaching the minimum value, the grain size increased to 5.8 nm as the the J_p increased to 20 mA/cm^2. The grain growth at high J_p could be attributed to promotion of side reactions (i.e., hydrogen evolution) as the applied potential becomes more negative, which then lowers overpotential of the main reaction(s) (reductions of Au and Cu in this case). The grain size of electrodeposits is highly dependent on the overpotential, and the grain size increases when the overpotential is lowered [26].

4.3.2. Effects of Current Off-Time

Effects of the t_{off} on crystal structure and alloy composition of the Au–Cu alloys are discussed in this section. Fig. 4.3 shows XRD patterns of the Au–Cu alloys electrodeposited at the J_p of 20 mA/cm^2 and the t_{off} varied from 20 to 120 ms. Similar to Fig. 4.1, all the XRD patterns showed the fcc reflections, and no other diffraction peaks were observed. The major (111) peak gradually shifted from $2\theta = 40.2°$ to 38.8° when the t_{off} increased from 20 to 120 ms, which indicate a decrease in the Cu concentration. It is known that the t_{off} plays an important role in controlling the alloy composition due to the galvanic displacement reaction occurred on the substrate surface [17,27–29]. During of the off-time period, nobler metals continue to be deposited on the substrate surface and less noble metals on the substrate surface would be oxidized and dissolved away. The displacement reaction leads to a decrease in concentration of the less noble component in the alloy. In the present Au–Cu system, the standard reaction potential of Au is more positive than Cu, hence nobleness of Au is higher. Therefore, the displacement reaction

occurred during the off-time period would cause a decrease in Cu concentration of the Au–Cu alloy, which is consistent with the lattice swelling observed from the XRD results.

Dependence of the Cu concentration on the t_{off} at J_p varied from 10 to 60 mA/cm^2 is shown in Fig. 4.4(a). Several trends were observed as the J_p and the t_{off} changed. At first, a decreases in the Cu concentration was observed as the t_{off} increased at all of the J_p. The results corresponded well with those observed from the XRD patterns, which more Cu was replaced by Au as the t_{off} increased. Secondly, decreasing rate of the Cu concentration as the t_{off} increased showed a transition from high to low as indicated by the change in slope of the curves in Fig. 4.4(a). The J_p of 50 mA/cm^2 curve indicated this point clearly. Cu concentration of the Au–Cu alloy showed a steep decrease from a short t_{off} to t_{off} of 240 ms, and the slop became less steep at t_{off} longer than 240 ms. The slope is suggested to be related to the displacement reaction or dissolution rate of Cu component in the Au–Cu alloy, which a steep slope indicates a high Cu dissolution rate. Again, the result is expected since the Cu dissolution rate is directly related to concentration of Cu component at surface of the film, and the Cu concentration is higher at the moment when the electrodeposition just entered the off-time period. Then the Cu concentration gradually decreases and leads to a lower Cu dissolution rate. Thirdly, the Cu concentration decreasing rate was slowed down as the J_p increased. The evidence can be clearly seen in the J_p of 20 mA/cm^2 and J_p of 60 mA/cm^2 cases. The Cu concentration decreased from 36.9 at% to 18.4 at% when the t_{off} was increased from 30 to 100 ms in the case of J_p of 20 mA/cm^2. A much longer t_{off} was required, from 290 to 590 ms, for the Cu concentration to decrease from 37.1 at% to 18.9 at% in the case of J_p of 60 mA/cm^2. The alloys electrodeposited at higher J_p contain higher Cu concentration. Although the dissolution rate is highly dependent on the Cu concentration, but diffusion of Cu^{2+} away from surface

of the substrate and Au^+ from the bulk to the reaction site could also affect the dissolution rate. Hence, a longer t_{off} is needed to reach the same Cu concentration when the J_p is high.

Effects of the t_{off} on the grain size showed similar trends at various J_p, which the grain size initially decreased to a minimum value of ca. 4.40 nm and then the grain size increased when the t_{off} increased, as shown in Fig. 4.4(b). The displacement reaction occurred during the off-time period can initiate re-arrangement of atoms in the alloy, which could induce nucleation or grain growth of the reduced metals in the alloy. Driving force of the re-arrangement is dependent on the dissolution rate. When the driving force is high, the re-arrangement is more vigorous and nucleation is induced. As shown in Fig. 4.4(a) and 4.4(b), the grain size reduced with a decrease in the Cu concentration until the Cu concentration reached ca. 36.0 at%. On the other hand, the re-arrangement is less vigorous and grain growth is favored when the Cu concentration is low. This is why grain coarsening was observed when the Cu concentration was lower than ca. 36.0 at% as the t_{off} increased.

As a result, a wide Cu concentration ranging from 10.1 at% to 50.0 at% was attained by adjusting either or both the J_p and the t_{off}. In addition, the critical point observed at the Cu concentration of ca. 36.0 at% indicated the grain size was interrelated to the alloy composition. Fig. 4.5 shows the grain size as a function of the Cu concentration. The Cu concentration and the grain size followed a monotonic relationship. Similar behavior was reported in other PC electrodeposited alloys [29–31]. When compared to the DC electrodeposited Au–Cu, the DC electrodeposited Au–Cu also showed the same monotonic relationship. Furthermore, as shown in Fig. 4.5, the PC electrodeposition allows fabrication of Au–Cu alloys with a wider range of the Cu concentration and a much finer grain size than those of the DC electrodeposition, which

are both advantageous for applications as movable micro-components.

4.3.3. Morphology of Au–Cu Alloys

Effects of the PC electrodeposition parameters on morphology of the Au–Cu films were observed by the SEM as shown in Fig. 4.6. Overview of the Au–Cu alloys electrodeposited at the J_p of 15 mA/cm^2 showed bright surfaces when the t_{off} was between 20 to 50 ms. From Fig. 4.6(a), the alloy film electrodeposited at the t_{off} of 20 ms showed pebble-like structures, and size of the pebble-like structures shrank gradually as the t_{off} increased to 50 ms as shown in Fig. 4.6(b) and (c). The surface became dull when the t_{off} increased to 100 ms, and the pebble-like structures were still observed as shown in Fig. 4.6(d). When a lower J_p at 5 mA/cm^2 was used, two alloy films deposited at the t_{off} of 30 and 100 ms both showed dull surface. Size of the pebble-like structures increased as the t_{off} increased to 100 ms (Fig. 4.6(f)). The surface condition became very rough when the J_p was increased to 20 mA/cm^2. As shown in Fig. 4.6(g), the alloy film deposited at the J_p of 20 mA/cm^2 and the t_{off} of 20 ms showed large agglomerates of colony-like clusters, and dull surface was observed. Then the surface became bright and size of the pebble-like structures decreased as the t_{off} increased to 50 ms, shown in Fig. 4.6(h). An interesting conclusion could be made here, which Au–Cu alloys with similar surface morphology and similar Cu concentration could be fabricated using different pulse parameters (Fig. 4.6(b): J_p = 15 mA/cm^2, t_{off} = 30 ms; Fig. 4.6(h): J_p = 20 mA/cm^2, t_{off} = 50 ms). This result demonstrated that not only the grain size but also the surface morphology was both interrelated to the Cu concentration. The morphology, composition, grain size, and electrodeposition parameters of the Au–Cu alloys are summarized in Table 4.2.

Effects of the J_p and the t_{off} on the morphology and the Cu concentration are

summarized and illustrated in Fig. 4.7. In general, roughness of the surface is affected by the current density applied, and smoothness of the surface is related to the displacement reaction, i.e., dissolution of the Cu component in the Au–Cu alloy. In other words, an increase in the J_p leads to roughening of the surface, and promotion of the displacement reaction causes smoothening of the surface. For example, when a high J_p and a short t_{off} are applied, a rough surface would be formed during the on-time period because of the high J_p, and the smoothening effect caused by the displacement reaction would be insufficient because of the short t_{off}. In this case, a rough surface condition is obtained as shown in Fig. 4.6(g). When a high J_p and a long t_{off} are applied, although the high J_p would give a rough surface, but with a long enough t_{off}, the displacement reaction could cause enough smoothening effect to produce a smooth surface. On the other hand, when a low J_p is used, the surface would be less rough than the one using high J_p. However, the Cu concentration is low when a low J_p is used, and this limits the displacement reaction, that is the surface smoothening effect. As observed in the alloys electrodeposited at the J_p = 5 mA/cm^2 in Fig. 4.6(e) and 4.6(f), the surface condition did not become smoother as the t_{off} increased from 30 to 100 ms.

4.3.4. Micro-Mechanical Properties of Pulse Electroplated Au–Cu Alloys

Micro-mechanical properties of the PC electrodeposited Au–Cu alloys were evaluated by micro-compression tests to demonstrate the potential for applications in micro-electronic devices. The micro-pillars were fabricated from the thick Au–Cu films by FIB, and the Cu concentration of each pillar was 46.5 at%, 33.9 at%, 21.0 at%, and 12.2 at%, respectively. Fig. 4.8 shows SIM images of the Au–Cu alloy micro-pillars before and after the micro-compression tests. For the Cu concentration of 46.5 at% pillar

(Fig. 4.8(a) and (b)), the surfaces showed clear boundaries originating from the large agglomerates observed in Fig. 4.6(g). After the compression test, brittle fracture was observed as shown in Fig. 8(b), which is suggested to be induced by the cracks along the agglomerate boundaries. As the Cu concentration decreased to 33.9 at% (Fig. 4.8(c) and (d)), the typically polycrystalline deformation (barrel-shape [24,32]) was observed. The micro-pillars containing lower Cu concentration (Cu concentration = 21.0 at% in Fig. 4.8(e) and (f) and 12.2 at% in Fig. 4.8(g) and (h)) also exhibited the same barrel-shape deformation. The large agglomerates and the brittle fracture were also observed in the DC Au–Cu alloys electrodeposited using a high current density, which the brittle fracture was observed when the Cu concentration was higher than 38 at%.

Engineering strain-stress (*SS*) curves obtained from the micro-compression tests are shown in Fig. 4.9. The σ_y were estimated from the 0.2% offset line of the elastic deformation region [33]. The Cu concentration of 46.5 at% and 33.9 at% micro-pillars showed almost the same σ_y of 1.36 and 1.38 GPa, respectively. However, the subsequent flow stress behaviors were different between the two pillars, which is attributed to the difference in the deformation behaviors shown in Fig. 4.8(b) and (d). The brittle fracture in the Cu concentration of 46.5 at% micro-pillar lead to the stagnant and trembling flow stress. In contrast, the flow stress continuously increased after the yielding region for the Cu concentration of 33.9 at% micro-pillar, which is a result of the barrel-shape deformation. The micro-pillars with lower Cu concentration (21.0 at% and 12.2 at%) showed similar *SS* curves as the Cu concentration of 33.9 at% micro-pillar but lower σ_y of 1.06 GPa and 0.90 GPa, respectively.

After all, the σ_y ranged from 0.90 to 1.38 GPa in the PC electrodeposited Au–Cu micro-pillars are all higher than that of pure Au, which can be understood as synergistic

effects of the grain boundary strengthening [5] and the solid solution strengthening mechanisms [9,10]. Based on the grain boundary strengthening mechanism, the strength of metallic materials is proportional to reciprocal square root of the grain size. This relationship is known as the Hall–Petch relationship [5]. On the other hand, the solid solution strengthening comes from the restriction of dislocation movement due to the interaction between dislocation and solute atoms [9,10]. A number of theories for solid solution strengthening have been proposed that the strength is proportional to the solute concentration with order of 1/2 [9] or 2/3 [10], which depends on the solute concentration. It is worth noticing that the highest σ_y at 1.38 GPa obtained in the PC electrodeposited Au–Cu micro-pillar is higher than that of DC electrodeposited micro-pillar with the same Cu concentration (σ_y = 1.15 GPa) [20], demonstrating the capability to further refine the grain size and enhance the strength by pulse current electrodeposition.

4.4. Conclusions

In this study, effects of the pulse current parameters on the alloy composition, grain size, surface morphology, and micro-mechanical property of the Au–Cu alloys were investigated. A wide copper concentration in the Au–Cu alloys ranging from 10.1 to 53.0 at% was obtained. An increase in the Cu concentration was observed by using either or both of a high pulsed current density and a short current off-time. The smallest grain size of ca. 4.40 nm was achieved in films having the Cu concentration ranged from 30.0 to 35.0 at%. Grain refinement was achieved with a high J_p, and promoting the displacement reaction could also reduce the grain size. A high J_p resulted roughening of the surface, and enhancing the displacement reaction lead to a surface smoothening effect. Deformation behavior of the Au–Cu micro-pillar was affected by the Cu concentration,

which brittle fraction was observed when the Cu concentration was higher than 38 at%. An ultrahigh σ_y at 1.38 GPa was obtained in the micro-pillar having the Cu concentration of 33.9 at% and the grain size of 4.68 nm, which is a result of synergistic effects of the grain boundary strengthening and solid solution strengthening mechanisms. In conclusion, the present study demonstrated the simplicity (by the pulse current electrodeposition) and the versatility in controlling properties of the Au–Cu alloys for applications in design and fabrication of micro-components in micro-electronic devices.

4.5. References

[1] D. Yamane, T. Konishi, T. Matsushima, K. Machida, H. Toshiyoshi, and K. Masu, Design of Sub-1g Microelectromechanical Systems Accelerometers, Appl. Phys. Lett. 104 (2014) 074102.

[2] Y. Okinaka and M. Hoshino, Some Recent Topics in Gold Plating for Electronics Applications, Gold Bull. 31 (1998) 3–13.

[3] J.R. Greer, W.C. Oliver, W.D. Nix, Size Dependence of Mechanical Properties of Gold at the Micron Scale in the Absence of Strain Gradients, Acta Materialia, 53 (2005) 1821–1830.

[4] H. Honma and K. Hagiwara, Fabrication of Gold Bumps Using Gold Sulfite Plating, J. Electrochem. Soc. 142 (1995) 81–87.

[5] N.J. Petch, The Cleavage Strength of Polycrystals, J. Iron Steel Inst. 174 (1953) 25–28.

[6] Y. Wang, M. Chen, F. Zhou, and E. Ma, High Tensile Ductility in a Nanostructured Metal, Nature 419 (2002) 912–915.

[7] C.-Y. Chen, M. Yoshiba, T. Nagoshi, T.-F.M. Chang, D. Yamane, K. Machida, K. Masu, and M. Sone, Pulse Electroplating of Ultra-Fine Grained Au Films with High Compressive Strength, Electrochem. Commun. 67 (2016) 51–54.

[8] H. Tang, C.-Y. Chen, T. Nagoshi, T.-F.M. Chang, D. Yamane, K. Machida, K. Masu, and M. Sone, Enhancement of Mechanical Strength in Au Films Electroplated with Supercritical Carbon Dioxide, Electrochem. Commun. 72 (2016) 126–130.

[9] R.L. Fleischer, Substitutional Solution Hardening, Acta Mater. 11 (1963) 203–209.

[10] R. Labusch, A Statistical Theory of Solid Solution Hardening, Phys. Status Solid. B 41 (1970) 659–669.

[11] L. Deléhouzée and A. Deruyttere, The Stacking Fault Density in Solid Solutions Based on Copper, Silver, Nickel, Aluminium and Lead, Acta Mater. 15 (1967) 727–734.

[12] K. Maki, Y. Ito, H. Matsunaga, and H. Mori, Solid-Solution Copper Alloys with High Strength and High Electrical Conductivity, Scripta Mater. 68 (2013) 777–780.

[13] N. Ibl, Some Theoretical Aspects of Pulse Electrolysis, Surf. Technol. 10 (1980) 81–104.

[14] D.-T. Chin, Mass Transfer and Current-Potential Relation in Pulse Electrolysis, J. Electrochem. Soc. 130 (1983) 1657–1667.

[15] M.S. Chandrasekar and M. Pushpavanam, Pulse and Pulse Reverse Plating—Conceptual, Advantages and Applications, Electrochim. Acta 53 (2008) 3313–3322.

[16] C. Müller, M. Sarret, and T. Andreu, Electrodeposition of ZnMn Alloys Using Pulse Plating, J. Electrochem. Soc. 150 (2003) C772–C776.

[17] A. Marlot, P. Kern, and D. Landolt, Pulse Plating of Ni–Mo Alloys from Ni-rich Electrolytes, Electrochem. Acta 48 (2002) 29–36.

[18] A.F. Jankowski, C.K. Saw, and J.P. Hayes, Nanocrystalline Growth and Grain-Size Effects in Au–Cu Electrodeposits, Thin Solid Films 515 (2006) 1152–1156.

[19] E. Brun, F. Durut, R. Botrel, M. Theobald, O. Legaie, I. Popa, and V. Vignal, Influence of the Electrochemical Parameters on the Properties of Electroplated Au-Cu Alloys, J. Electrochem. Soc. 158 (2011) D223–D227.

[20] H. Tang, C.-Y. Chen, M. Yoshiba, T. Nagoshi, T.F.M. Chang, D. Yamane, K. Machida, K. Masu, and M. Sone, High-Strength Electroplated Au–Cu Alloys as Micro-Components in MEMS Devices, J. Electrochem. Soc. 164 (2017) D244–D247.

[21] B. Jönsson and S. Hogmark, Hardness Measurements of Thin Films, Thin Solid

Films 114 (1984) 257–269.

[22] M.F. Doerner, D.S. Gardner, W.D. Nix, Plastic Properties of Thin Films on Substrates as Measured by Submicron Indentation Hardness and Substrate Curvature Techniques, J. Mater. Res. 1 (1986) 845–851.

[23] J.R. Greer and J.Th.M. De Hosson, Plasticity in Small-Sized Metallic Systems: Intrinsic Versus Extrinsic Size Effect, Prog. Mater. Sci. 56 (2011) 654–724.

[24] T. Nagoshi, A. Shibata, Y. Todaka, T. Sato, and M. Sone, Mechanical Behavior of a Microsized Pillar Fabricated from Ultrafine-Grained Ferrite Evaluated by a Microcompression Test, Acta Mater. 73 (2014) 12–18.

[25] A.J. Bard, R. Parsons, and J. Jordan, Standard Potentials in Aqueous Solution, CRC Press, New York, 1985.

[26] E. Budevski, G. Staikov, and W.J. Lorenz, Electrocrystallization: Nucleation and Growth Phenomena, Electrochim. Acta 45 (2000) 2559–2574.

[27] S. Roy and D. Landolt, Effect of Off-Time on the Composition of Pulse-Plated Cu-Ni Alloys, J. Electrochem. Soc. 142 (1995) 3021–3027.

[28] P.E. Bradley and D. Landolt, A Surface Coverage Model for Pulse-Plating of Binary Alloys Exhibiting a Displacement Reaction, Electrochim. Acta 42 (1997) 993–1003.

[29] S.K. Ghosh, A.K. Grover, G.K. Dey, and M.K. Totlani, Nanocrystalline Ni–Cu Alloy Plating by Pulse Electrolysis, Surf. Coat. Technol. 126 (2000) 48–63.

[30] F. Liu and R. Kirchheim, Nano-Scale Grain Growth Inhibited by Reducing Grain Boundary Energy Through Solute Segregation, J. Cryst. Growth 264 (2004) 385–391.

[31] A.J. Detor and C.A. Schuh, Tailoring and Patterning the Grain Size of Nanocrystalline Alloys, Acta Mater. 55 (2007) 371–379.

[32] J.Y. Zhang, J.C. Cui, G. Liu, and J. Sun, Deformation Crossover in Nanocrystalline Zr Micropillars: The Strongest External Size, Scripta Mater. 68 (2013) 639–642.

[33] W.F. Hosford, Mechanical Behavior of Materials, 2nd edition, Cambridge University Press, New York, 2010.

4.6. Tables

Table. 4.1. Parameters for pulse electrodeposition of Au–Cu alloy films.

Operating parameters	Range
Pulse current density (mA/cm^2)	5–60
Current on-time (ms)	10
Current off-time (ms)	5–600
Electrolyte temperature (°C)	50

Table. 4.2. A summary of pulse parameters, Cu concentration ([Cu]), grain size (d_g), and morphology of the Au–Cu alloys presented in Fig. 4.6.

J_p, mA/cm^2	t_{off}, ms	[Cu], at%	d_g, nm	Morphology
20	20	46.5	4.83	Colony-like clusters and dull surface
	50	33.9	4.68	Pebble structure and bright surface
15	20	37.0	4.71	Pebble structure and bright surface
	30	34.1	4.82	Pebble structure and bright surface
	50	29.5	4.94	Pebble structure and bright surface
	100	21.0	6.16	Pebble structure and dull surface
5	30	18.0	7.03	Pebble structure and dull surface
	100	12.2	9.09	Pebble structure and dull surface

4.7. Figures

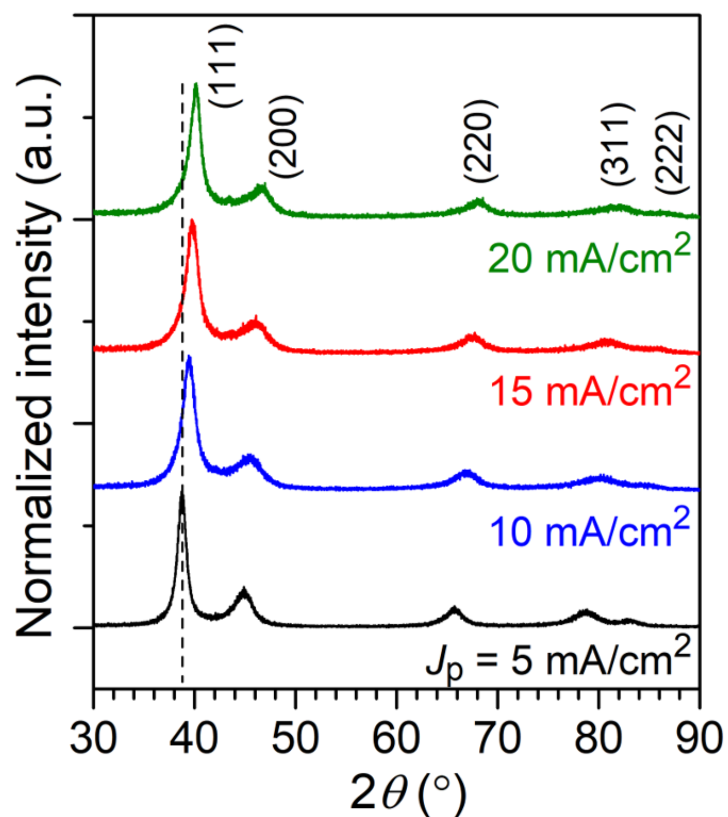

FIG. 4.1. XRD patterns of the Au–Cu alloys electrodeposited at the J_p varied from 5 to 20 mA/cm^2 with t_{on} and t_{off} both fixed at 10 ms. The straight dash line indicates the center of (111) diffraction peak in the J_p of 5 mA/cm^2 sample.

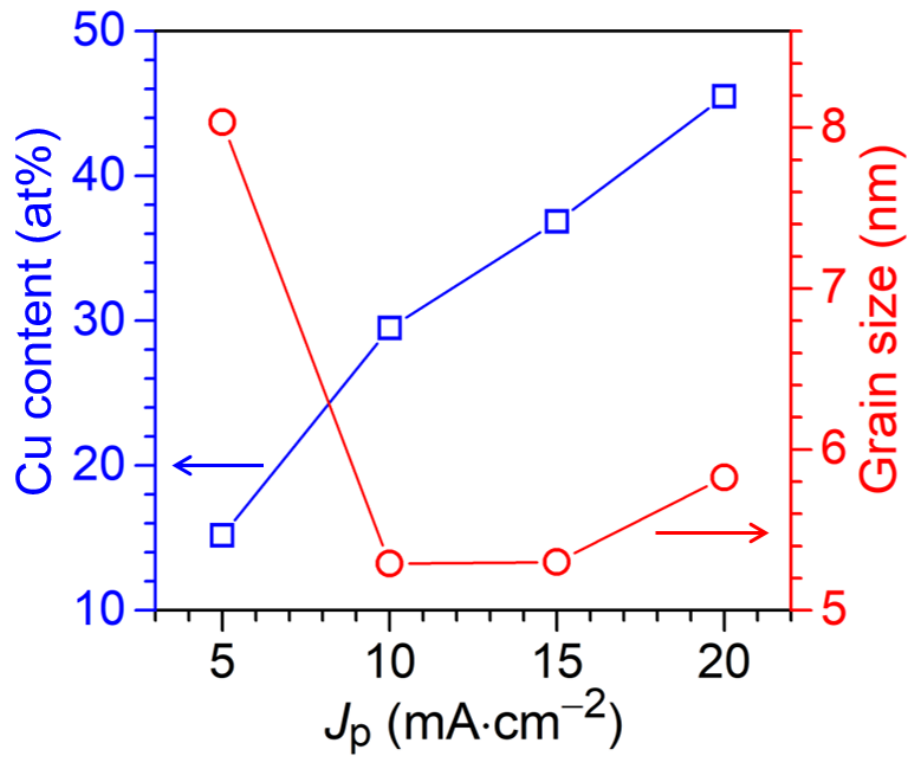

FIG. 4.2. Plots of the J_p versus the grain size and Cu composition. The t_{on} and t_{off} is fixed at 10 ms.

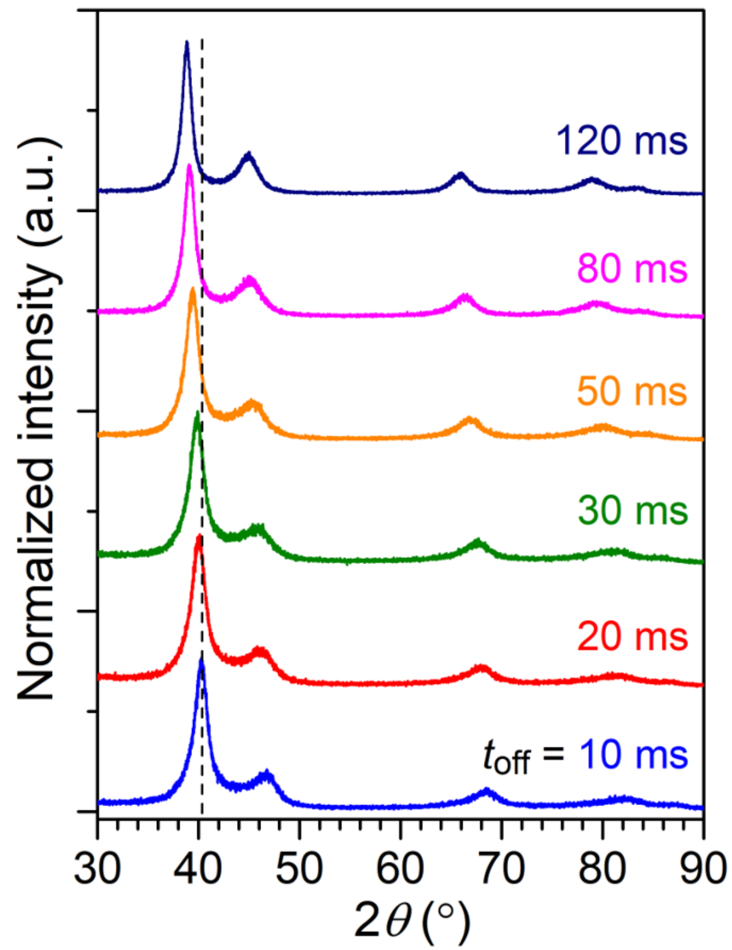

FIG. 4.3. XRD patterns of the Au–Cu alloys electrodeposited at the J_p of 20 mA/cm^2 with the t_{off} varied from 10 to 120 ms. The t_{on} was fixed at 10 ms. The straight dash line indicates center of the (111) diffraction peak in the t_{off} of 10 ms sample.

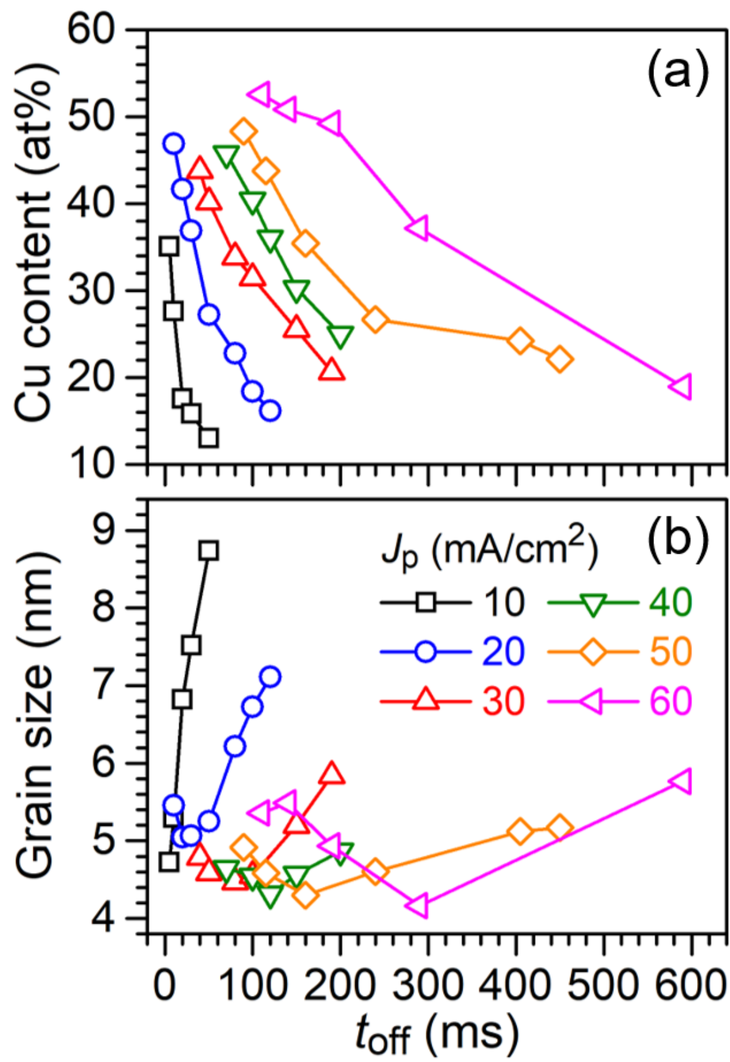

FIG. 4.4. Plots of the t_{off} versus the Cu concentration grain size and grain size. (a) Cu concentration versus t_{off} and (b) grain size versus t_{off}.

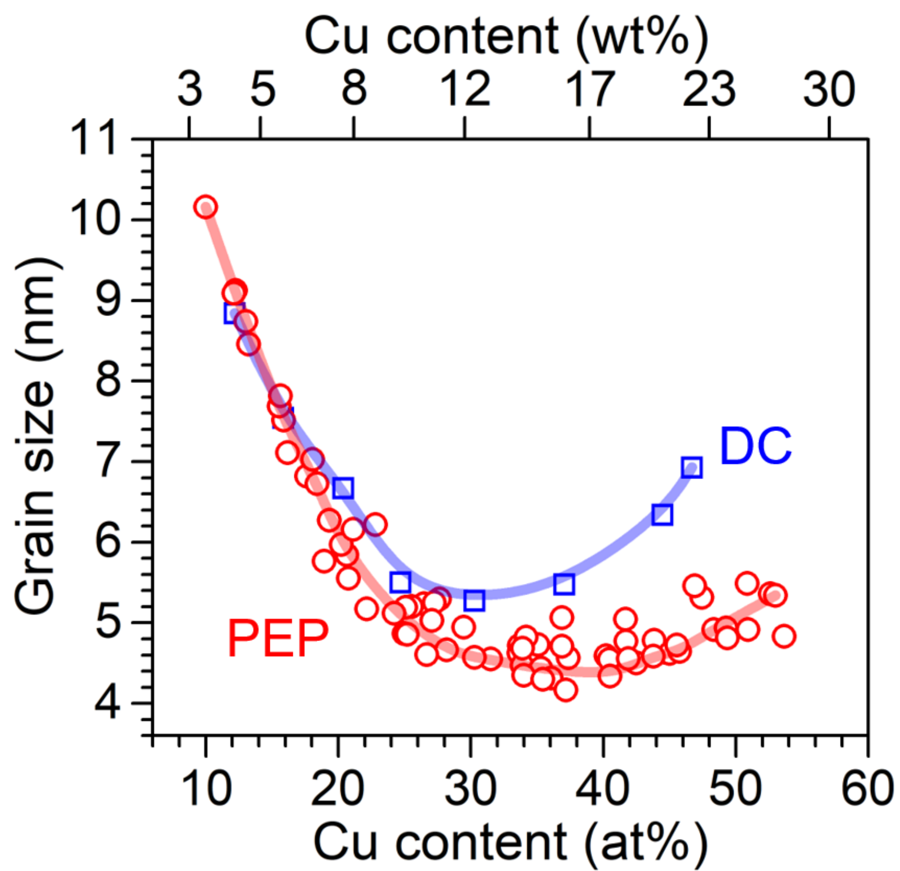

FIG. 4.5. A plot of relationship between grain size and composition for Au–Cu alloys electrodeposited with varied J_p and t_{off}.

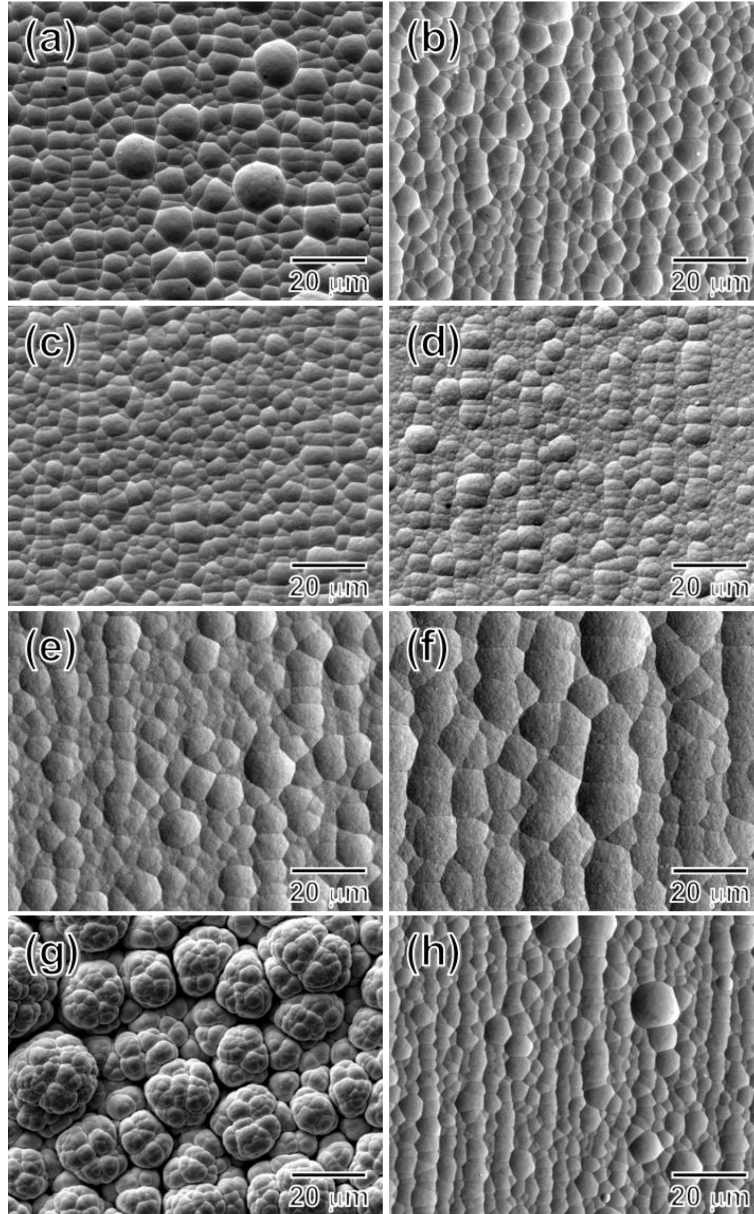

FIG. 4.6. SEM micrographs of the Au–Cu alloy thick films. The alloys electrodeposited at the J_p of 15 mA/cm^2 with the t_{off} of (a) 20 ms, (b) 30 ms, (c) 50 ms, and (d) 100 ms; J_p of 5 mA/cm^2 with (e) 30 ms and (f) 100 ms; J_p of 20 mA/cm^2 with (g) 20 ms and (h) 50 ms. The t_{on} is fixed at 10 ms.

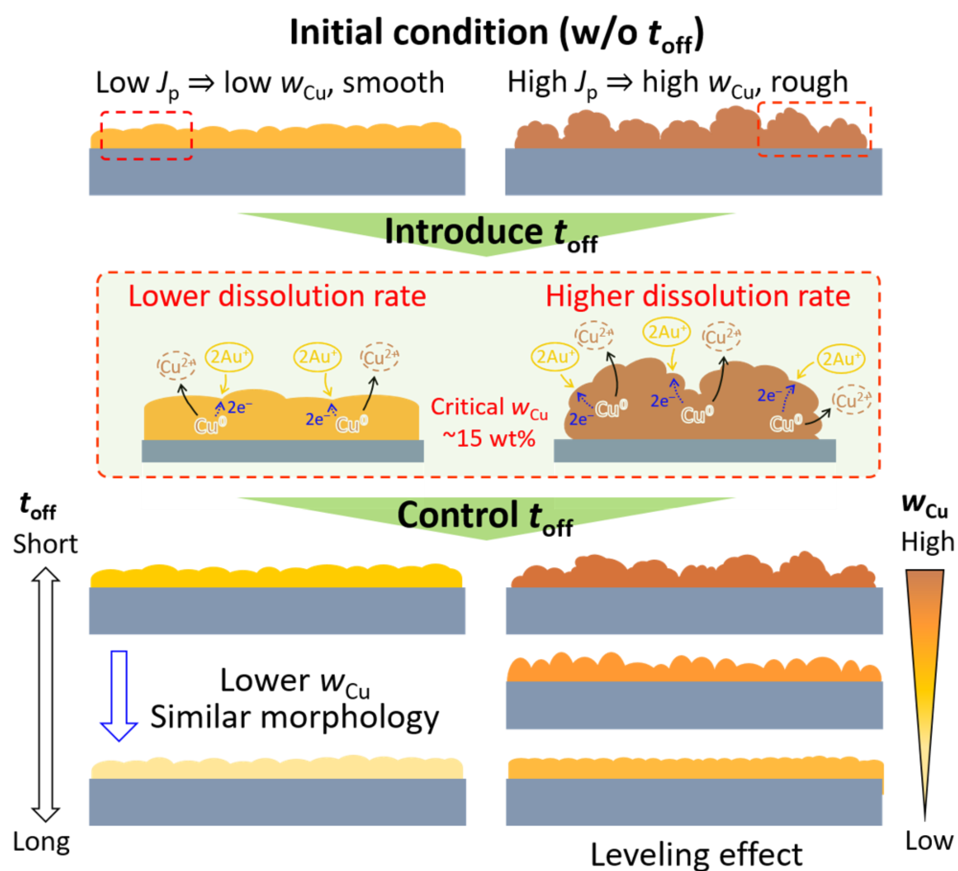

FIG. 4.7. Illustration of the morphology change with the pulse electrodeposition parameters.

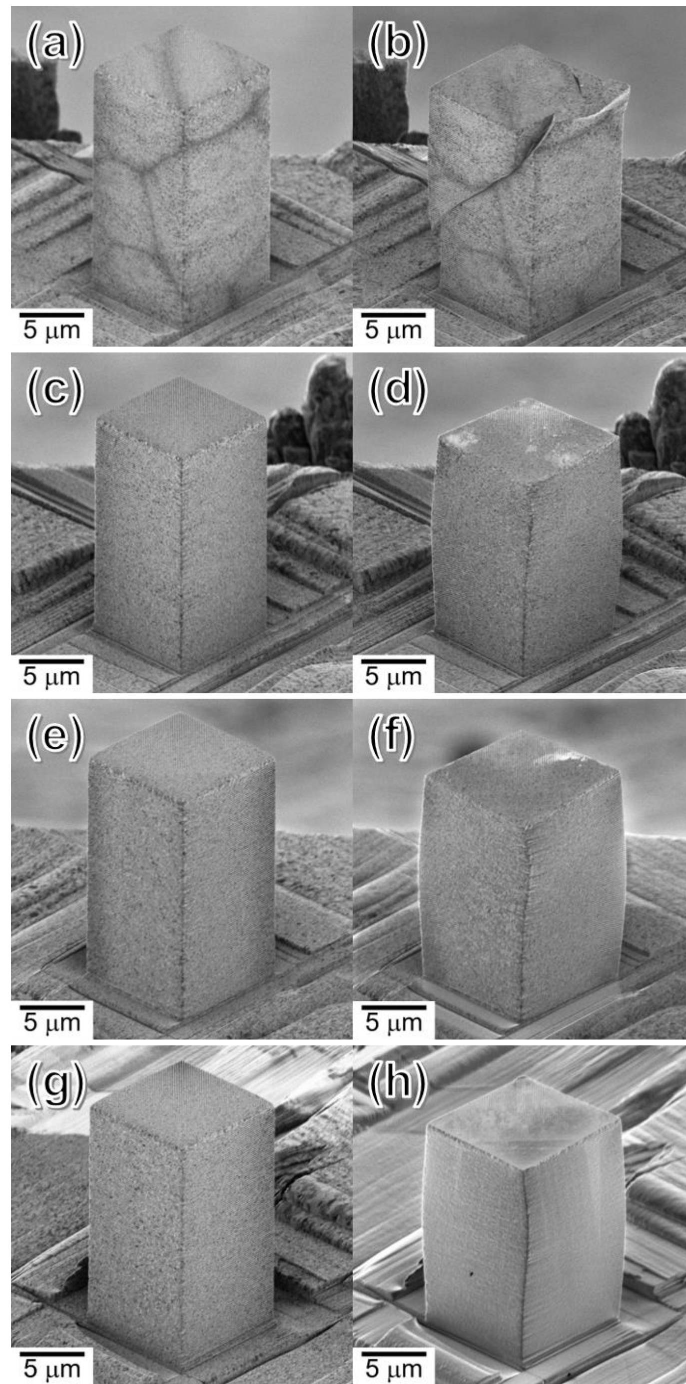

FIG. 4.8. SIM micrographs of the Au–Cu alloy micro-pillars (a–d) before and (e–f) after the micro-compression tests. The micro-pillars were fabricated from the thick films with the Cu concentration of (a, e) 46.5 at%, (b, f) 33.9 at%, (c, g) 21.0 at%, and (d, h) 12.2 at%.

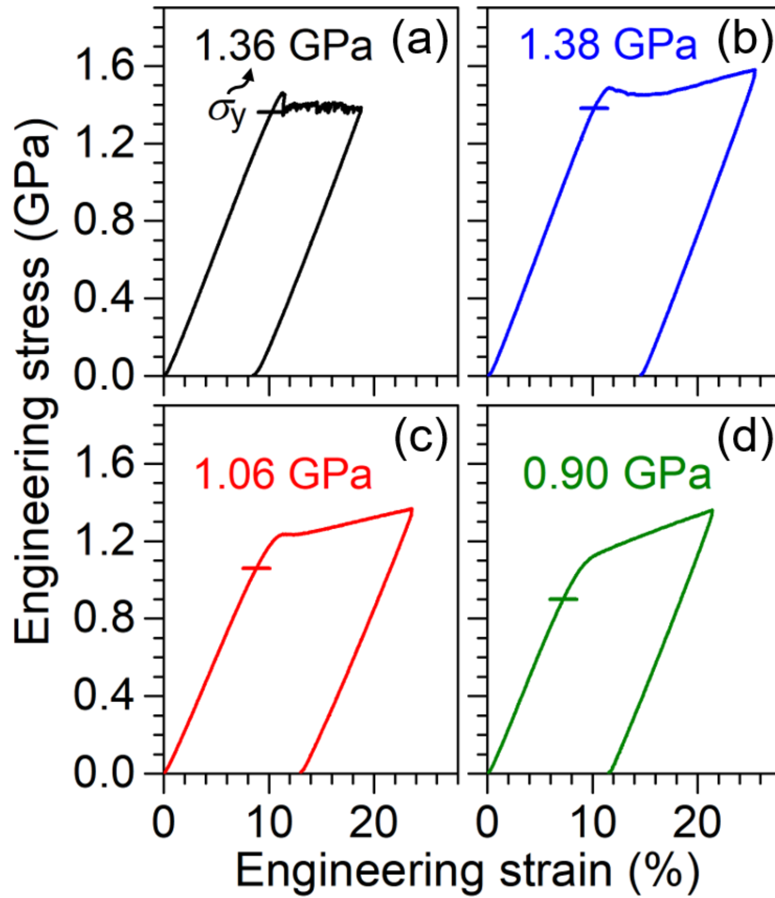

FIG. 4.9. Engineering *SS* curves of the micro-pillars containing the Cu concentration of (a) 46.5 at%, (b) 33.9 at%, (c) 21.0 at%, and (d) 12.2 at%. The yield strength (σ_y) is determined by the cross-point of the *SS* curve and the 0.2% offset line of the elastic deformation region. The σ_y is marked by a horizontal bar.

CHAPTER 5

Microstructure of Electrodeposited Au–Cu Alloys Observed by High-Resolution Transmission Electron Microscopy

5.1. Introduction

Microelectromechanical systems (MEMS) capacitive accelerometers have been developed in recent decades and widely used in the acceleration-detection applications including inertial navigation, earthquake prediction, and early diagnosis of neurological diseases [1]. Significant reduction of mechanical noise by uses of electrodeposited Au in movable micro-components in MEMS devices have been demonstrated [2,3], which further allows further enhancement in the sensitivity and miniaturization of the device. However, Au is known to be a soft metallic material and the yield strength in bulk state is reported to be 50–200 MPa [4]. A relatively high yield strength of ~500 MPa could be achieved by refining the grain size to nanoscale [5], but it still lower than the conventional silicon (Si) materials having the fracture strength of 1–3 GPa [6]. Besides, high purity nanocrystalline metals are known to have low thermal stability [7]. The undesired effect of grain growth would be induced by the necessary thermal treatment in the MEMS fabrication process, and the grain growth leads to lowering of the mechanical strength [8].

Further enhancement of mechanical strength can be achieved by alloying of the

nanocrystalline Au [9–11]. In previous chapters [12,13], I investigated micro-mechanical properties of the electrodeposited Au–Cu alloys using uniaxial micro-compression tests. The high yield strengths of 0.9–1.5 GPa could be regarded as synergistic effects of grain refinement and solid solution, and the flow stress during plastic deformation exhibited different behaviors when the alloy composition varied. The micro-pillar with lower copper concentration (below 15 at%) showed steady flow stress after the yielding; while, a stress drop was observed right after the yielding in early stage of the plastic deformation region and became more clearly as the copper concentration increased until ~34 at%. Such stress drop phenomenon was rarely found in nanocrystalline face-centered cubic (fcc) metals or alloys and should be clarified.

Another unexpected result is that, the yield strength continuously increased when the grain size was refined less than 10 nm. The finding is much different with the literature results evaluated by Vicker hardness tests, which clearly show inverse Hall-Petch behavior [9–11]. For nanocrystalline materials, it is generally recognized that the grain size estimated by X-ray diffraction (XRD) and Scherrer's equation is close to the grain size observed in transmission electron microscopy (TEM) [14,15]. While, the deviation between estimated and real grain size might occur if specific structure or texture exist. On the other hand, the nanotwinned structure is often observed in electrodeposited face-centered cubic (fcc) alloys (i.e., Ni–Mn, Ni–Co) [16,17]. In addition, reduction of the stacking fault energy (SFE) can promote the twin evolution in deposited fcc alloy films due to the lower energy requirement to form twin boundaries [18]. Moreover, formation of nanotwinned structure can also enhance the mechanical strength. Numerous studies have demonstrated that twin boundaries are effective on impeding dislocation motion similarly to the effect of grain boundaries [19–21]. Therefore, it is necessary to investigate

microstructure of the Au–Cu alloys through TEM observation and relate with the mechanical properties.

In this chapter, microstructures of the electrodeposited Au–Cu alloys were investigated using TEM measurements. In addition to the as-deposited alloys, the compressed micro-pillars were also investigated in order to understand the stress drop phenomenon observed in the early deformed state.

5.2. Experimental

Two Au–Cu alloys with different copper concentration of 15 at% and 32 at% were electrodeposited from a commercially available electrolyte mainly containing $X_3Au(SO_3)_2$ (X = Na, K) and $CuSO_4$, the details are given in Chapter 3 and 4. The chemical composition and crystal structure of plated Au–Cu alloys were characterized by energy-dispersive spectroscopy in a SEM (Hitachi SU4300SE) and X-ray diffraction (XRD, Rigaku Ultima IV). The Au–Cu alloys coated plates were subsequently thinned down to less than 100 μm by mechanical polishing and cut into semicircle disk shape by a mechanical punch machine. The micro-pillar specimens with the dimension of 15×15×30 μm^3 were fabricated from the semicircle specimens by focus ion beam (FIB, Hitachi FB2100). Micro-mechanical properties of the Au–Cu alloy micro-pillars were evaluated by micro-compression tests carried out at a constant displacement rate of 0.1 μm/s [15]. The compressed micro-pillars were further thinned down to thickness of ~100 nm by using a SEM-FIB (JEOL JIB-4500). The milling direction of Ga ion beam is parallel to the compression direction. The as-deposited Au–Cu alloys without compression were also prepared for the comparison. The microstructures were observed

using a scanning TEM (STEM, JEOL JEM-2100F) equipped with a high resolution TEM (HRTEM) operated at 200 kV.

5.3. Results and Discussion

At first, we observed the microstructure of as-electrodeposited Au–Cu alloys. Fig. 5.1(a) and (b) show the STEM images of the $Au_{85}Cu_{15}$ and $Au_{68}Cu_{32}$ alloys. Each nano-scaled and individual crystal grain could be distinguished by different contrasts and the clear boundaries. Average grain sizes of two alloys were 25.6 ± 4.1 nm and 16.6 ± 1.1 nm. Numerous single bands embedded in grain interior were observed in both two alloys. Such band structure was confirmed as nanotwin by HRTEM measurements. Fig. 5.1(c) shows a representative HRTEM image of a ~30 nm grain containing a ~8 nm width nanotwin. The grain is roughly divided into three equal parts by the parallel twin boundaries (TBs). The electron diffraction patterns converted by fast-fourrier transform (FFT) confirmed that the twin structure is symmetrical to the matrix with the TB (111) plane. On the other hand, grains containing half twin are also frequently observed. As shown in Fig. 5.1(d), the TB located in the middle of the grain separates the grain into two parts and the twin almost have the same size with the matrix.

Fig. 5.1(e) shows the XRD patterns of the as-electrodeposited $Au_{85}Cu_{15}$ and $Au_{68}Cu_{32}$ alloys. No other diffraction peaks originated from the ordered structure (i.e., $L1_2$ Au_3Cu or $L1_0$ AuCu) were observed except the fcc diffraction peaks. The average grain sizes estimated by the Scherrer equation and major (111) diffraction peak were 7.8 nm and 4.7 nm for $Au_{85}Cu_{15}$ and $Au_{68}Cu_{32}$ alloys, which is somewhat smaller than the values that observed from STEM. The twin in a grain could be recognized as an individual grain in the XRD; therefore, underestimation of grain size in XRD should be attributed

to presence of nanotwins as illustrated in Fig. 5.1(f).

For alloy electroplating, the applied current density or potential plays an important role on controlling the grain size and composition. In the case of Au–Cu alloys, the Cu concentration is increased by applying a higher cathodic current density due to different reduction potential between Au ion and Cu ion [9,11]. In the meanwhile, the higher current density can promote the nucleation rate resulting in finer grains in electrodeposits [22]. The twin evolution in the electrodeposited Au–Cu might be attributed to the reduction of stacking fault energy (SFE). A strong decrease in SFE as a result of alloying additions was experimentally examined and revealed to have a semi-log relationship in many fcc-based alloys [23,24], as expressed by:

$$\ln \gamma / \gamma_0 = k_\gamma (c / (1 + c))^2 \qquad (5\text{-}1)$$

$$c = x / x^* \qquad (5\text{-}2)$$

where γ_0 is the fault energy of the solvent metal, k_γ is a material constant, x is the alloying concentration, x^* is the solubility limit at high temperature. For example, the SFE of Cu reduces from ~70 mJ/m^2 to below than 10 mJ/m^2 when alloying with other elements [23]. Although the SFE of Au alloys were rarely reported in the literatures, it is reasonable to suppose that the SFE decreases by forming the Au–Cu alloys. Similar twin evolution was also reported in the electrodeposited Ni alloys [16,17].

Next, we evaluated micro-mechanical properties of the electrodeposited Au–Cu alloys using micro-compression tests. Fig. 5.2(a) and (b) shows SEM images of the $Au_{85}Cu_{15}$ and $Au_{68}Cu_{32}$ deformed micro-pillars with 12–14% compressive plastic strain. Similar barrel-shape deformations were observed in both micro-pillars, which are typical deformations for polycrystalline metallic materials. The engineering strain-stress curves obtained from the compression tests are shown in Fig. 5.2(c). The σ_y of $Au_{85}Cu_{15}$ and

$Au_{68}Cu_{32}$ micro-pillars are 0.95 GPa and 1.16 GPa, respectively. After the yielding point, the $Au_{85}Cu_{15}$ pillar exhibits steady flow stress during the plastic deformation until unloading. For the $Au_{68}Cu_{32}$ pillar, the flow stress declined at early plastic strain of ~1.7% to 2.5%. After that, it exhibits steadily increased trend as well as the $Au_{85}Cu_{15}$ pillar. It should be noticed that stress drop is rarely observed in the pure polycrystalline fcc micro-specimens [15,25].

Mechanical strengths of polycrystalline metals are typically affected by several strengthening mechanisms which take place simultaneously. In the present case of electrodeposited Au–Cu alloys, the obtained σ_y are considered to be influenced by multiple strengthening mechanisms:

$$\sigma_y = \sigma_{gb} + \sigma_{nt} + \sigma_{ss} \tag{5-3}$$

where σ_{gb} is the grain boundary strengthening, σ_{nt} is contribution from nanotwins, and σ_{SS} is the solid solution strengthening. The effect of grain size on the strength is known to be Hall–Petch relationship [26], and the term of σ_{gb} can be expressed as:

$$\sigma_{gb} = \sigma_0 + k_{HP} \cdot d_g^{-1/2} \tag{5-4}$$

where σ_0 is the friction resistance for dislocation movement within the polycrystalline grains, k_{HP} is the Hall–Petch coefficient, and d_g is the grain size. Moreover, the presence of nanotwin can also enhance the strength. The twin boundary has similar effect with grain boundary that forms barriers to the dislocation motion. Lu et al. [19,20,27] reported that the twin width and strength follow a Hall–Petch relationship-like behavior in the columnar-grained Cu with high density nanotwins perpendicular to the growth direction. However, such nanotwinned structure is somewhat different with the present Au–Cu alloys that only show one twin in a single grain. In this case, the twin could be regarded as an individual grain because it has similar size with matrix. This assumption could be

further suggested by the grain size difference in STEM and XRD, at which the STEM observed grain size ($d_{g,STEM}$) is roughly 3 times larger than the XRD estimated grain size ($d_{g,XRD}$). The presence of nanotwins would cause the deviation in the Hall–Petch plot. As shown in Fig. 5.3(a), the straight line plotted using the STEM observed grain size has sharper slope with the Hall–Petch coefficient of k_{HP} = 0.259 MPa(m)$^{0.5}$. The k_{HP} value decreases to 0.110 MPa(m)$^{0.5}$ when using the XRD estimated grain size. Then, the sum of σ_{gb} and σ_{nt} can be simplified as σ_{gb} if regarding the twin as grain. On the other hand, the Hall–Petch plot only considered the grain size without the effect of solid solution. For the solid solution strengthening σ_{ss}, the classical theories are established well in coarse-grain alloys such as Fleischer model [28] and Labusch theory [29]. Rupert et al. [30] further proposed an enhanced model modified from Fleischer model in nanocrystalline fcc alloys, in which the composition dependence is approximately linear to the solute concentration. This modified model for nanocrystalline alloys is in line with our experimental results as shown in Fig. 5.3(b).

To understand the stress drop phenomena observed in the strain-stress curves, the deformed microstructure in the compressed micro-pillars were further investigated by STEM and HRTEM measurements. Fig. 5.3(a) shows a STEM image of the $Au_{68}Cu_{32}$ alloy after compressed for 13.8% plastic strain, which is similar to the as-electrodeposited alloys in Fig. 5.1(a,b) that conspicuous nanotwins could be observed. In addition to the growth twin, deformation twins from highly deformed grains in HRTEM measurement were observed as shown in Fig. 5.3(b). The image shows that a deformation twin located near the original TB in the matrix crystal is obstructed in the interior grain. In addition, the opposite of matrix also shows small part of twin (right part of Fig. 3(b)). The magnified IFFT image shown in Fig. 5.3(c) reveals the extremely complex interaction

between the deformation twin and dislocation which force the twinning to stop in the matrix interior. Such interactions are considered to be one of the important behaviors during plastic deformation.

Deformation twinning is a possible mode for plastic deformation that is mainly observed in fcc nanocrystalline metals with low stacking fault energy (SFE), but also in fcc metals with medium-to-high SFE if deformed under extreme conditions. There are several twinning mechanisms [31–33] proposed and observed in nanocrystalline fcc metals, i.e. the random activation of partials (RAP) mechanism [33], the dislocation rebound mechanism [31], or the partial emissions from grain boundary [31,34]. However, if a single twin grows from a grain boundary but terminates inside a grain, it can only be formed by the partial emissions from grain boundary. Zhu et al. [35] observed the similar results in nanocrystalline Ni and proposed the relative mechanisms for Shockley twinning partials to multiply at GB. Furthermore, the SFE of the fcc metals is usually reduced by alloying, especially for the Au–Cu alloys. Therefore, the reduction of SFE can change the energy path (i.e. general planar fault energy [36]) and thus facilitates the deformation twinning under the applied stress. The stress drop observed in $Au_{68}Cu_{32}$ alloy pillar is reasonably considered to be the lowered energy requirement for Shockley twinning partials threading into grains to form deformation twins.

5.4. Conclusion

The microstructure of electrodeposited Au–Cu alloys with different compositions were observed by STEM and HRTEM. The observed grain sizes in $Au_{85}Cu_{15}$ and $Au_{68}Cu_{32}$ were 25.6 nm and 16.1 nm, respectively. Numerous growth twins were observed in the as-electrodeposited Au–Cu alloys, which might be the main reason

to cause the underestimation of grain size in XRD evaluation. The stress drop observed in $Au_{68}Cu_{32}$ pillar is attributed to the deformation twining confirmed by HRTEM measurement. Reduction of stacking fault energy is considered to promote initiation of deformation twinning.

5.5. References

[1] R.E. Mayagoitia, A.V. Nene, and P.H. Veltink, Accelerometer and Rate Gyroscope Measurement of Kinematics: An Inexpensive Alternative to Optical Motion Analysis Systems, J. Biomech. 35 (2002) 537–542.

[2] D. Yamane, T. Konishi, T. Matsushima, K. Machida, H. Toshiyoshi, and K. Masu, Design of Sub-1g Microelectromechanical Systems Accelerometers, Appl. Phys. Lett. (2014) 074102.

[3] M. Takayasu, S. Dosho, H. Ito, D. Yamane, T. Konishi, K. Machida, N. Ishihara, and K. Masu, A 0.18-μm CMOS Time-Domain Capacitive-Sensor Interface for Sub-1mG MEMS Accelerometers, IEICE Electron. Exp. 15 (2018) 1–12.

[4] H.D. Espinosa, B.C. Prorok, and B. Peng, Plasticity Size Effects in Free-Standing Submicron Polycrystalline FCC Films Subjected to Pure Tension, J. Mech. Phys. Solids 52 (2004) 667–689.

[5] H. Tang, C.-Y. Chen, T. Nagoshi, T.-F.M. Chang, D. Yamane, K. Machida, K. Masu, and M. Sone, Enhancement of Mechanical Strength in Au Films Electroplated with Supercritical Carbon Dioxide, Electrochem. Commun. 72 (2016) 126–130.

[6] T. Tsuchiya, O. Tabata, J. Sakata, and Y. Taga, Specimen Size Effect on Tensile Strength of Surface-Micromachined Polycrystalline Silicon Thin Films, J. Microelectromech. Sys. 7 (1998) 106–113.

[7] M.A. Atwater, D. Roy, K.A. Darling, B.G. Butler, R.O. Scattergood, and C.C. Koch, The Thermal Stability of Nanocrystalline Copper Cryogenically Milled with Tungsten, Mater. Sci. Eng. A 558 (2012) 226–233.

[8] J.A. Krogstad, C. Keimel, and K.J. Hemker, Emerging Materials for Microelectromechanical Systems at Elevated Temperatures, J. Mater. Res. 29 (2014)

1597–1608.

[9] A.F. Jankowski, C.K. Saw, and J.P. Hayes, Nanocrystalline Growth and Grain-Size Effects in Au–Cu Electrodeposits, Thin Solid Films 515 (2006) 1152–1156.

[10] J. Lohmiller, N.C. Woo, and R. Spolenak, Microstructure–Property Relationship in Highly Ductile Au–Cu Thin Films for Flexible Electronics, Mater. Sci. Eng. A 527 (2010) 7731–7740.

[11] E. Brun, F. Durut, R. Botrel, M. Theobald, O. Legaie, I. Popa, and V. Vignal, Influence of the Electrochemical Parameters on the Properties of Electroplated Au-Cu Alloys, J. Electrochem. Soc. 158 (2011) D223–D227.

[12] H. Tang, C.-Y. Chen, M. Yoshiba, T. Nagoshi, T.F.M. Chang, D. Yamane, K. Machida, K. Masu, and M. Sone, High-Strength Electroplated Au–Cu Alloys as Micro-Components in MEMS Devices, J. Electrochem. Soc. 164 (2017) D244–D247.

[13] H. Tang, C.-Y. Chen, T.-F.M. Chang, T. Nagoshi, D. Yamane, T. Konishi, K. Machida, K. Masu, and M. Sone, Au–Cu Alloys Prepared by Pulse Electrodeposition toward Applications as Movable Micro-Components in Electronic Devices, J. Electrochem. Soc. 165 (2018) D58–D63.

[14] T.-F.M. Chang, M. Sone, A. Shibata, C. Ishiyama, and Y Higo, Bright Nickel Film Deposited by Supercritical Carbon Dioxide Emulsion Using Additive-Free Watts Bath, Electrochim. Acta 55 (2010) 6469–6475.

[15] T. Nagoshi, T.-F.M. Chang, S. Tatsuo, and M. Sone, Mechanical Properties of Nickel Fabricated by Electroplating with Supercritical CO_2 Emulsion Evaluated by Micro-Compression Test Using Non-Tapered Micro-Sized Pillar, Microelectron. Eng. 110 (2013) 270–273.

[16] B.Y.C. Wu, P.J. Ferreira, and C.A. Schuh, Nanostructured Ni-Co Alloys with

Tailorable Grain Size and Twin Density, Metall. Mater. Trans. A 36A (2005) 1927–1936.

[17] G. Lucadamo, D.L. Medlin, N.Y.C. Yang, J.J. Kelly, and A.A. Talin, Characterization of Twinning in Electrodeposited Ni–Mn Alloys, Philos. Mag. 85 (2005) 2549–2560.

[18] D.A. Porter, K.E. Easterling, and M. Sherif, Phase Transformations in Metals and Alloys, 3rd version, CRC Press (2009).

[19] L. Lu, Y. Shen, X. Chen, L. Qian, and K. Lu, Ultrahigh Strength and High Electrical Conductivity in Copper, Science 304 (2004) 422–426.

[20] L. Lu, X. Chen, X. Huang, and K. Lu, Revealing the Maximum Strength in Nanotwinned Copper, Science 323 (2009) 607–610.

[21] G.-D. Sim, J. A. Krogstad, K.M. Reddy, K.Y. Xie, G.M. Valentino, T.P. Weihs, and K.J. Hemker, Nanotwinned Metal MEMS Films with Unprecedented Strength and Stability, Sci. Adv. 3 (2017) e1700685.

[22] H. Natter, T. Krajewski, and R. Hempelmann, Nanocrystalline Palladium by Pulsed Electrodeposition, Ber. Bunsenges. Phys. Chem. 100 (1996) 55–64.

[23] P.C.J. Gallagher, The Influence Effects on the of Alloying, Temperature, and Related Stacking Fault Energy, Metall. Trans. 1 (1970) 2429–2461.

[24] S.I. Hong and C. Laird, Mechanisms of Slip Mode Modification in F.C.C. Solid Solutions, Acta Mater. 38 (1990) 1581–1594.

[25] H. Kinashi, T. Nagoshi, T.-F.M. Chang, T. Sato, and M. Sone, Mechanical Properties of Cu Electroplated in Supercritical CO_2 Emulsion Evaluated by micro-compression test, Microelectron. Eng. 121 (2014) 83–86.

[26] N.J. Petch, The Cleavage Strength of Polycrystals, J. Iron Steel Inst. 174 (1953) 25–28.

[27] Y.F. Shen, L. Lu, Q.H. Lu, Z.H. Jin, and K. Lu, Tensile Properties of Copper with Nano-Scale Twins, Scripta Mater. 52 (2005) 989–994.

[28] R.L. Fleischer, Substitutional Solution Hardening, Acta Mater. 11 (1963) 203–209.

[29] R. Labusch, A Statistical Theory of Solid Solution Hardening, Phys. Status Solid. B 41 (1970) 659–669.

[30] T.J. Rupert, J.C. Trenkle, and C.A. Schuh, Enhanced Solid Solution Effects on the Strength of Nanocrystalline Alloys, Acta Mater. 59 (2011) 1619–1631.

[31] Y.T. Zhu, J. Narayan, J.P. Hirth, S. Mahajan, X.L. Wu, and X.Z. Liao, Formation of Single and Multiple Deformation Twins in Nanocrystalline Fcc Metals, Acta Mater. 57 (2009) 3763–3770.

[32] Y.T. Zhu, X.L. Wu, X.Z. Liao, J. Narayan, L.J. Kecskés, and S.N. Mathaudhu, Dislocation–Twin Interactions in Nanocrystalline Fcc Metals, Acta Mater. 59 (2011) 812–821.

[33] X.L. Wu, X.Z. Liao, S.G. Srinivasan, F. Zhou, E.J. Lavernia, R.Z. Valiev, and Y.T. Zhu, New Deformation Twinning Mechanism Generates Zero Macroscopic Strain in Nanocrystalline Metals, Phys. Rev. Lett. 100 (2008) 095701.

[34] V. Yamakov, D. Wolf, S.R. Phillpot, A.K. Mukherjee, and H. Gleiter, Dislocation Processes in the Deformation of Nanocrystalline Aluminium by Molecular-Dynamics Simulation, Nat. Mater. 1 (2002) 45.

[35] Y.T. Zhu, X.L. Wu, X.Z. Liao, J. Narayan, S.N. Mathaudhu, and L. J. Kecskés, Twinning Partial Multiplication at Grain Boundary in Nanocrystalline Fcc Metals, Appl. Phys. Lett. 95 (2009) 031909.

[36] S. Kibey, J.B. Liu, D.D. Johnson, and H. Sehitoglu, Predicting Twinning Stress in Fcc metals: Linking Twin-Energy Pathways to Twin Nucleation, Acta Mater. 55

(2007) 6843–6851.

5.6. Figures

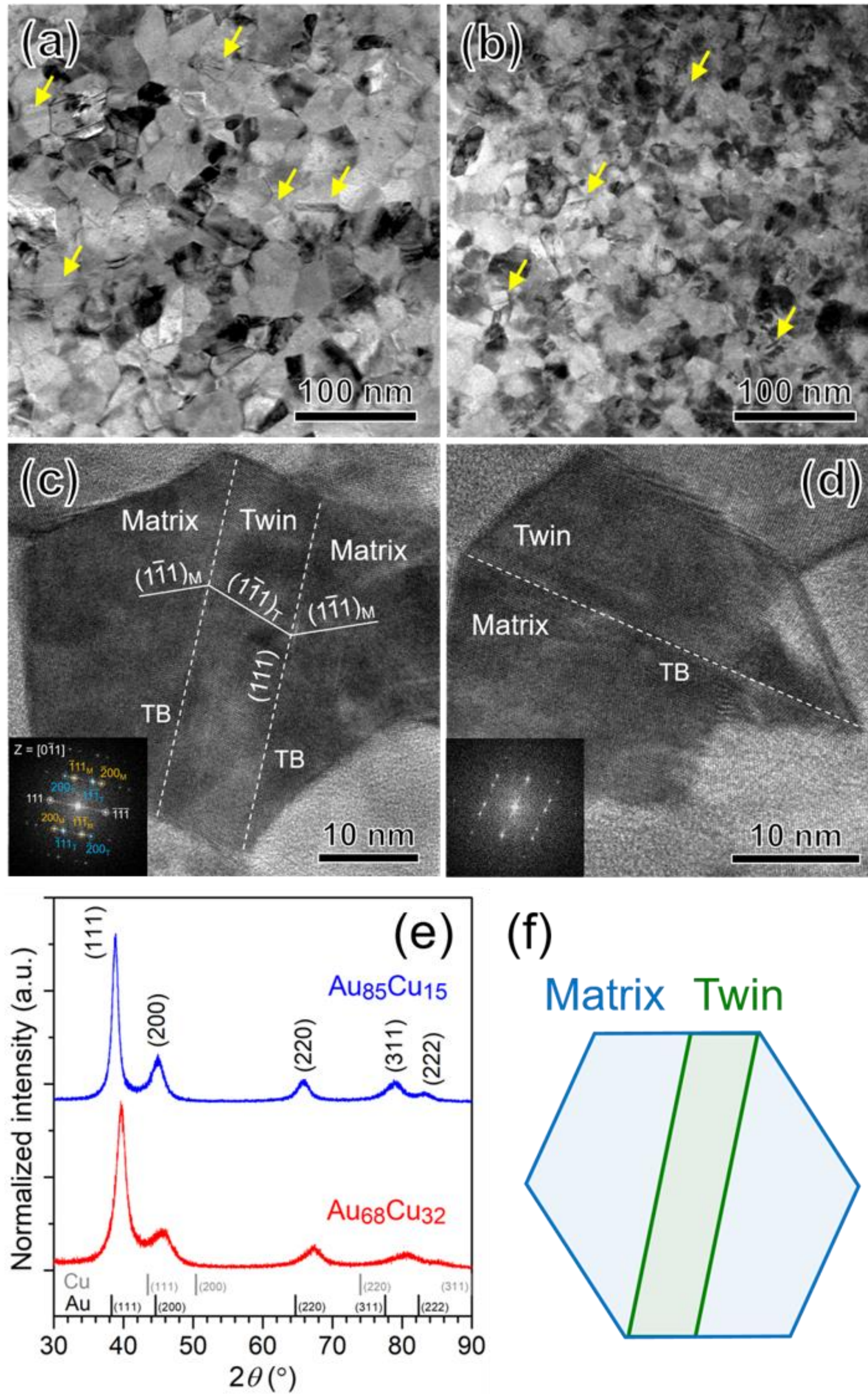

FIG. 5.1. (a,b) Bright-field STEM images of as-electrodeposited $Au_{85}Cu_{15}$ and $Au_{68}Cu_{32}$ alloys. The arrows indicating the nanotwins embedded in the grains. (c,d) Two representative HRTEM images taken from $Au_{85}Cu_{15}$ alloy. Zone axis: [0-11] (e) GI-XRD patterns of $Au_{85}Cu_{15}$ and $Au_{68}Cu_{32}$ alloys. The vertical bars in bottom indicating the diffraction peaks of pure Au and Cu. (f) Illustration of how the nanotwin embedded in a nano-scale grain causing the underestimation of grain size from XRD patterns.

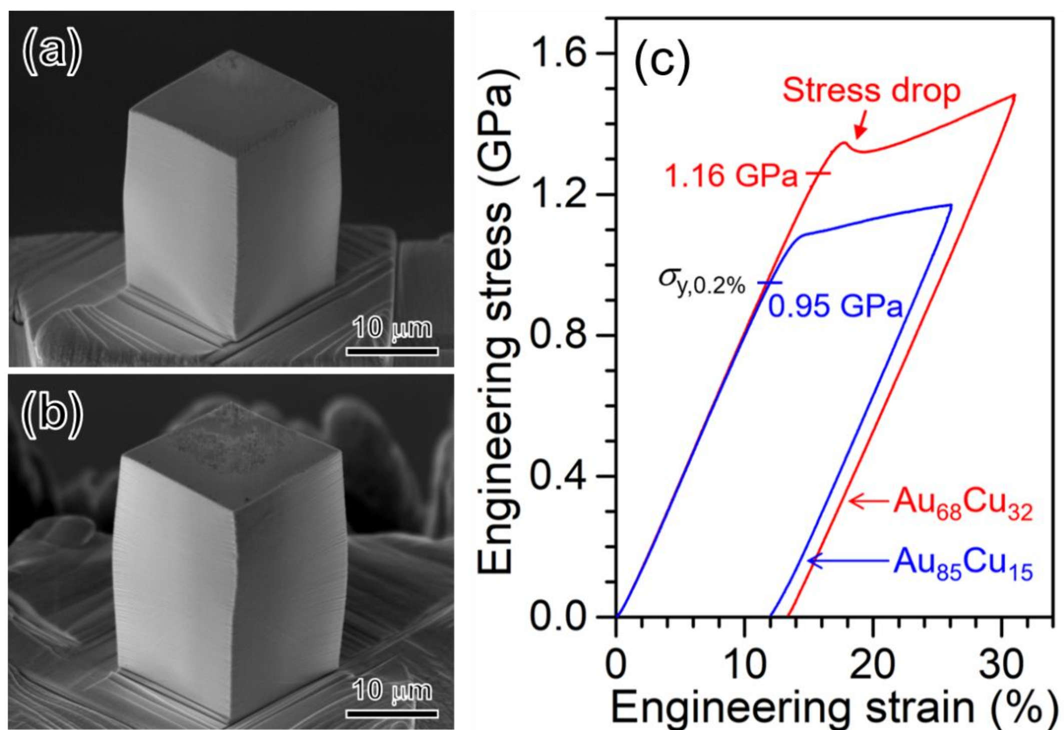

FIG. 5.2. SEM images showing the (a) $Au_{85}Cu_{15}$ and (b) $Au_{68}Cu_{32}$ micro-pillars after compression. (c) Engineering strain-stress curves obtained from micro-compression tests.

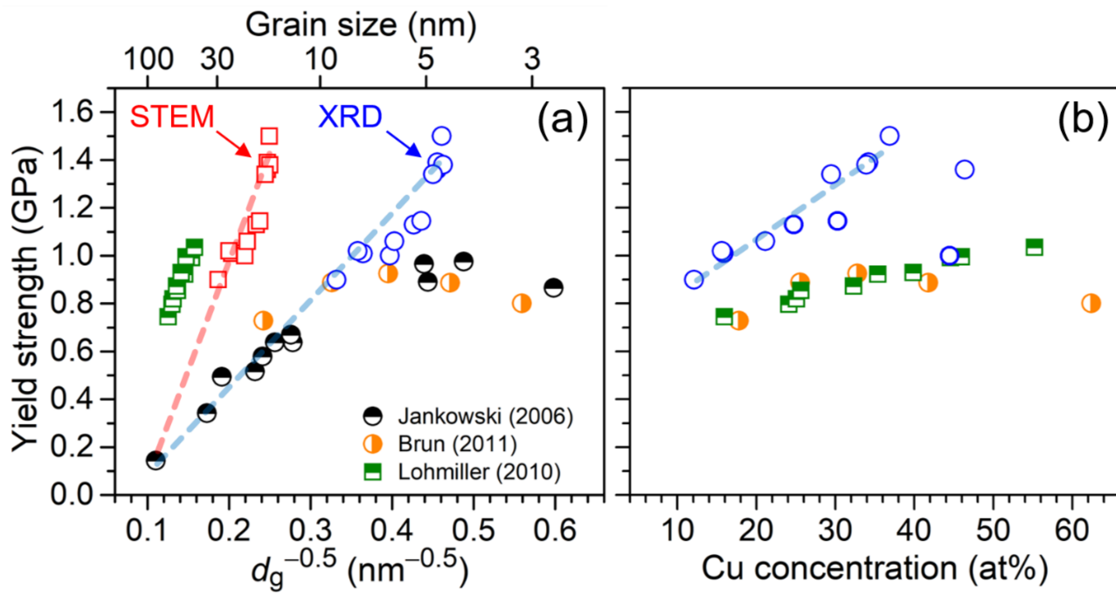

FIG. 5.3. (a) Hall-Petch plot for Au-Cu alloys. Hollow circle and squares indicate the grain size obtained from STEM and XRD, respectively. The yield strengths in the literatures were converted from Vickers hardness. (b) A plot of yield strength versus composition.

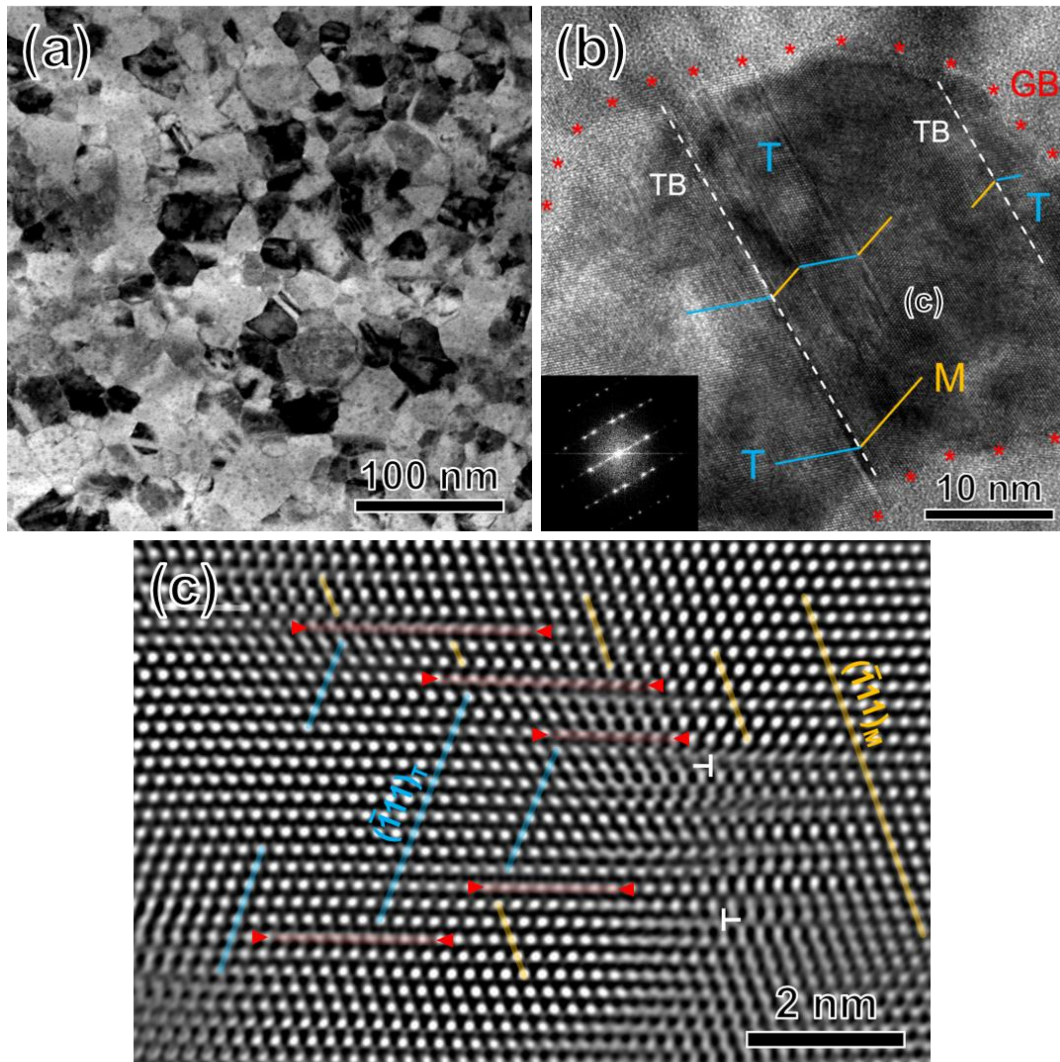

FIG. 5.4. (a) STEM image of $Au_{85}Cu_{15}$ alloy after ~13.8% compressive strain. (b) HRTEM image of a highly-deformed grain showing deformation twin. (c) Magnified IFFT image showing the deformation twin.

CHAPTER 6

Summary and General Conclusions

In the present study, high strength Au and Au–Cu alloys with nanocrystalline structure were successfully fabricated by electroplating techniques in order to replace the movable micro-components in microelectromechanical system (MEMS) devices. The enhanced mechanical strengths in Au electrodeposits exhibit high potential for ensuring the structural stability in the MEMS devices. Utilizing the pulse electroplating (PEP) and the electroplating with supercritical CO_2-contained electrolyte (EP-SCE) methods allows the pure Au to have the yield strength (σ_y) over than 520 MPa. The compressive flow stress (σ_f) of exceeding 800 MPa is the highest value reported for electrodeposited pure Au when compared with the literatures. Furthermore, the sample size effect was investigated for the EP-SCE Au. Different size of micro-specimens in micron-scale show the consistent σ_y, indicating that the nanocrystalline structure is preferred for the design of various micro-components.

The mechanical strength in Au materials was further enhanced by forming the Au–Cu solid solution alloys. With the control of electroplating conditions, a wide Cu concentration ([Cu]) in the Au–Cu alloys ranging from 10.1 to 50.0 at% was obtained. An ultrahigh σ_y at 1.38 GPa was obtained in the micro-pillar having the [Cu] of 33.9 at% and the grain size of 4.68 nm, which is a result of synergistic effects of the grain boundary strengthening and solid solution strengthening mechanisms. The displacement reaction

occurred only during the current-off period in PEP showed great influences on the composition and the grain size. The Au–Cu alloys with the [Cu] exceeding ~34 at% also exhibit high yield strength > 1.15 GPa; while, the fracture deformation formed after σ_y is unsuitable for structural design in MEMS devices. The microstructure of Au–Cu electrodeposits were further revealed by high-resolution transmission electron microscope (HRTEM). The nanotwinned structure was found in the electrodeposited Au–Cu alloys, including the half-twin and the single-lamellar twin in the crystal grains. Moreover, deformation twins were observed in the higher Cu content alloys, which causes different behaviors in the compressive flow stress region. As a result, the Au and Au–Cu alloys developed in the present study fulfill the requirement to replace the Si-based materials in next generation MEMS devices. The results of the present study are summarized as follows:

Chapter 2 An enhancement in the mechanical properties of the Au films fabricated by the PEP and the EP-SCE was confirmed by micro-compression tests. Grain refinement effect was observed in the Au films prepared by the PEP and the EP-SCE. Also, a high carbon content was observed in the EP-SCE film, which was one of the causes of the grain refinement effect. The σ_y and the σ_f of the EP-SCE micro-pillar with dimensions of $10 \times 10 \times 20$ μm^3 reached 520 MPa and ~800 MPa, respectively. The fine grains were suggested to be the main cause of the enhancement in the mechanical properties based on the grain-boundary hardening mechanism known as the Hall-Petch relationship. For the EP-SCE pillars with different pillar dimensions, the compressive flow stress increased from 740 to 810 MPa with a decrease in the pillar dimensions from $20 \times 20 \times 40$ to $10 \times 10 \times 20$ μm^3. The strengthening observation confirmed the sample size effect on

mechanical properties of micro-pillars composed of Au crystals having an average grain size in the nano-scale.

Chapter 3 Au–Cu alloys were fabricated by galvanostatic electroplating, and the micro-mechanical properties were evaluated by micro-compression tests. Surface morphology of the Au–Cu alloy films showed a wide variation from smooth surface to bump-clustered agglomerates as the current density varied from 2 to 9 mA/cm^2. A reduction in the grain size and an increase in the Cu content were observed with an increase in the current density. The film with the finest d_g at 5.3 nm was obtained when current density = 6 mA/cm^2 was used. For the micro-compression tests, the specimens used were micro-pillars with dimensions of 10×10×20 μm^3 fabricated from the electroplated Au–Cu alloys. The highest yield stress at 1.15 GPa was achieved for the Au–Cu alloy having d_g = 5.3 nm and the Cu content of 30.3 at%. The ultra-high yield stress was higher than the values reported in the literatures and suggested to be a synergistic effect of the grain boundary strengthening mechanism with the solid solution strengthening mechanism.

Chapter 4 Effects of the pulse current parameters on the alloy composition, grain size, surface morphology, and micro-mechanical property of the Au–Cu alloys were investigated. A wide copper concentration in the Au–Cu alloys ranging from 10.1 to 53.0 at% was obtained. An increase in the Cu concentration was observed by using either or both of a high pulsed current density and a short current off-time. The smallest grain size of ca. 4.40 nm was achieved in films having the Cu concentration ranged from 30.0 to 35.0 at%. Grain refinement was achieved with a high J_p, and promoting the displacement

reaction could also reduce the grain size. A high J_p resulted roughening of the surface, and enhancing the displacement reaction lead to a surface smoothening effect. Deformation behavior of the Au–Cu micro-pillar was affected by the Cu concentration, which brittle fraction was observed when the Cu concentration was higher than 38 at%. An ultrahigh σ_y at 1.38 GPa was obtained in the micro-pillar having the Cu concentration of 33.9 at% and the grain size of 4.68 nm, which is a result of synergistic effects of the grain boundary strengthening and solid solution strengthening mechanisms.

Chapter 5 The microstructure of electrodeposited Au–Cu alloys with different compositions were observed by STEM and HRTEM. The observed grain sizes in $Au_{85}Cu_{15}$ and $Au_{68}Cu_{32}$ were 25.6 nm and 16.1 nm, respectively. Numerous growth twins were observed in the as-electrodeposited Au–Cu alloys, which might be the main reason to cause the underestimation of grain size in XRD evalution. The stress drop observed in $Au_{68}Cu_{32}$ pillar is attributed to the deformation twining confirmed by HRTEM measurement. Reduction of stacking fault energy is considered to promote initiation of deformation twinning.

Acknowledgements

The present study was carried out under the supervision of Professor Masato Sone, Assistant Professor Tso-Fu Mark Chang of Tokyo Institute of Technology from October 2015 to September 2018.

First of all, I would like to express my deepest gratitude to Professor Masato Sone for his helpful guidance and invaluable comments throughout the work. He has given me a change to work in the research area of electrochemistry and metallurgy and many valuable advices during the entire period of my doctoral course.

I would like to express my gratitude to Assistant Professor Tso-Fu Mark Chang, Assistant Professor Masaki Tahara, Dr. Chun-Yi Chen, Dr. Takashi Nagoshi for their helpful advices and continuous supports in this study. I have learned a lot of things from them through their scientific advices.

I would also like to express my gratitude to Professor Hideki Hosoda, Professor Yoshisato Kimura, Associate Professor Takumi Sannomiya, Associate Professor Yoshihiro Terada for refereeing this thesis and for their valuable comments

I would like to grateful thanks to Professor Kazuya Masu, Professor Katsuyuki Machida, Associate Professor Toshifumi Konishi, Assistant Professor Daisuke Yamane, and other members of CREST, supported by JST for their discussion and support.

I wish to express my science gratitude to Associate Professor Yaw-Wang Chai for TEM observation and valuable comments.

I am much indebted to Ms. Kaori Toda, all members of Sone Laboratory and my alumnus including Mr. Bolun Zheng, Ms. Minami Teranishi, Mr. Yota Ishizuka, Mr. Sari Yanagida, Mr. Masaharu Yoshiba, Mr. Kemgo Igawa, Mr. Koichiro Tachibana, Mr. Takuma Suzuki for many helpful suggestions and kind assistance. I wish to appreciate

Ms. Wan-Ting Chiu, doctoral course student and Mr. Keisuke Asano, Mr. Ken Hashigata, Mr. Hideaki Nakajima, Mr. Takahiro Yamamoto, Kyotaro Nitta, master course students of Sone Laboratory, for general discussion and generous help.

Finally, I deeply appreciate my family with all my heart, who have given me this chance to study.

Publication Lists

Papers included in the thesis

1. "Sample size effect on micro-mechanical properties of gold electroplated with dense carbon dioxide"

   H. Tang, K. Hashigata, T.-F. M. Chang, C.-Y. Chen, T. Nagoshi, D. Yamane, T. Konishi, K, Machida, K. Masu, and M. Sone, Surf. Coat. Technol. 350 (2018) 1065–1070.

2. "Au–Cu Alloys Prepared by Pulse Electrodeposition toward Applications as Movable Micro-Components in Electronic Devices"

   H. Tang, C.-Y. Chen, T.-F. M. Chang, T. Nagoshi, D. Yamane, T. Konishi, K, Machida, K. Masu, and M. Sone, J. Electrochem. Soc. 165 (2018) D58–D63.

3. "High-Strength Electroplated Au–Cu Alloys as Micro-Components in MEMS Devices"

   H. Tang, C.-Y. Chen, M. Yoshiba, T. Nagoshi, T.-F. M. Chang, D. Yamane, K, Machida, K. Masu, and M. Sone, J. Electrochem. Soc. 164 (2017) D244–D247.

4. "Enhancement of mechanical strength in Au films electroplated with supercritical carbon dioxide"

   H. Tang, C.-Y. Chen, T. Nagoshi, T.-F. M. Chang, D. Yamane, K, Machida, K. Masu, and M. Sone, *Electrochem. Commun.* **72** (2016) 126–130.

Other papers

1. "Effects of Base Pressure on Growth and Optoelectronic Properties of Amorphous In-Ga-Zn-O: Ultralow Optimum Oxygen Supply and Bandgap Widening"

   K. Ide, K. Ishikawa, H. Tang, T. Katase, H. Hiramatsu, H. Kumomi, H. Hosono, and T. Kamiya, *Phys. Status Solid. A (2018) 1700832*.

2. "Multiple Roles of Hydrogen Treatments in Amorphous In–Ga–Zn–O Films", ECS J. Solid State Sci. Technol. 6 (2017) P365–P372.

   H. Tang, Y. Kishida, K. Ide, Y. Toda, H. Hiramatsu, S. Matsuishi, S. Ueda, N. Ohashi, H. Kumomi, H. Hosono, and T. Kamiya, *ECS J. Solid State Sci. Technol. 6 (2017) P365–P372*.

3. "Micro-Bending Testing of Electrodeposited Gold for Applications as Movable Components in MEMS Devices"

   K. Asano, H. Tang, C.-Y. Chen, T. Nagoshi, T.-F. M. Chang, D. Yamane, K. Machida, K. Masu, and M. Sone, *Microelectron. Eng. 180 (2017) 15–19*.

4. "Effects of thermal annealing on elimination of deep defects in amorphous In-Ga-Zn-O thin-film transistors"

   H. Tang, K. Ide, H. Hiramatsu, S. Ueda, N. Ohashi, H. Kumomi, H. Hosono, and T. Kamiya, *Thin Solid Films 614 (2016) 73–78*.

5. "Effects of residual hydrogen in sputtering atmosphere on structures and properties of amorphous In-Ga-Zn-O thin films"

H. Tang, K. Ishikawa, K. Ide, H. Hiramatsu, S. Ueda, N. Ohashi, H. Kumomi, H. Hosono, and T. Kamiya, *J. Appl. Phys. 118 (2015) 205703*.

6. "Fabrication and opto-electrical properties of amorphous (Zn,B)O thin film by pulsed laser deposition"

   H. Tang, J. Kim, H. Hiramatsu, H. Hosono, and T. Kamiya, *J. Ceram. Soc. Jpn. 123 (2015) 523–526*.

Presentation Lists

International

1. "Pulse Current Electrodeposition of Ultrahigh Strength Nanocrystalline Au–Cu Alloys"

   H. Tang, C.-Y. Chen, T.-F. M. Chang, D. Yamane, T. Konishi, K. Machida, K. Masu, and M. Sone, The 22nd Topical Meeting of the International Society of Electrochemistry, Tokyo, Japan, 2018.

2. "Ultrahigh strength in electroplated nanocrystalline Au–Cu alloys evaluated by micro-compression tests"

   H. Tang, C.-Y. Chen, T.-F. M. Chang, D. Yamane, T. Konishi, K. Machida, K. Masu, and M. Sone, 2017 MRS Fall Meeting & Exhibition, Boston, USA, 2017.

3. "Strategies of mechanical strengthening in electroplated Au materials for next-generation MEMS devices"

   H. Tang, C.-Y. Chen, T.-F. M. Chang, D. Yamane, T. Konishi, K. Machida, K. Masu, and M. Sone, IUMRS International Conference in Asia (IUMRS-ICA) 2017, Taipei, Taiwan, 2017.

4. "Utilization of supercritical carbon dioxide in the electrodeposition of Au films for MEMS application"

   H. Tang, C.-Y. Chen, T.-F. M. Chang, D. Yamane, K. Machida, K. Masu, and M. Sone, 21st International Conference on Solid State Ionics, Padua, Italy, 2017.

5. “Effect of supercritical carbon dioxide on micro-mechanical properties of electrodesposited gold”

   H. Tang, T.-F. M. Chang, C.-Y. Chen, and M. Sone, The 2nd International Conference and Expo on Separation Techniques, Valencia, Spain, 2016.

6. “Enhancement of mechanical properties in Au films electroplated with supercritical carbon dioxide for application in MEMS”

   H. Tang, C.-Y. Chen, T.-F. M. Chang, D. Yamane, K, Machida, K. Masu, and M. Sone, The 42nd International Conference on Micro- and Nano-Engineering (MNE 2016), Vienna, Austria, 2016.

7. “Preparation and characterization of gold films by electroplating with supercritical carbon dioxide”

   H. Tang, C.-Y. Chen, T.-F. M. Chang, K. Machida, D. Yamane, K. Masu, and M. Sone, The 19th Topical Meeting of the International Society of Electrochemistry, Auckland, New Zealand, 2016.

8. “Effects of thermal annealing on elimination of deep defects in amorphous In-Ga-Zn-O thin-film transistors”

   H. Tang, K. Ide, S. Ueda, H. Hiramatsu, N. Ohashi, H. Kumomi, H. Hosono, and T. Kamiya, The 9th International Symposium on Transparent Oxide and Related Materials for Electronics and Optics (TOEO-9), Tsukuba, Japan, 2015.

9. “Importance of excess oxygen on growth and carrier transport of amorphous In−Ga−Zn−O with impurity hydrogen”
H. Tang, K. Ishikawa, K. Ide, H. Hiramatsu, S. Ueda, N. Ohashi, H. Kumomi, H. Hosono, and T. Kamiya, The 15th International Meeting on Information Display (IMID 2015), Daegu, Korea, 2015.

10. “Hydrogen effects on subgap states in a-In−Ga−Zn−O investigated by HAXPES”
H. Tang, K. Ishikawa, K. Ide, H. Hiramatsu, S. Ueda, N. Ohashi, H. Kumomi, H. Hosono, and T. Kamiya, The 6th International Conference on Hard X-ray Photoelectron Spectroscopy, Hsinchu, Taiwan, 2015.

11. “Variation of subgap states in vacuum-deposited a-In−Ga−Zn−O, examined by hard X-ray photoemission spectroscopy”
H. Tang, K. Ishikawa, H. Hiramatsu, H. Kumomi, S. Ueda, N. Ohashi, H. Hosono, and T. Kamiya, The 24th Annual Meeting of MRS-J, Yokohama, Japan, 2014.

12. “Opto-electrical properties of polycrystalline and amorphous (Zn,B)O thin films fabricated by pulsed laser deposition”
H. Tang, H. Hiramatsu, H. Hosono, and T. Kamiya, The 8th International Conference on the Science and Technology for Advanced Ceramics (STAC-8), Yokohama, Japan, 2014.

Domestic

1. “電解めっき法による MEMS 用金銅合金の作製及び機械的特性評価”

   H. Tang, C.-Y. Chen, T.-F. M. Chang, D. Yamane, K. Machida, K. Masu, and M. Sone, The 65th JSAP Spring Meeting, Tokyo, Japan, 2018.

2. “High mechanical strength in gold films electroplated with supercritical carbon dioxide for MEMS applications”

   H. Tang, C.-Y. Chen, T.-F. M. Chang, D. Yamane, K, Machida, K. Masu, and M. Sone, The 77th JSAP Autumn Meeting, Niigata, Japan, 2016.

3. “Application of supercritical carbon dioxide in electroplating of gold materials used in MEMS devices”

   H. Tang, C.-Y. Chen, T.-F. M. Chang, D. Yamane, K, Machida, K. Masu, and M. Sone, The 63rd JSAP Spring Meeting, Tokyo, Japan, 2016.

4. “Annealing effects on subgap states in vacuum-deposited a-In−Ga−Zn−O examined by hard X-ray photoemission spectroscopy”

   H. Tang, K. Ishikawa, J. Herms, H. Hiramatsu, S. Ueda, N. Ohashi, H. Kumomi, H. Hosono, and T. Kamiya, The 11th Thin Film Materials and Devices Meeting (TFMD-11), Kyoto, Japan, 2014.